



저작자표시-비영리-변경금지 2.0 대한민국

이용자는 아래의 조건을 따르는 경우에 한하여 자유롭게

- 이 저작물을 복제, 배포, 전송, 전시, 공연 및 방송할 수 있습니다.

다음과 같은 조건을 따라야 합니다:



저작자표시. 귀하는 원저작자를 표시하여야 합니다.



비영리. 귀하는 이 저작물을 영리 목적으로 이용할 수 없습니다.



변경금지. 귀하는 이 저작물을 개작, 변형 또는 가공할 수 없습니다.

- 귀하는, 이 저작물의 재이용이나 배포의 경우, 이 저작물에 적용된 이용허락조건을 명확하게 나타내어야 합니다.
- 저작권자로부터 별도의 허가를 받으면 이러한 조건들은 적용되지 않습니다.

저작권법에 따른 이용자의 권리는 위의 내용에 의하여 영향을 받지 않습니다.

이것은 [이용허락규약\(Legal Code\)](#)을 이해하기 쉽게 요약한 것입니다.

[Disclaimer](#)

Ph.D. DISSERTATION

**Resistive Switching Characteristics of
Antimony Oxide Thin Film for Resistive Switching
Random Access Memory Application**

by

Youngbae Ahn

February 2013

**Department of Materials Science and Engineering
College of Engineering
Seoul National University**

Abstract

Resistive switching (RS) oxide materials, including various binary metal oxides (BMO) and perovskite structured ternary oxides, have been researched extensively for application to next-generation nonvolatile memory. Among the many candidate materials for resistive random access memory (ReRAM) applications, BMOs have emerged as promising materials due to their simple chemical composition and their compatibility with current complementary metal-oxide semiconductor technology. While earlier studies on the RS of BMO materials focused on materials with distinctive second phases, such as TiO_2 or NiO , due to the formation and rupture of evident CFs, recent studies have focused more on materials with less-evident phase transitions with higher binding energy, such as HfO_2 and Ta_2O_5 , because of their higher reliability. Nevertheless, it is still technically important to examine the RS of a material with far lower binding energy than those of typical transition metals oxides (TMO) for lower power consumption.

This dissertation discusses unipolar and bipolar resistive switching characteristics of antimony oxides (Sb_2O_5) films as new BMO material for RS application which has low binding energy, low energy band gap, and low melting point.

At first, antimony oxide thin films were deposited by reactive dc magnetron sputtering on Pt/Ti/SiO₂/Si substrates. Then, 100nm-thick Pt or Sb was formed by using e-beam evaporation and dc magnetron sputtering, respectively. The Pt/Sb₂O₅/Pt (PSP) and Sb/Sb₂O₅/Pt (SSP) structures were used for the measurement of electrical characteristics. Both PSP and SSP samples showed URS behavior with switching current lower than those of several other TMO materials by almost two orders of magnitude, but the switching endurance of the PSP sample was insufficient to satisfy the requirement for memory application. The weak binding between the pnictogen element Sb and O and the low melting point of Sb₂O₅ resulted switching of low energy consumption, but they also made the RS relatively less reliable. When Sb was used as the top electrode, endurance characteristics improved greatly because of the suppression of oxygen loss from the Sb₂O₅ films by the oxygen blocking effect of Sb TE. In addition, severe oxygen gas evolution from the Sb₂O₅ films during electroforming can be alleviated by pre-existing Sb clusters. TEM analysis confirmed that the electrical stressing induced the formation of metallic Sb clusters, which would percolate to form conducting filaments during the set switching. Therefore, it can be concluded that the URS phenomenon of Sb₂O₅ films is controlled by the formation and rupture of localized CF which is composed of metallic Sb.

The BRS phenomenon of Sb₂O₅ film was driven by the abnormal reset process during URS and the recovery of URS was induced by another

abnormal reset process during BRS. It can be understood that the migration of oxygen ions from and into the partly ruptured CF region near the anode is responsible for the BRS from the negative and positive bias polarities of the BRS set and reset steps. The Schottky emission and space-charge-limited current in HRS were the dominant conduction mechanisms for URS and BRS, respectively, meaning that the URS and BRS phenomena are induced by more complete (URS) and retarded (BRS) reoxidation and reduction of the local CF-ruptured region.

Finally, the effect of bottom electrode on resistive switching property of Sb_2O_5 thin film was studied using Ti and TiN as the bottom electrode. A reproducible and stable switching endurance were obtained in Sb/ Sb_2O_5 /TiN (SSN) structure. URS and BRS characteristics of of SSN structure were similar with that of SSP structure. Because TiN film is widely used material in electronic memory industry, SSN device can be one of promising candidate for use in ReRAM.

Keywords : Sb_2O_5 , Resistive switching, Pnictogen oxide, Antimony oxide, Unipolar switching, Bipolar switching, ReRAM

Student number : 2008-30180

Youngbae Ahn

Table of contents

Abstract	i
Table of contents	iv
List of Tables	vii
List of Figures	viii
1. Introduction	1
1.1 Overview	1
1.2 Objective and outline.....	4
1.3 Bibliography.....	7
2. Literature Review	8
2.1 Resistive switching random access memory (ReRAM); general introduction ..	8
2.1.1 Materials for ReRAM application	8
2.1.2 Classification of resistive switching phenomenon.....	10
2.2 Resistive switching mechanisms	13
2.2.1 Filament model	13
2.2.2 Interface model	18
2.3 Sb ₂ O ₅ as a resistance switching material	22
2.4. Electronic conduction mechanism in metal-insulator-metal structure.....	25
2.4.1 The thermionic (Schottky) current.....	25
2.4.2 The Poole-Frenkel current	28
2.4.3 Space-Charge-Limited current (SCLC)	31
3. Experimental procedure	38
3.1 DC sputtering system for thin films deposition	38
3.2 Analysis methods.....	43

3.3 Switching methods for electrical characterization.....	45
4. Results and Discussions	48
4.1 Unipolar resistive switching properties of Sb_2O_5 films	48
4.1.1 Introduction	48
4.1.2 Experimental procedure.....	56
4.1.3 Results and discussions	58
4.1.3-1 Crystal structure and chemical status of Sb_2O_5 films	58
4.1.3-2 Electrical characteristics of Sb_2O_5 films in PSP and SSP samples...	66
4.1.3-3 Resistive switching of Sb_2O_5 by localized filamentary mechanism .	79
4.1.4 Summary.....	87
4.2 Bipolar resistive switching characteristics in Sb_2O_5 films.....	89
4.2.1 Introduction	89
4.2.2 Experimental procedure.....	91
4.2.3 Results and discussions	93
4.2.3-1 Anode interfaced switching of Sb_2O_5 films.....	93
4.2.3-2 Bipolar resistive switching properties of Sb_2O_5 films	102
4.2.4 Summary.....	117
4.3 The effects of bottom electrode material on resistive switching properties of Sb_2O_5 films	118
4.3.1 Introduction	118
4.3.2 Experimental procedure.....	121
4.3.3 Results and discussions	123
4.3.3-1 Material properties of deposited TiN films	123
4.3.3-2 Resistive switching properties of $\text{Sb}/\text{Sb}_2\text{O}_5/\text{Ti}$ (SST) and $\text{Sb}/\text{Sb}_2\text{O}_5/\text{TiN}$ (SSN) structure.....	129
4.3.4 Summary.....	146
4.4 Bibliography	147

5. Conclusion.....	154
List of Publications.....	157
Abstract (Korean)	165

List of Tables

Table 2.1.1 Various binary metal oxide materials utilized for ReRAM devices

Table 3.1.1 Process conditions of the Sb_2O_3

Table 3.1.2 Process conditions of TiN films

Table 3.1.2 Process conditions of TiN films

Table 4.1.1 Physical properties of various BMO materials for ReRAM application

Table 4.1.2 Reset current values of unipolar resistive switching material

Table 4.2.1 Physical constant used in electro-thermal simulation

List of Figures

Figure 1.1.1 Technology performance evaluation of ReRAM reported in ITRS 2011.

Figure 2.1.1 I - V curves for (a) unipolar (nonpolar) switching in a Pt/NiO/Pt cell and (b) bipolar switching in a Ti/La₂CuO₄/La_{1.65}Sr_{0.35}CuO₄ cell.

Figure 2.2.1 Schematic diagram of unipolar resistive switching behavior.

Figure 2.2.2 C-AFM on TiO₂ films. (a) Schematic diagram of the C-AFM measurements. (b) I - V curves using the conducting AFM tip as a top electrode clearly show the forming, reset, and set operations. (c) Mapping of the current flow through the surface just after the forming operation with 8 V shows locally distributed conducting regions. (d) After the reset operation with 1 V, the TiO₂ surface in the HRS state shows that the locally distributed conducting regions disappear.

Figure 2.2.3 Ta 4d HX-PES spectra of TaO_x large-area test vehicle. The height of the reduced TaO_x component corresponds to the change of the resistance state, the low resistance state (LRS), the high resistance state (HRS), and the initial state showing the highest resistance state.

Figure 2.2.4 C - V curves under reverse bias for a Ti/PCMO/SRO cell show hysteretic behavior. This indicates that the depletion layer width (W_d) at the Ti/PCMO interface is altered by applying an electric field.

Figure 2.3.1 Unipolar and bipolar resistance switching curves in Sb₂O₅.

Figure 2.4.1 Energy diagram for a symmetrical MIM structure.

Figure 2.4.2 Schematic diagram of electronic potential energy in insulator containing a trap.

Figure 2.4.3 Variation of $\ln(J)$ as a function of V in the case of SCLC.

Figure 3.1.1 DC magnetron sputtering system of this study.

Figure 3.3.1 Typical I - V curves of URS in Pt/Sb₂O₅/Pt structure.

Figure 4.1.1 Temperature dependence of the Gibbs free energy of formation per one O₂ mole of various transition metal oxides.

Figure 4.1.2 (a) Glancing angle X-ray diffraction patterns of Sb₂O₅ films on Pt/Ti/SiO₂/Si substrate, (b) High resolution TEM image of Pt/Sb₂O₅/Pt structure.

Figure 4.1.3 (a) XPS Sb 3d (left panel) and Pt 4f (right panel) depth profiling spectra for Pt/Sb₂O₅/Pt structure. (b) shows the XPS Sb 3d (left panel) and Pt 4f (right panel) depth profiling spectra of Sb/Sb₂O₅/Pt structure.

Figure 4.1.4 AES depth profiles results of (a) Pt/Sb₂O₅/Pt and (b) Sb/Sb₂O₅/Pt structures

Figure 4.1.5 (a) The I - V results and (b) electrical endurance properties of Pt/Sb₂O₅/Pt structure.

Figure 4.1.6 (a) The URS I - V characteristics of the Sb/Sb₂O₅/Pt structure. Inset figure shows the leakage current of SSP and PSP structure during electroforming process. (b) The electrical endurance characteristics of SSP structure.

Figure 4.1.7 (a) The electroforming curves and (b) the URS I - V curves after electroforming process with $I_{cc} = -8$ mA, respectively, of Sb/Sb₂O₅/Pt structure using negative voltage sweep mode.

Figure 4.1.8 Schematic diagrams of oxygen ion and Sb cluster movement (a) at pristine state and (b) with high positive bias, and (c) with high negative bias.

Figure 4.1.9 (a) The magnitude of current and (b) the current density of Sb/Sb₂O₅/Pt structure with various device area. The current values were read at V= 0.5 V.

Fig 4.1.10 (a) The images of blown off region after electroforming process, (b) the schematic diagram of FIB patterns.

Figure 4.1.11 (a)~(c) The bright field TEM images of the Pt/Sb₂O₅/Pt structure after set process, (d)~(f) shows the inversed FFT images of fig. (a)~(c), respectively. (g)~(i) The FFT micrographs of the high resolution image of Sb₂O₅.

Figure 4.1.12 The schematic diagram of conducting filament formation process in Sb₂O₅ films.

Figure 4.2.1 The schematic diagram of *I-V* sweep method for anode-cathode interface switching experiment.

Figure 4.2.2 (a) *I-V* curves of the electroforming process (curve F), and subsequent reset process (curve R). *I-V* curves between pads A and C (curve A-C), and pads B and D (curve B-D) after the reset process is also shown in 4.1.2

Figure 4.2.3 (a) Simulation structure of SSP device, (b) temperature distribution in SSP device.

Figure 4.2.4 Schematic diagram of Sb/Sb₂O₅/Pt structure after the developed CFs.

Figure 4.2.5 The URS *I-V* characteristics of the Sb/Sb₂O₅/Pt structure.

Figure 4.2.6 *I-V* result of abnormal reset process during URS cycling measurement.

Figure 4.2.7 The BRS *I-V* characteristics after abnormal URS reset process.

Figure 4.2.8 The distribution of the low and high resistance values.

Figure 4.2.9 The *I-V* curves of the Sb/Sb₂O₅/Pt device measured at temperatures ranging from 25 to 105 °C. The Schottky plot of the J-T curves is shown in lower-left inset figure. The lower-right inset figure shows the variation in SBH as a function of V.

Figure 4.2.10 The I - V curves and fitting results using SCLC mechanism of the LRS and HRS plotted on a log-log scale. The upper-left inset shows 10 cycles of BRS.

Figure 4.2.11 The abnormal reset process during BRS cycling measurement.

Figure 4.2.12 The schematic diagrams of (a) reset state after abnormal reset process of URS, (b) set process of BRS, and (c) reset process of BRS.

Figure 4.3.1 The dependence of the deposition rate of TiN on the N_2 partial pressure with various temperature.

Figure 4.3.2 Glancing angle X-ray diffraction patterns of TiN films on SiO_2/Si substrate with various (a) temperature and (b) N_2 partial pressure.

Figure 4.3.3 AES depth profiles results of TiN/ SiO_2 structure.

Figure 4.3.4 Changes of resistivity values of TiN films as a function of N_2 partial pressure.

Figure 4.3.5 Electroforming curves of SSP, SST, and SSN devices.

Figure 4.3.6 Various electroforming curves of Sb/ Sb_2O_5 /Ti device.

Figure 4.3.7 The URS characteristics of SST structure.

Figure 4.3.8 The BRS characteristics of SST structure.

Figure 4.3.9 I - V curves and fitting results using SCLC mechanism of the HRS plotted on a log-log scale.

Figure 4.3.10 The schematic diagrams of (a) reset state from electroforming process, (b) set process of BRS, and (c) reset process of BRS.

Figure 4.3.11 The URS behaviors of Sb/ Sb_2O_5 /TiN structure.

Figure 4.3.12 URS endurance characteristics of Sb/ Sb_2O_5 /TiN structure.

Figure 4.3.13 I - V result of abnormal reset process of SSN structure during URS cycling measurement.

Figure 4.3.14 The BRS I - V characteristics after abnormal URS reset process. Inset figure shows distribution of the low and high resistance values.

Figure 4.3.15 Fitting results of SSN device using SCLC mechanism of the HRS plotted on a log-log scale.

1. Introduction

1.1 Overview

As the conventional charge-based memory device scaling limitation comes closer to near future, various new memory concepts have emerged as candidates for next-generation nonvolatile memory (NVM). In many of these memory devices, such as phase change random access memory (PRAM), magneto-resistive random access memory (MRAM), and resistive switching random access memory (ReRAM), the active elements for information storage are resistive. In PRAM, the information is stored as resistance contrast between crystalline (conducting) and amorphous (insulating) phases of phase-change materials such as $\text{Ge}_2\text{Sb}_2\text{Te}_5$ (GST). [1] MRAM is a memory which the stored data are represented by a magnetization direction and the read operation is performed by a resistance measurement and this implies that its operation relies on a magnetoresistance phenomenon. [2] ReRAM depends on the resistance-switching phenomenon by the formation of electrically conducting path, which is consist of metallic ion (or charged vacancy), induced by applied electric field (SET, low resistance state) and rupture of conducting filament by Joule heating (RESET, high resistance state). [3] Among the several candidates for next-generation NVMs, ReRAM has the

great potential to serve as a replacement for charge-based memory due to ReRAM device, which has simple structure as metal/oxide/metal, can be scaled to the ~10nm technology generation. Additional incentives for developing ReRAM technologies include their fast switching speed, low cost/bit, and high storage density through integration in crossbar arrays stacked in multiple levels in 3D. Figure 1.1.1 shows the technology performance evaluation for ReRAM in ITRS 2007, 2009, and 2011. [4]

However, ReRAM device is facing solution to some challenges. First and foremost, one needs a better understanding and control of the physical set/reset processes. In addition, ReRAM device needs better endurance and data retention time. Therefore, better performance of ReRAM is required for commercialization, and this is under intense and various investigations by numerous researchers around the world.

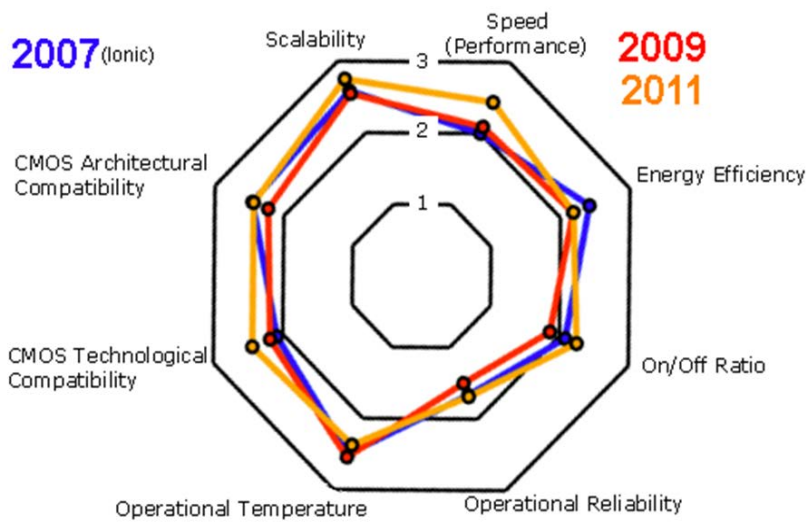


Figure 1.1.1 Technology performance evaluation of ReRAM reported in ITRS 2011.

1.2 Objective and outline

The resistive switching (RS) characteristics of binary metal oxides (BMOs) have been widely studied based on resistive switching mechanism and its device characteristics. The unipolar resistive switching (URS) property is characterized by various physical properties of BMOs such as binding energy, energy band gap, melting point, and presence of intermediate sub-oxide phase. The BMOs for URS switching suggested by many researchers can be roughly divided into two categories: one involving the transition metal oxides and one involving the non-transition metal oxides which have high binding energy, large the energy band gap, and high thermal stability. [6] The pnictogen oxides, such as Sb_2O_5 , are also binary metal oxides but there have not been studied intensively yet about its RS characteristics.

This dissertation discusses unipolar and bipolar resistive switching characteristics of antimony oxides (Sb_2O_5) films as new BMO material for RS application which has low binding energy, low energy band gap, and low melting point. Firstly, URS characteristics of Sb_2O_5 films were studied. The URS and electrical endurance characteristics of amorphous Sb_2O_5 films in Pt/ Sb_2O_5 /Pt and Sb/ Sb_2O_5 /Pt structures were investigated. Although both structures showed URS characteristics with power consumption smaller than those of other various transition metal oxides by \sim two orders of magnitude,

enhanced electrical endurance was obtained when Sb was employed as the top electrode than when Pt was employed as the top electrode. This improvement was explained by the creation of Sb clusters in the Sb_2O_5 films through the diffusion of oxygen from Sb_2O_5 to the Sb layer and the suppression of excessive oxygen loss during conducting filament formation process by the Sb top electrode. Secondly, bipolar resistive switching (BRS) characteristics of Sb_2O_5 were investigated. It was discovered that the BRS phenomenon was driven by the abnormal reset process during URS cycles which was induced by the rupture and recovery of the conducting filament (CF) in the localized region near the anode. The electrical conduction behavior in the high resistance state of URS and BRS was explained by the Schottky emission and space-charge-limited current mechanism, meaning that the URS and BRS phenomena are induced by the extent of reoxidation and reduction regarding the local CF-ruptured region. Finally, the effects of Ti (reactive metal with Sb_2O_5 films) and TiN (non-reactive metal with Sb_2O_5 films) bottom metal electrodes on the resistive switching properties of Sb_2O_5 thin films were presented.

The organization of this dissertation is as follows. Chapter 1 gives an overview of the subject of ReRAM and an outline of the dissertation. Chapter 2 reviews literature of general information on resistive random access memory, metal oxide films property for ReRAM application, and explained the resistive switching mechanisms. Chapter 3 explained the detailed deposition

processing, analysis method of deposited films, and electrical switching method. Chapter 4 presents the both unipolar and bipolar resistive switching characteristics of antimony oxide films. Chapter 5 provides the conclusion of the thesis.

1.3 Bibliography

- [1] Wong, H. P., Raoux, S., Kim, S., Liang, J., Reifenberg, J. P., Rajendran, B., Asheghi, M., and Goodson, K. E., Proceedings of the IEEE, 98(12), pp. 2201-2227. (2010)
- [2] Worledge, D. C., Gajek, M., Abraham, D. W., Brown, S., Gaidis, M. C., Hu, G., Nowak, J., O'Sullivan, E. J., Robertazzi, R. P., Sun, J. Z., Trouilloud, P. L., and Gallagher, W. J., Proc. Memory Workshop (IMW), 2012 4th IEEE International, pp. 1-3. (2012)
- [3] J. Joshua Yang, I. H. I., Thomas Mikolajick and Cheol Seong Hwang, MRS Bulletin, 37, pp. pp 131-137 (2012)
- [4] The International Technology Roadmap for Semiconductors (ITRS): Emerging research devices, 2011
- [5] D.S. Jeong, R. Thomas, R.S. Katiyar, J.F. Scott, H. Kohlstedt, A. Petraru, and C.S. Hwang, Reports on Progress in Physics 75 (7), 076502 (2012)
- [6] K.M. Kim, D.S. Jeong, and C.S. Hwang, Nanotechnology 22, 254002 (2011).

2. Literature Review

2.1 Resistive switching random access memory (ReRAM); general introduction

2.1.1 Materials for ReRAM application

Since the first demonstration of resistance switching phenomenon in chalcogenide glass material in 1960s [1], many resistance switching materials have been reported and the switching mechanisms have been discussed. The resistance switching have been observed not only in metal oxides but also in various types of materials, such as group IV and III-V semiconductors (in many cases, the switching is volatile) and organic compounds [2, 3]. Among various materials, binary metal oxide (BMO) has been received great attention from electronic semiconductor industry due to their simple composition and simple metal/insulator/metal (MIM) structures using conventional deposition technique such as sputtering, evaporation, and chemical vapor deposition (CVD). Table 2.1.1 lists the binary metal oxides that have shown reported resistance switching materials and its properties in the last eight years.

Table 2.1.1 Various binary metal oxide materials utilized for ReRAM devices

(U ; unipolar switching, B ; bipolar switching)

Material	Operation mode	Device size	Operation current	Ref.
Al ₂ O ₃	B	800 μm ²	20 ~ 50mA	[4]
NiO	U	30 × 30 μm ²	~ 20 mA	[5]
CoO	U	20 × 20 μm ²	~10 mA	[6]
Cu ₂ O	B	100 × 100 μm ²	~ 10 mA	[7]
FeO _x	B	–	< 5 mA	[8]
HfO ₂	B	10 ⁻⁵ cm ²	< 0.3 mA	[9]
MgO	U	200 × 400 nm ²	1 ~ 10 mA	[10]
Ta ₂ O _{5-x}	B	0.5 × 0.5 μm ²	< 200 μA	[11]
TiO ₂	U/B	700 μm ²	~ 1 mA(B), 30~ 50 mA (U)	[12]
ZnO	U	1500 μm ²	~ 20 mA	[13]
ZrO	U	1000 μm ²	~ 10 mA	[14]

2.1.2 Classification of resistive switching phenomenon

Resistance switching behavior is a key point in the ReRAM operation. Resistance memories nominally include all types of memories using two or more distinctive resistance states as the ‘0’ and ‘1’. The ReRAM device is characterized by two distinctive resistance states: a high resistance state (HRS) and a low resistance state (LRS). By applying either a voltage or a current to the cell, reversible switching between the HRS and LRS can be achieved. Once switched, the cell retains the particular resistance level for a long time. [15]

On the basis of I–V characteristics, the switching behaviors can be classified into two types: unipolar (nonpolar) and bipolar, for which typical I–V curves are shown in Figs. 2.1.1 (a) and (b), respectively. In unipolar resistive switching (URS), the switching procedure does not depend on the polarity of the write voltage signal. The pristine memory cell is in a highly resistive state and is put into a low-resistance state (LRS) by applying a specific high voltage stress. This process called ‘electroforming process’. After the electroforming process, the cell in a LRS is switched to a high-resistance state (HRS) by applied voltage (reset process). Switching from a HRS to a LRS (set process) is achieved by applied voltage that is usually larger than the reset voltage. During set process, the current is typically

limited by the current compliance of control circuit. The unipolar switching behavior has been widely observed in various BMOs. When the set to an LRS occurs at one bias polarity and the reset to HRS occurs at reversed bias polarity, this resistive switching behavior is called bipolar resistive switching (BRS). The BRS behavior occurs with many semiconducting oxides, such as complex perovskite oxides. [16]

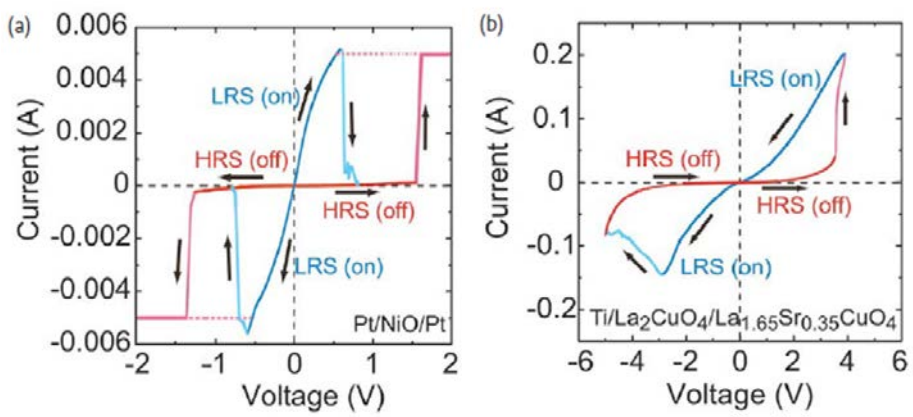


Figure 2.1.1 I - V curves for (a) unipolar (nonpolar) switching in a Pt/NiO/Pt cell and (b) bipolar switching in a Ti/La₂CuO₄/La_{1.65}Sr_{0.35}CuO₄ cell. [16]

2.2 Resistive switching mechanisms

Various studies have reported the origin and mechanisms for the resistance switching of ReRAM. There are usually two proposed models of resistive switching mechanism: the "filament model" and the "interface model". In this section, the filament model is firstly shown, then, interface model with the experimental evidence is described.

2.2.1 Filament model

A possible mechanism of resistance switching effect was reported in the study of NiO, which the switching was based on the formation and rupture of a nickel metallic filament in a NiO thin film held between two electrodes. [17] This is the first report to propose the mechanism called "filament model". In 1967, there was discussing the possibility of using this resistance switching phenomena for a memory application. [18, 19] Recently, Kwon et al. confirmed a formation and disruption of Ti_nO_{2n-1} (or so-called Magneli phase) metallic filament during resistive switching in Pt/TiO₂/Pt system. [20] Figure 2.2.1 shows a schematic diagram of filament-type resistive switching mechanisms that shows unipolar switching behavior. [16] In the forming

process (1), filamentary conducting path is generated as a soft breakdown in the dielectric material. Rupture of the filaments occurs during the reset (2) process, and filament formation during the set process (3). Thermally assisted redox and/or anodization near the interface between the electrode and the metal oxide films are widely considered to be the mechanism of the formation and rupture of the filaments. [21, 22]

The other studies using MIM structures supported the filamentary nature of the nonvolatile resistance switching. The electrode area dependence and the oxide thickness dependence on the I - V characteristics were investigated. [23] The results showed that the current flowed uniformly in the off-state, while in the on-state the current was localized. In addition, the set and reset voltages did not depend on the thickness of the oxide. These facts evidenced that the set and reset switching was associated with the homogeneous/inhomogeneous transition of the current distribution. Namely, the "electric faucet" turns on and off at the high-resistance interface to regulate the current flow in the filament conduction path between two electrodes.

Performing more physical observations, e.g., by conductive atomic force microscopy (C-AFM), the evidence of the formation and rupture of conducting channels was provided with a high spatial resolution. [24-26] By applying the external voltage to the C-AFM tip as the top electrode, the nonvolatile resistance switching operations of forming, reset, and set were triggered, the conducting spots appeared in the forming and set processes, and

the locally distributed conducting regions disappeared after the reset process, as shown in Fig. 2.2.2. Note that the diameter of the conducting spots was typically approximately 3-10 nm after the forming operation with a bias of 8.0 V. Reductions in the switching power and the switching speed for small memory element sizes were observed in the range of $10^2 \sim 10^{10}$ nm². [24] This is considered to be due to the reduction in the number of filaments and thinner filaments for a smaller electrode size. In the same report, a high resolution transmission electron microscopy (HR-TEM) image of the NiO layer showed the formation of nano-filament nickel channels across two electrodes through the grain boundaries of the insulating NiO matrix.

The contribution of the Joule heating to the filament rupture in Pt/NiO/Pt has been discussed in detail based on the self-accelerated thermal dissolution model for the reset process. [27] This model also proposes that the down-scaling of the cylindrically-shaped filament leads to the reduction of the reset current and the importance of the filament size control have been pointed out. Moreover, reliability predictions for the read disturb and data retention characteristics in NiO based ReRAM have been demonstrated by their analytical models. [28] It should be noted that the cross-sectional shape of the filament can affect the longitudinal position of the filament rupture. [29]

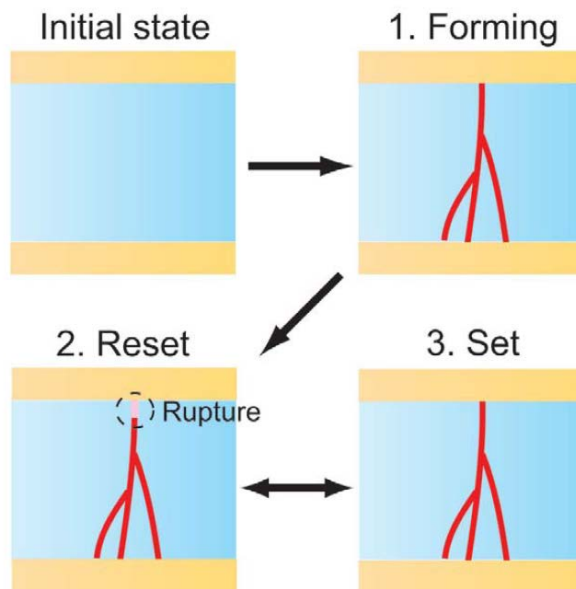


Figure 2.2.1 Schematic diagram of unipolar resistive switching behavior.

[16]

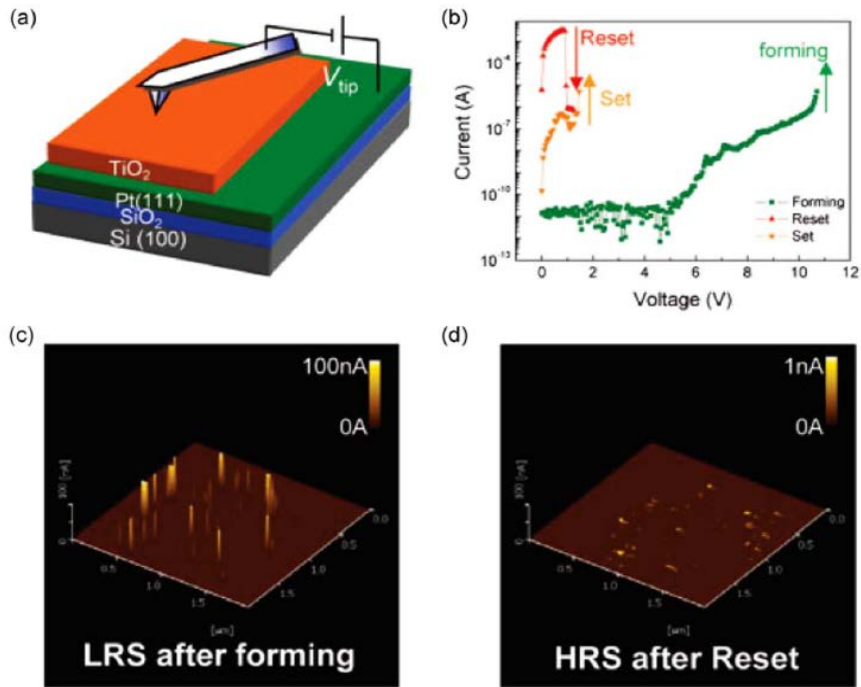


Figure 2.2.2 C-AFM on TiO₂ films. (a) Schematic diagram of the C-AFM measurements. (b) I - V curves using the conducting AFM tip as a top electrode clearly show the forming, reset, and set operations. (c) Mapping of the current flow through the surface just after the forming operation with 8 V shows locally distributed conducting regions. (d) After the reset operation with 1 V, the TiO₂ surface in the HRS state shows that the locally distributed conducting regions disappear. [30]

2.2.2 Interface model

The other resistive switching mechanism is an interface-type model, in which the resistive switching takes place at the interface between the metal electrode and the oxide. Using multi-lead resistance measurements on perovskite oxide cells, Baikalov et al. have recently shown that the contact resistance between the metal electrode and the perovskite oxide changes upon the application of an electric field. [31] This switching model is usually related to the bipolar-type resistive switching behavior. One can easily understand the interface model that the change in the oxidation state by the analogy of anodic oxidation. The redox reaction was evidenced optically in the Fe-O-based ReRAM. [8] Raman microspectroscopy on the lateral device and four-electrode transport measurements revealed that the resistance switching could be explained as a redox reaction between Fe_3O_4 and Fe_2O_3 at the interface near the anode. Another evidence for the redox reaction at the electrode interface in a Pt/TaO_x/Pt memory cell was confirmed by hard X-ray photoemission spectroscopy (HX-PES). [11] Fig. 2.2.3 shows Ta 4d HX-PES spectra of a TaO_x large-area test vehicle. The spectra clearly show the correspondence of the reduced TaO_x component to the change in the resistance state. Wei et al. claimed that the resistance switching occurred upon changing the barrier height between the anode and TaO_x, caused by the redox

reaction. The interface layer included $\text{Ta}_2\text{O}_{5-\delta}$ and $\text{TaO}_{2-\beta}$. In the reset operation, by applying a positive voltage pulse to the anode electrode, O^{2-} ions migrated and the oxidization reaction of the $\text{TaO}_{2-\beta}$ and O^{2-} led to the formation of $\text{Ta}_2\text{O}_{5-\delta}$. Increasing the $\text{Ta}_2\text{O}_{5-\delta}$ component enlarged the bandgap and increased the Schottky barrier height (SBH) at the interface. For the set operation, the reduction reaction of the $\text{Ta}_2\text{O}_{5-\delta}$ by applying the negative voltage pulse on the anode electrode decreased the SBH. Therefore, the switching behavior of Ta_2O_5 can be classified as BRS. The interface switching mechanism from SBH was also confirmed by Sawa et al. [32] The C–V curve for the Ti/PCMO interface shows hysteretic behavior, and C is larger in the LRS than in the HRS. This suggests that W_d is narrower in the LRS than in the HRS (Fig. 2.2.4). Electrons possibly pass through the thin Schottky-like barrier via a tunneling process in the LRS, whereas the thick barrier in the HRS prevents tunneling. Electrochemical migration of oxygen vacancies in the vicinity of the interface is considered to be the driving mechanism for the change in W_d .

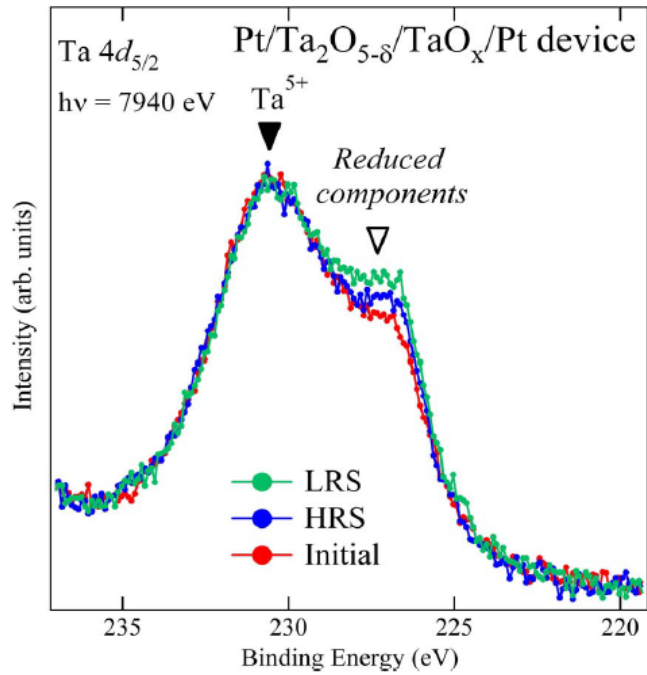


Figure 2.2.3 Ta 4d HX-PES spectra of TaO_x large-area test vehicle. The height of the reduced TaO_x component corresponds to the change of the resistance state, the low resistance state (LRS), the high resistance state (HRS), and the initial state showing the highest resistance state.

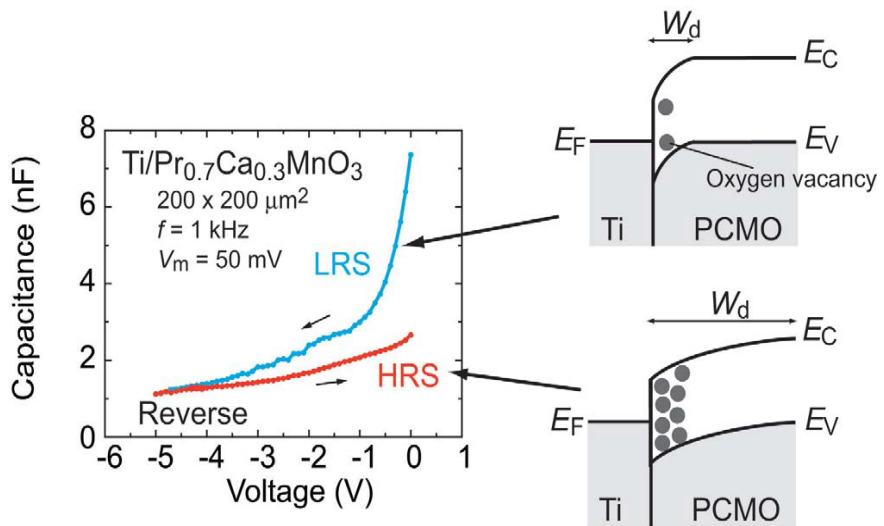


Figure 2.2.4 C–V curves under reverse bias for a Ti/PCMO/SRO cell show hysteretic behavior. This indicates that the depletion layer width (W_d) at the Ti/PCMO interface is altered by applying an electric field. [32]

2.3 Sb₂O₅ as a resistance switching material

Before Sb₂O₅ as a resistive switching material, it is widely used as an optical material because it possesses a high refractive index and high abrasive resistance. [33] As a resistance switching materials, Sb₂O₅ has been reported firstly in 2012 by this research. [34, 35]

A great interest of Sb₂O₅ as resistive switching materials is it has both URS and BRS phenomena. Both curves measured in Sb/Sb₂O₅/Pt structure are shown in figure 2.3.1. A detailed resistive switching properties and mechanism will be discussed chapter 4. Most of binary metal oxide materials show the URS behavior. At the same time, it is the base material of well-known perovskite materials such as SrTiO₃ and BaTiO₃ that show a BRS. [16] Because both URS and BRS are shown in Sb₂O₅ films, it can suggest a crucial clue of recognizing the nature of resistive switching mechanism.

In a material scope, Sb₂O₅ is included in pnictogen metal oxides and it has very low Gibbs free energy for formation per one O₂ mole ($\Delta G_f = -331.6$ kJ at R.T.) and low melting point (904 K). These properties may offer a viable root for obtaining the low switching power due to the weak bonding and the faster oxygen diffusion according to the low T_m. [36, 37]

In the point of ReRAM application, both URS and BRS in Sb₂O₅ films have its own advantages and disadvantages. URS has relatively wide

switching margin because of high on/off ratio and non-bias polarity while too high reset current is considered as a critical problem. Although BRS has small on/off resistance ratio, the switching speed is faster and reset current is lower than that of URS. In this thesis, the origin of URS and BRS phenomena and its own characteristics will be discussed.

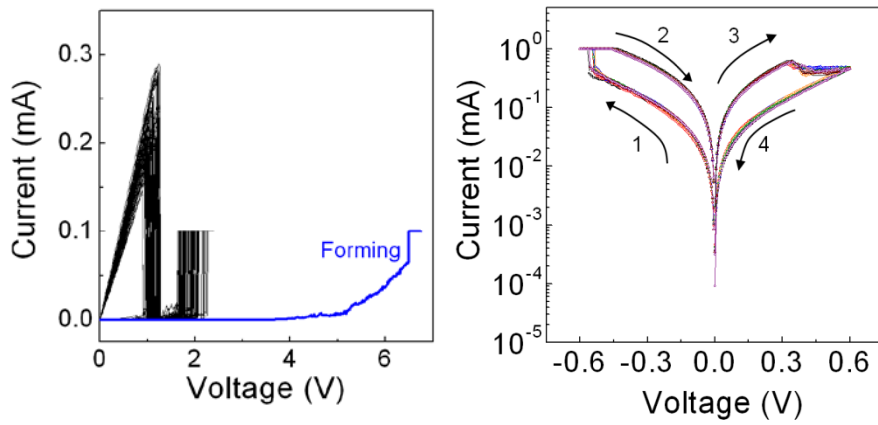


Figure 2.3.1 Unipolar and bipolar resistance switching curves in Sb_2O_5

2.4 Electronic conduction mechanism in metal-insulator-metal (MIM) structure

It has been reported that the I - V behaviors in the LRS of ReRAM device can be well explained by the Ohmic conduction and that they are quite reproducible during repeated switching experiments. However, the conduction behavior in the HRS is much more complicated and less reproducible. Therefore, the studying about conduction mechanism in HRS offers direct clues to understanding the resistive switching process.

2.4.1. The thermionic (Schottky) current [38]

When the electrons of a metal/insulator/metal (MIM) structure travel through the insulating layer without scattering due to phonons or impurities, the current is limited only by the electrode injection phenomena. The thermionic current (also called Schottky current) is one of electrode-limited current, and it is due to the electrons which transit above the potential barrier, i.e. those of energy $E > \phi_m$, as illustrated in Fig. 2.4.1 (figure in which ϕ_0 represents the metal-insulator barrier height without image force effect).

From the electronic current equation in MIM, the electronic current density can be written as follows;

$$J = \frac{4\pi q k_B^2 m^* T^2}{h^3} \exp\left(-\frac{\phi_o}{k_B T}\right) \exp\left(\frac{\beta_s E^2}{k_B T}\right)$$

with

$$\beta_s = \left(\frac{q}{4\pi\epsilon_0\epsilon_i E}\right)^{\frac{1}{2}}$$

β_s is called Schottky constant, which is defined as $\beta_s = 3.8 * 10^{-4} (\epsilon_i)^{-1/2}$. This equation is the Richardson-Schottky equation.

Thus, the Schottky current flow is a thermally activated process. The activation energy is $\phi_o - \beta_s E^{1/2}$, the difference between the metal-insulator barrier height ϕ_o and the barrier lowering due to the image force effect $\beta_s E^{1/2}$.

Schottky analysis followed the standard procedure; the various I - V curves were plotted on $\ln(I/T^2)$ versus $V^{1/2}$ and the Schottky V region was found. Then, $\ln(I/T^2)$ was plotted with respect to $1/T$ in the Schottky V region, and the variation of activation energy obtained from the slopes was plotted as a function of $V^{1/2}$. During the analysis, it was found that V and T region for Schottky fitting was quite narrow due to the interference with the Ohmic current and others.

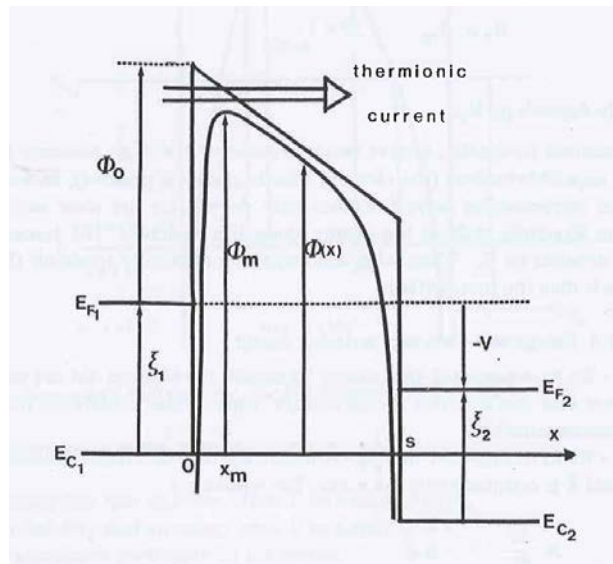


Figure 2.4.1 Energy diagram for a symmetrical MIM structure. [38]

2.4.2 The Poole-Frenkel current [38]

In the case of an Ohmic contact between electrode and insulator, when the insulator-metal interface is injecting, the current is limited by a bulk effect, which means electronic conduction property is dependent on the characteristics of the insulator. In an insulator, there can be exist in deep donor levels. There also often exist shallow electron traps, such as oxygen vacancy or defects. In this case, when an electron travels in insulator, it easily gets trapped by electron traps. An electronic conduction can still proceed if the electron can transit from one trapping site to the next. The barrier height ϕ_m of each trapping site depends on the various interactions, on the local electric field and on the distance separating the energy level of the trap and the lower edge of the insulator conduction band (ϕ_s in figure 2.4.2). An electron can overcome this barrier through a thermionic mechanism, when E_x , the energy of the electron along the x axis, is such that $E_x > \phi_m$ (so called Poole-Frenkel effect). In this case, electrons have enough energy to transit over the energy barrier whose height is given by equation 2.5.6. For calculating Poole-Frenkel current, it has various cases: thick or thin insulator, presence or absence of trapping sites.

$$\phi_m = \phi_s - \Delta\phi = \phi_s - \beta_{PF}E^{1/2}$$

$$\text{with } \beta_{\text{PF}} = \left(\frac{q}{\pi \epsilon_0 \epsilon_i} \right)^{\frac{1}{2}}$$

i) Thick insulator without traps

$$J = q(N_c N_D)^{1/2} \mu \exp\left(-\frac{\Phi_D}{2k_B T}\right) \exp\left(\frac{\beta_{\text{PF}}}{2k_B T} E^{\frac{1}{2}}\right) E$$

ii) Thick insulator with traps

$$J = q(N_c N_D)^{1/2} \mu \exp\left(-\frac{\Phi_D + \Phi_t}{2k_B T}\right) \exp\left(\frac{\beta_{\text{PF}}}{2k_B T} E^{\frac{1}{2}}\right) E$$

iii) Thin insulator with or without traps

$$J = qN_c \mu \exp\left(-\frac{\Phi_o}{k_B T}\right) \exp\left(\frac{\beta_{\text{PF}}}{k_B T} E^{\frac{1}{2}}\right) E$$

Here, N_c and N_D mean equivalent density of states in the insulator conduction band and donor atom concentration, respectively. In all cases, the quantity $\ln(J/E)$ varies linearly with $E^{1/2}$. The slope is equal to $\beta_{\text{PF}}/2k_B T$ for a thick insulator and to $\beta_{\text{PF}}/k_B T$ for a thin insulator.

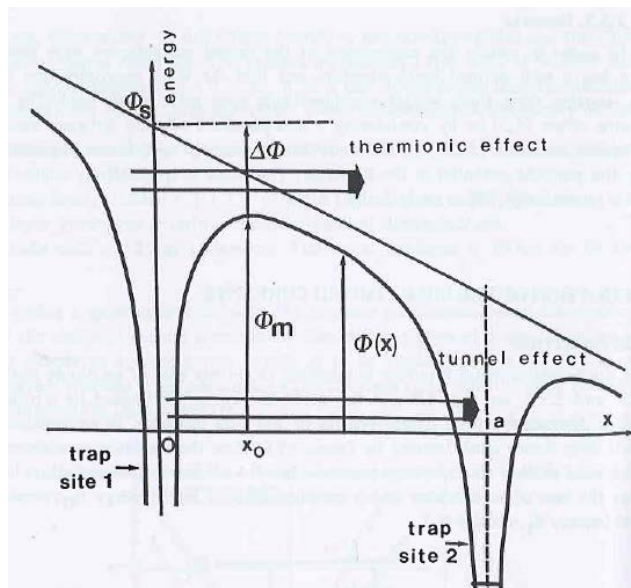


Figure 2.4.2 Schematic diagram of electronic potential energy in insulator containing a trap. [38]

2.4.3 Space-Charge-Limited current (SCLC) [38]

In Poole-Frenkel effect, it is supposed that the electric field was constant. When injection is strong, this hypothesis is no longer valid.

i) weak injection

In the case of weak injection of electron, the insulator charge density $\rho(x)$ can be ignored and the electric field, therefore, constant. This Ohmic conduction occurs as long as the insulator is electrically quasi-neutral. The current is as follows;

$$J = q n(x) \mu \frac{V}{s}$$

where, s is the insulator thickness, μ is the electron mobility.

ii) strong injection

For stronger injection, the insulator traps fill up and a space charge appears. The charge density is equal to $\rho(x) = -q n_t = -q n(x)/\theta$. From integrate Poisson's equation, the current density is as follows;

$$J = \frac{9}{8} \mu \frac{\epsilon_i \epsilon_0}{s^3} \theta V^2$$

J varies with V (Child's law). This behavior is typical of the space charge conduction behavior.

iii) very strong injection

When all traps are filled, the space charge is due to the conduction electrons with a charge density to $\rho(x) = -q n(x)$. The current expression is as follows;

$$J = \frac{9}{8} \mu \frac{\epsilon_i \epsilon_0}{S^3} V^2$$

By integrating Poisson's equation with $\rho(x) = -q N_t$, one can calculate trap-filled-limited voltage (V_{TFL}) defined as the limit between the strong injection and the very strong injection. It is as follows;

$$V_{TFL} = \frac{qN_t S^2}{2\epsilon_i \epsilon_0}$$

Figure 2.4.3 shows a rough diagram of the J(V) characteristics. When in the strong injection mode, the bias voltage reaches V_{TFL} , the traps get gradually saturated which means that the Fermi-level gets closer to the bottom of the conduction band. This results in a strong increase of the number of free electrons, thus explaining the increase of the current for $V = V_{TFL}$.

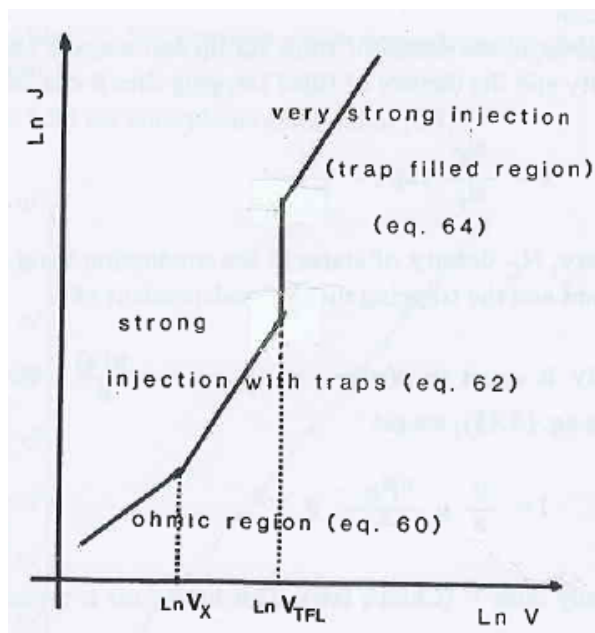


Figure 2.4.3 Variation of $\ln(J)$ as a function of V in the case of SCLC [38]

2.5 Bibliography

- [1] J. F. Dewald, A. D. Pearson, W. R. Northover, and W. F. Peck, Jr., J. Electrochem. Soc. 109, 243c (1962)
- [2] H. Shima, T. Nakano, and H. Akinaga, Appl. Phys. Lett., vol. 96, pp. 192107-1-192107-3, (2010).
- [3] Y. Hayashi, Appl. Phys. Lett., vol. 37, pp. 407-408, (1980).
- [4] C.-Y. Lin, D.-Y. Lee, S.-Y. Wang, C.-C. Lin, and T.-Y. Tseng, Surface Coatings Technol., vol. 203, pp. 628-631, (2008).
- [5] S. R. Lee, K. Char, D. C. Kim, R. Jung, S. Seo, X. S. Li, G.-S. Park, and I. K. Yoo, Appl. Phys. Lett., vol. 91, pp. 202115-1-202115-3, (2007).
- [6] H. Shima, F. Takano, H. Akinaga, Y. Tamai, I. H. Inoue, and H. Takagi, vol. 91, pp. 012901-1-012901-3, (2007).
- [7] T.-N. Fang, S. Kaza, S. Haddad, A. Chen, Y.-C. Wu, Z. Lan, S. Avanzino, D. Liao, C. Gopalan, S. Choi, S. Mahdavi, M. Buynoski, Y. Lin, C. Marrian, C. Bill, M. VanBuskirk, and M. Taguchi, in Tech. Dig. Int. Electron Devices Meeting, San Francisco, CA, (2006).
- [8] S. Muraoka, K. Osano, Y. Kanzawa, S. Mitani, S. Fujii, K. Katayama, Y. Katoh, Z. Wei, T. Mikawa, K. Arita, Y. Kawashima, R. Azuma, K. Kawai, K. Shimakawa, A. Odagawa, and T. Takagi, in Tech. Dig. Int. Electron Devices Meeting, Washington, DC, (2007).

- [9] Y. S. Chen, H. Y. Lee, P. S. Chen, P. Y. Gu, C. W. Chen, W. P. Lin, W. H. Liu, Y. Y. Hsu, S. S. Sheu, P. C. Chiang, W. S. Chen, F. T. Chen, C. H. Lien, and M.-J. Tsai, in Tech. Dig. Int. Electron Devices Meeting, San Francisco, CA, (2009).
- [10] C. Yoshida, M. Kurasawa, Y. M. Lee, M. Aoki, and Y. Sugiyama, Appl. Phys. Lett., vol. 92, pp. 113508-1-113508-3, (2008).
- [11] Z. Wei, Y. Kanzawa, K. Arita, Y. Katoh, K. Kawai, S. Muraoka, S. Mitani, S. Fujii, K. Katayama, M. Iijima, T. Mikawa, T. Ninomiya, R. Miyanaga, Y. Kawashima, K. Tsuji, A. Himeno, T. Okada, R. Azuma, K. Shimakawa, H. Sugaya, T. Takagi, R. Yasuhara, K. Horiba, H. Kumigashira, and M. Oshima, in Tech. Dig. Int. Electron Devices Meeting, San Francisco, CA, (2008).
- [12] D. S. Jeong, H. Schroeder, and R. Waser, Electrochem. Solid-State Lett., vol. 10, pp. G51-G53, (2007).
- [13] J. W. Seo, J.-W. Park, K. S. Lim, J.-H. Yang, and S. J. Kang, Appl. Phys. Lett., vol. 93, pp. 223505-1-223505-3, (2005).
- [14] S. Kim, I. Byun, I. Hwang, J. Kim, J. Choi, B. H. Park, S. Seo, M.-J. Lee, D. H. Seo, D.-S. Suh, Y.-S. Joung, and I.-K. Yoo, Jpn. J. Appl. Phys., vol. 44, pp. L345-L347, (2005).
- [15] R. Waser and M. Aono, Nature materials, 6, 883 (2003)
- [16] A. Sawa, Materials Today 11 (6), 28 (2008).
- [17] J. F. Gibbons and W. E. Beadle, vol. 7, pp. 785-797, (1964).

- [18] J. G. Simmons and R. R. Verderber, Proc. R. Soc. A., vol. 301, pp. 77-102, (1967).
- [19] C. J. Varker and E. M. Juleff, Proc. IEEE, vol. 55, no. 5, pp. 728-729, (1967).
- [20] D.H. Kwon, K.M. Kim, J.H. Jang, J.M. Jeon, M.H. Lee, G.H. Kim, X.S. Li, G.S. Park, B. Lee, and S. Han, Nature Nanotechnology 5 (2), 148 (2010).
- [21] Kinoshita, K., et al., Appl. Phys. Lett. (2006) 89, 103509
- [22] Kim, K. M., et al., Appl. Phys. Lett. (2007) 90, 242906
- [23] A. Chen, S. Haddad, Y. C. Wu, T. N. Fang, S. Kaza, and Z. Lan, Appl. Phys. Lett., vol. 92, pp. 013503-1-013503-3, (2008).
- [24] M.-J. Lee, S. Han, S. H. Jeon, B. H. Park, B. S. Kang, S.-E. Ahn, K. H. Kim, C. B. Lee, C. J. Kim, I.-K. Yoo, D. H. Seo, X.-S. Li, J.-B. Park, J.-H. Lee, and Y. Park, Nano Lett., vol. 9, pp. 1476-1481, (2009).
- [25] S. C. Chae, J. S. Lee, S. Kim, S. B. Lee, S. H. Chang, C. Liu, B. Kahng, H. Shin, D.-W. Kim, C. U. Jung, S. Seo, M.-J. Lee, and T. W. Noh, Adv. Mater., vol. 20, pp. 1154-1159, (2008).
- [26] B. J. Choi, D. S. Jeong, S. K. Kim, C. Rohde, S. Choi, J. H. Oh, H. J. Kim, C. S. Hwang, K. Szot, R. Waser, B. Reichenberg, and S. Tiedke, J. Appl. Phys., vol. 98, pp. 033715-1-033715-3, (2005).
- [27] U. Russo, D. Ielmini, C. Cagli, A. L. Lacaita, S. Spiga, C. Wiemer, M. Perego, and M. Fanciulli, in Tech. Dig. Int. Electron Devices Meeting,

Washington, DC, (2007).

- [28] C. Cagli, F. Nardi, and D. Ielmini, *IEEE Trans. Electron Devices*, vol. 56, no. 8, pp. 1712-1720, Aug. (2009).
- [29] K. M. Kim, G. H. Kim, S. J. Song, J. Y. Seok, M. H. Lee, J. H. Yoon, and C. S. Hwang, *Nanotechnology*, vol. 21, pp. 305203-1-305203-7, (2010).
- [30] C. Rohde, B. J. Choi, D. S. Jeong, S. Choi, J.-S. Zhao, and C. S. Hwang, *Appl. Phys. Lett.*, vol. 86, pp. 262907-1-262907-3, (2005).
- [31] Baikalov, A., et al., *Appl. Phys. Lett.* (2003) 83, 957
- [32] Sawa, A., et al., *Proc. SPIE* (2005) 5932, 59322C
- [33] H. Xiong, J. Chen, and D. Li, *Journal of materials chemistry*, 13, 1994–1998 (2003)
- [34] Y.B. Ahn, S.W. Ryu, J.H. Lee, J.W. Park, G.H. Kim, Y.S. Kim, J. Heo, C.S. Hwang, and H.J. Kim, *Journal of Applied Physics*, 112, 114105 (2012)
- [35] Y. Ahn, J.H. Lee, G.H. Kim, J.W. Park, J. Heo, S.W. Ryu, Y.S. Kim, C.S. Hwang, and H. J. Kim, *Journal of Applied Physics*, 112, 104105 (2012)
- [36] B. Ihsan, *Thermochemical data of pure substances*, Weinheim, Germany (1989).
- [37] E.M. Levin, C.R. Robbins, and H.F. McMurdie, *Phase Diagram for Ceramists*, Am. Ceram. Soc., Columbus, Ohio (1969).
- [38] G. Barbottin, A. Vapaille, *Instabilities in silicon devices*, North-Holland (1986)

3. Experimental procedure

3.1 DC sputtering system for thin films deposition

Outline figure of the sputtering system used for this study is shown in figure 3.1. Substrates were usually thermally oxidized 100 nm-thick SiO₂/Si wafer. Vacuum system is composed of a turbomolecular pump with a rotary pump; base pressure could be reached below 9×10^{-7} Torr. Ar, N₂, and O₂ gas can be supplied to the sputtering chamber for the adjustment of sputtering gas ambient. To enhance the uniformity of the deposited films, substrate holder was rotated during the film growth. 3-gun is fixed at the lid of the sputter and two DC and one RF power is equipped, which enables sputtering at most 3 targets at a same time. In this study, sputtering was done using the metal target described as follows.

- 1) Sb metal target + O₂ gas → Sb₂O₅ thin film on Pt/Ti/SiO₂/Si substrate
- 2) Sb metal target → Sb top electrode on Sb₂O₅/Pt/Ti/SiO₂/Si substrate
- 3) Ti metal target → TiN bottom electrode on SiO₂

Sb₂O₅ thin films were deposited by reactive dc magnetron sputtering on Pt/Ti/SiO₂/Si substrates. Table 3.1.1 summarizes the sputtering conditions of

Sb₂O₅ films in this study. 100-nm-thick TiN films were deposited on Si wafers with 100-nm-thick thermal oxide layer. The input DC power of Ti was fixed at 200W, and N₂ partial pressure was varied from 0 % to 9 % at 450 °C. The specifications of detailed deposition conditions for TiN films were summarized in Table. 3.1.2.

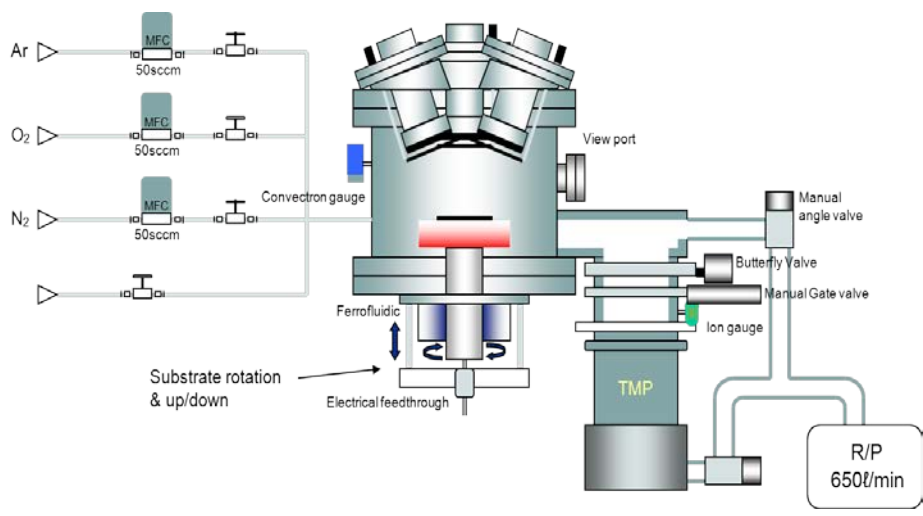


Figure 3.1.1 DC magnetron sputtering system of this study.

Table 3.1.1 Process conditions of the Sb₂O₅

Sputtering process conditions	
Base pressure	$< 5.0 \times 10^{-7}$ Torr
Process pressure	6 mTorr
Target-substrate distance	6 cm
Substrate rotation rate	15 rpm
Temperature	Room Temperature
Sputtering Gas (Ar) flow rate	10 sccm
Sputtering Gas (O ₂) flow rate	3 sccm

Table 3.1.2 Process conditions of TiN films

Sputtering process conditions	
Base pressure	$< 5.0 \times 10^{-7}$ Torr
Process pressure	6 mTorr
Target-substrate distance	6 cm
Substrate rotation rate	15 rpm
Temperature	450 °C
Sputtering Gas (Ar) flow rate	10 sccm
Sputtering Gas (N ₂) flow rate	0 ~ 1.0 sccm

3.2 Analysis methods

The crystallinity of the grown films was analyzed by glancing angle X-ray diffraction (GAXRD, PANalytical, X'Pert PRO MPD) under Cu K α radiation at 40 kV and 30 mA. The thickness and structure of the pristine Sb₂O₅ films were confirmed by cross-sectional TEM (JEOL, JEM-3000F). The chemical bonding states of the films were investigated by X-ray photoelectron spectroscopy (XPS, SIGMAPROBE). The binding energy was calibrated by setting C 1s peak to 284.5 eV. The change in the chemical nature and composition of the films was examined using depth profiling of the sample using Ar⁺ ion sputter-etching in the XPS chamber.

The chemical compositions of deposited films were examined using the Auger electron spectroscopy (AES, Perkin-Elmer 660) depth profiles. The rectangular shaped TEs of various areas were fabricated by photolithography and the lift-off process using 100-nm-thick sputtered Sb on the Sb₂O₅ films. The area of the Sb TE ranged from 1,600 μm^2 to 40,000 μm^2 . For studying the nature of CF in Sb₂O₅ after the set process, TEM specimens were prepared using a focused ion beam (FIB, SII Nanotechnology, SMI3050SE). From TEM analysis, electron diffraction and micrograph images of the CF phase in the Sb₂O₅ matrix were obtained. Digital Hot Plate/Stirrer Model HS30, San Marcos, CA, USA) was used at air ambient and sheet resistance was measured

with a 4-point probe (Advanced Instrument Technology, SR-2000N, Yongin, Republic of Korea) to determine the electrical resistivity of deposited films.

Electro-thermal simulation for studying of thermal effect in fabricated device was carried out on a 3D grid using the commercial program “CFD-ACE” by ESI-group. The material parameters, such as thermal conductivity (k), film density (q), specific heat (C_p), etc., were taken from bulk values. Electrical resistivity was calculated from the resistance of the low resistance state (LRS) obtained from I - V curve.

3.3 Switching methods for electrical characterization

Electrical characterization was made using capacitor-like metal-insulator-metal structure with circular top electrode. The resistive switching behaviors of these structures were measured at room temperature using an HP4145B semiconductor parameter analyzer.

Voltage sweep mode measurement is the most well-known method to analyze switching phenomena. Figure 3.3.1 shows typical resistive switching curves of Pt/Sb₂O₅/Pt structure using voltage sweep mode. At the first, an electroforming process is needed for soft breakdown of insulating layer as shown curve 1. The current compliance (I_{cc}) for the electroforming and set process was set in order to protect the samples from complete breakdown. After electroforming process, the resistance value of device had low which is shown curve 2 and is called to low resistance state (LRS). Then, voltage sweep is repeated again from LRS, a sudden current drop can be appeared at a certain voltage and this process is called “reset” process. In high resistance state (HRS), voltage sweep is started 0 V with limiting I_{cc} and a sudden current jump occurs which is similar with electroforming process at smaller voltage than forming voltage is observed. In this process, the resistance state is changed from HRS to LRS and it is called “set” process. The set and reset process can be repeated so that the resistance state can be controlled using

voltage sweep.

The HRS in BRS phenomenon can be obtained using positive bias, and then negative bias can make set process. At a specific voltage in negative bias sweep, there happen current jump similar with URS set. In URS, I_{cc} should be applied for protecting permanent breakdown of insulating layer. In BRS, however, current jump stops itself without any external compliance current, therefore, I_{cc} in BRS is not essential. But by applying I_{cc} in BRS at the current jump, the resistance of LRS can be maintained uniformly. Therefore, in this studying, the I_{cc} was also limited during voltage sweep mode for BRS characterization. The voltage sweep method in BRS is similar with method of URS, however, set process was carried out using negative bias.

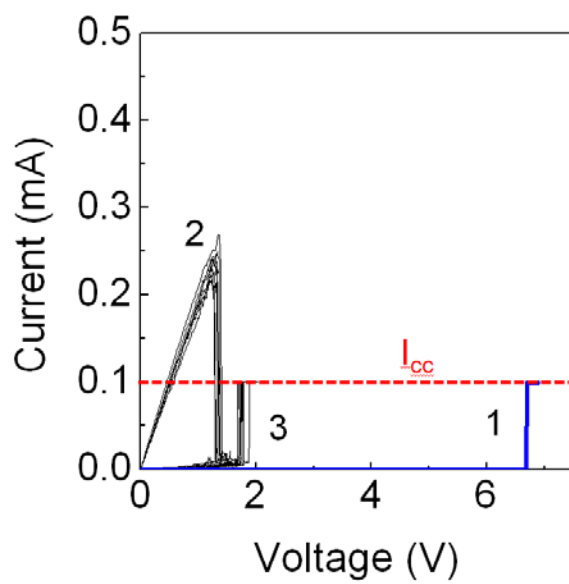


Figure 3.3.1 Typical I - V curves of URS in Pt/Sb₂O₅/Pt structure

4. Results and Discussions

4.1 Unipolar resistive switching properties of Sb_2O_5 films

4.1.1 Introduction

Resistive switching (RS) oxide materials, including various binary metal oxides (BMO) and perovskite structured ternary oxides, have been researched extensively for application to next-generation nonvolatile memory. [1] Among the many candidate materials for resistive random access memory (ReRAM) applications, BMOs have emerged as promising materials due to their simple chemical composition and their compatibility with current complementary metal-oxide semiconductor technology. [2]

The RS characteristics of many materials are duly classified into unipolar resistive switching (URS) and bipolar resistive switching (BRS) mechanisms according to the bias polarities required to induce the set (switching from high resistance state (HRS) to low resistance state (LRS)) and reset (switching from LRS to HRS) processes, although the exact microscopic mechanisms are diverse. [3] While these two mechanisms were initially considered to have quite distinctive origins, Jeong et al. already reported that both the URS and BRS mechanisms can be induced in a single material system ($\text{Pt}/\text{TiO}_2/\text{Pt}$) by

appropriate control of the switching sequences. [4] Recently, Kim et al. [5] and Yoon et al. [6] reported that correlations between URS and BRS mechanism can be well explained by the BRS-type switching in the ruptured region of the conducting filament (CF) in TiO_2 , whose formation and rupture are the origins of the URS in the same material. Although there are several cases where the CF does not play a critical role in their RS, which is typically characterized by the area-independent current density of the LRS, most of the RS in BMO appears to have a close correlation with the CF-related mechanism as in the TiO_2 case. Therefore, understanding on the nature of CF in many RS-BMO materials is of crucial importance.

The formation a CF in oxide materials is generally considered to be related with the formation of highly dense oxygen vacancies (V_o) or metal interstitial atoms, whose densities are usually higher than the thermodynamic stability range. These effects become possible by the simultaneous action of an electric field and thermal effect by the Joule heating, and their percolation. The percolated electrical conduction path can be of oxygen deficient entity as in Ta_2O_5 [7] and TiO_2 [8] or of metal excessive one as in NiO. [9] CF can be composed of even separate conducting phases, such as Magnéli phases ($\text{Ti}_n\text{O}_{2n-1}$, where $n =$ typically 4–5) in TiO_2 , or composed of dendritic metallic branches, such as Ni-filaments in NiO. The shape and direction of CF growth also depend on the types of materials, electrode, etc. suggesting the rich electrical-physico-chemical nature of RS behavior. [10] These diverse

characteristics must be closely correlated with 1) the bonding nature between the various metal and oxygen and 2) phase stability of solid solutions and possible intermediate phases. As mentioned above, TiO_2 is a typical material system which contains many metastable intermediate Magnéli phases, which are electrically much more conducting than the insulating mother phase. Similar materials are WO_3 and MoO_3 . Therefore, it must be reasonable to induce these conducting intermediate phases during the RS of these materials. [8,11] In contrast, NiO has almost negligible solid solubility of the two end members (Ni and NiO) in its phase diagram; therefore, the formation of metallic Ni CF can be understood from the phase diagram. [12] HfO_2 and Ta_2O_5 are perhaps the materials with intermediate properties in terms of phase stability; HfO_2 has a rather high stability range of hypo-stoichiometry of oxygen, although Hf barely has solid solubility to oxygen. [13] On the other hand, Ta has rather extensive oxygen solubility while Ta_2O_5 has a highly limited oxygen non-stoichiometry range. [14] Both of them do not show stable intermediate phases with high electrical conductivity. Therefore, these materials could have CFs that are composed of highly oxygen non-stoichiometric materials but the structure of their mother phases may be still retained.

Another viable aspect to examine the RS of various BMO materials is to look at the binding energy between the metal and oxygen ions. Since most of the BMOs are insulators with sufficiently large energy band gaps (E_g , see

table 4.1.1), the loss of oxygen is a prerequisite when observing the RS in these materials. Therefore, the binding energy, which could be represented by the Gibb's free energy of formation per molecular oxygen (ΔG_f , shown in Fig. 4.1.1), could be an important parameter that governs the various switching parameters such as switching voltage, current, speed, and reliability. It can be expected that a material with a higher binding energy would require a higher switching energy and involve a lower switching speed due to its difficulty in losing oxygen by electrical stimuli. However, once the local conduction path is formed, the recovery of the insulating property can be facilitated by the higher binding energy, so that the reset process can be accelerated. [7] A material with a lower binding energy can be advantageous in forming the CF but too easy loss of oxygen could make the material vulnerable to so called set-stuck problem with low reliability. E_g appears to play a certain role too. If it is too high, as in the cases of Al_2O_3 and SiO_2 , even though its ΔG_f is not so high, reliable RS can hardly be observed, as in Al_2O_3 , [15] or highly unusual RS mechanism which is independent of the redox reaction of the material is observed, such as in SiO_2 . [16] The non-transition nature of the metal ions in these materials also contributes to the difficulty in RS. The physical parameters of these materials are summarized in table 4.1.1.

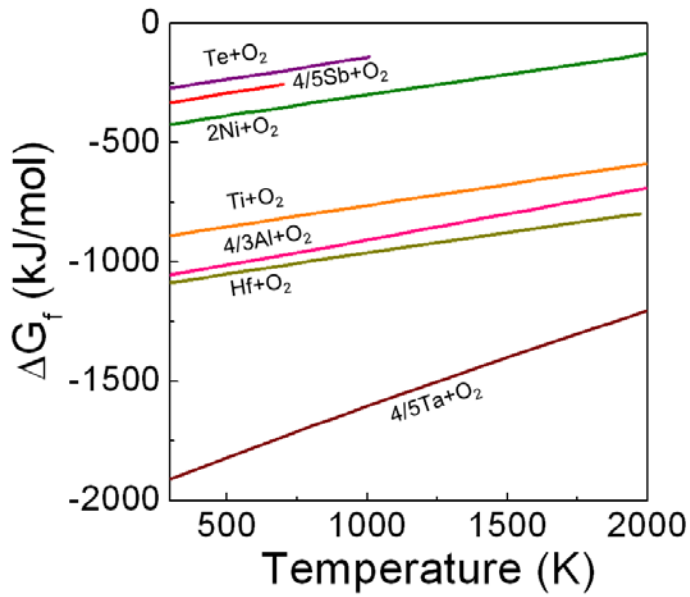


Figure 4.1.1 Temperature dependence of the Gibbs free energy of formation per one O₂ mole of various transition metal oxides. [35]

Table 4.1.1 Physical properties of various BMO materials for ReRAM application [12-14, 30-33]

Physical property	TMOs				Non-TMOs			
	TiO ₂	NiO	HfO ₂	Ta ₂ O ₅	Al ₂ O ₃	SiO ₂	Sb ₂ O ₅	TeO ₂
E _g (eV)	3.5	3.7	5.7	4.4	8.8	9	3	3.4
T _m (°C)	>1800	>1600	>2700	1880	>2000	~1100	525	733

While earlier studies on the RS of BMO materials focused on materials with distinctive second phases, such as TiO_2 or NiO , due to the formation and rupture of evident CFs, recent studies have focused more on materials with less-evident phase transitions with higher binding energy, such as HfO_2 and Ta_2O_5 , because of their higher reliability. [7,17] Nevertheless, it is still technically important to examine the RS of a material with far lower binding energy than those of typical transition metals oxides (TMO) for lower power consumption.

Antimony (Sb) is a pnictogen element and Sb_2O_5 is known as a stable oxide compound of Sb, which is an n-type semiconductor with an E_g of ~ 3 eV (Table 4.1.1). As can be understood from Fig. 1 and table I, the ΔG_f and melting point (T_m) of this pnictogen oxide are one of the lowest among the various BMOs. These properties may offer a viable root for obtaining the low switching power due to the weak bonding and the faster oxygen diffusion according to the low T_m .

In this chapter, Sb_2O_5 films were deposited on Pt electrodes by the reactive sputtering technique and their URS properties were examined. Sb_2O_5 films lost oxygen very easily during repeated URS cycling test when the Pt top electrode (TE) was adopted, and this loss usually led to failure after only several tens of RS cycles. However, oxygen loss of Sb_2O_5 films could be controlled by adopting Sb TE. Once the appropriate fabrication and electrical switching conditions were selected, the Sb_2O_5 films showed higher switching

performance in terms of a small switching current than that of other various oxide materials for URS application.

The variations in the chemical structure of the as-prepared Sb_2O_5 films for different TEs were examined and correlated with the observed RS characteristics. The detailed role of oxygen vacancies or metal clusters in the formation of CF was proposed based on an in-depth analysis of the chemical binding state, and the nature of CF in Sb_2O_5 films was revealed by high resolution transmission electron microscopy (HRTEM) analysis.

4.1.2 Experimental procedure

Antimony oxide thin films were deposited by reactive dc magnetron sputtering on Pt/Ti/SiO₂/Si substrates. The dc power for the deposition of the Sb target (3 inch in diameter) was fixed at 40W, and the oxygen content in the Ar and O₂ gas mixture was 23 %. The chamber pressure and substrate temperature were 6 mTorr and room temperature, respectively, during the sputtering. Then, 100nm-thick Pt or Sb was formed by using e-beam evaporation and dc magnetron sputtering, respectively. The Pt/Sb₂O₅/Pt (PSP) and Sb/Sb₂O₅/Pt (SSP) structures were used for the measurement of electrical characteristics.

The crystallinity of the grown films was analyzed by glancing angle X-ray diffraction (GAXRD, PANalytical, X'Pert PRO MPD) under Cu K α radiation at 40 kV and 30 mA. The thickness and structure of the pristine Sb₂O₅ films were confirmed by cross-sectional TEM (JEOL, JEM-3000F). The chemical bonding states of the films were investigated by X-ray photoelectron spectroscopy (XPS, SIGMAPROBE). The binding energy was calibrated by setting C 1s peak to 284.5 eV. The change in the chemical nature and composition of the films was also examined using depth profiling of the sample using Ar⁺ ion sputter-etching with an acceleration voltage of 2 kV in the XPS chamber. The chemical composition of the PSP and SSP samples were also examined using the Auger electron spectroscopy (AES, Perkin-

Elmer 660) depth profiles. The thickness of the Pt top electrodes for XPS and AES depth profiling were ~40 nm because Pt could not be easily etched by the sputtering process using accelerated Ar⁺ ions. The Pt and Sb TE were patterned into a circular shape with diameter of 300 μm through a metal shadow mask. In addition, rectangular shaped TEs of various areas were fabricated by photolithography and the lift-off process using 100-nm-thick sputtered Sb on the Sb₂O₅ films. The area of the Sb TE ranged from 1,600 μm² to 40,000 μm². The RS characteristics of the PSP and SSP were measured with an HP4145A semiconductor parameter analyzer at room temperature. The resistances of HRS and LRS were measured at 0.1 V. During RS, the top electrode was biased positively or negatively, while the bottom electrode was grounded. For studying the nature of CF in Sb₂O₅ after the set process, TEM specimens were prepared using a focused ion beam (FIB, SII Nanotechnology, SMI3050SE). With these specimens, the dielectrics influenced by the set process could be directly observed. From TEM analysis, electron diffraction and micrograph images of the CF phase in the Sb₂O₅ matrix were obtained. CF was located at the spots where the TE was severely damaged by the abrupt evolution of oxygen gas. [8]

4.1.3 Results and discussions

4.1.3-1 Crystal structure and chemical status of Sb₂O₅ films

Figure 4.1.2 (a) shows the GAXRD results of the Sb₂O₅ layers which were deposited on the Pt (100 nm)/Ti (10 nm)/SiO₂ (100 nm)/Si substrate. Only the obvious peaks from Pt were observed, suggesting that the as-grown Sb₂O₅ films were amorphous. The cross-sectional TEM image shown in Fig. 4.1.2 (b) also confirmed that the structure of the ~30nm-thick Sb₂O₅ films having Pt TE and BE is amorphous.

XPS depth profiling measurement was carried out to investigate the possible changes in the chemical state of the Sb₂O₅ layer when different TE materials are deposited. The Sb 3d and Pt 4f depth-profiling spectra for PSP are shown in Fig. 4.1.3 (a). In the Sb₂O₅ region, two peaks were detected at 530.7 and 540.1 eV, which coincided well with those of Sb₂O₅. [18] No peak was observed at 528 eV, which corresponds to metallic Sb 3d_{5/2}, indicating that Sb was fully oxidized to Sb⁵⁺ in the oxide layer. Considering the probing depth of the XPS (~ 5 nm), the red lines in Fig. 4.1.3(a) represents the binding status of Sb and Pt near the interface between the Sb₂O₅ films and the top and bottom Pt electrodes, respectively, because the XPS signals in these red lines include information on both Sb 3d and Pt 4f. Significant changes of the Sb 3d

peaks in both interface regions were not observed compared with that of Sb_2O_5 region, suggesting that there are hardly any chemical interactions between the Sb_2O_5 and Pt electrodes, which are reasonable considering the inert nature of Pt. This also suggests no oxygen diffusion from the Sb_2O_5 films to the Pt top and bottom electrodes when no electrical bias was applied. In the top and bottom Pt electrode regions, two Pt peaks were detected at 74.6 and 71.2 eV, which coincide well with those of metallic Pt. In contrast, the depth profiling results of the SSP sample shown in Fig. 4.1.3(b) were different from those of the PSP sample. The Sb 3d spectrum of the top electrode region showed that the Sb electrode already contained a non-negligible content of Sb_2O_5 as indicated by the peak at the binding energies of 530.7 and 540.1 eV. Oxygen can be incorporated into the Sb TE because of the residual oxygen in the sputtering chamber, as confirmed by the AES depth profiling results in Fig. 4.1.4 (b). Meanwhile, the clear emergence of the metallic Sb peak (at binding energy of 528.3 eV) at the TE interface (again indicated by the red lines) and even in the bulk of the Sb_2O_5 films region indicates that the oxygen diffused from the Sb_2O_5 layer into the Sb TE. Furthermore, the metallic Sb peak was still present even at the interface with the Pt BE, although the intensity decreased as the probing location deviated from the TE interface. In Pt BE region, only Pt 4f peaks were detected without any sign of an Sb 3d peak. These results suggest that the deposition of Sb TE induced a local reduction of Sb_2O_5 into Sb clusters by the outward diffusion of oxygen, and the Sb cluster

formation was not limited to only at the TE interface but down to the BE interface. This behavior was in accordance with the low oxygen binding energy and low T_m (high oxygen diffusivity) of Sb_2O_5 .

The microstructural change of Sb_2O_5 films by the Sb TE deposition was not confirmed by TEM. However, it was evident that the Sb clusters in SSP sample had not percolated to form the conduction channel in the pristine state, as can be understood from the still electrically insulating property of the SSP sample, although the leakage current was increased compared with the PSP sample (see Figs. 4.1.5 and 4.1.6). However, these Sb clusters are assumed to play a crucial role in forming CFs during the electroforming step in a well-controlled manner, and, thus, to contribute to the better reliability of the SSP sample compared with the PSP sample.

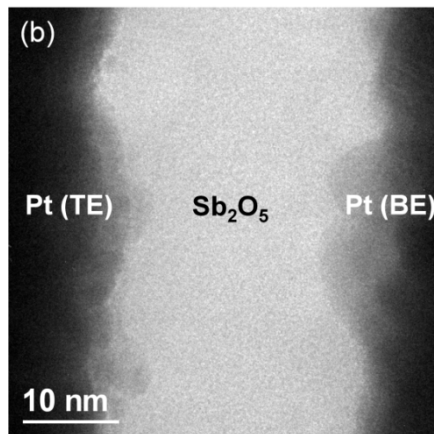
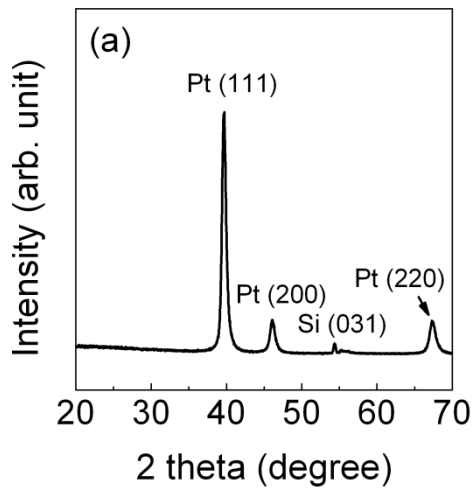


Figure 4.1.2 (a) Glancing angle X-ray diffraction patterns of Sb₂O₅ films on Pt/Ti/SiO₂/Si substrate, (b) High resolution TEM image of Pt/Sb₂O₅/Pt structure.

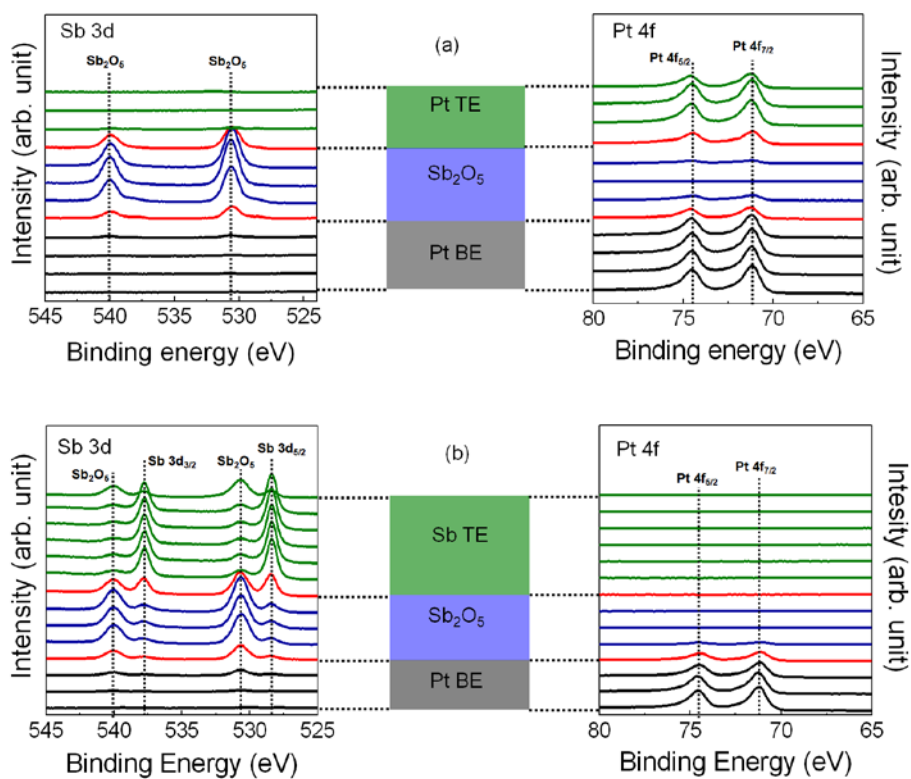


Figure 4.1.3 (a) XPS Sb 3d (left panel) and Pt 4f (right panel) depth profiling spectra for Pt/Sb₂O₅/Pt structure. (b) shows the XPS Sb 3d (left panel) and Pt 4f (right panel) depth profiling spectra of Sb/Sb₂O₅/Pt structure.

Figure 4.1.4 (a) shows the AES depth profiles of the PSP structure. Here, the atomic concentration was calculated based on the assumption that the atomic concentration ratio of Sb : O is 2 : 5 for a Sb_2O_5 films without any TEs. Both the TE and BE Pt layers have negligible concentrations of elements other than Pt. In the Sb_2O_5 region, a significant concentration of Pt was detected, which contradicts the XPS depth profiling results. It is believed that these results came from the high sputtering voltage (5 kV) for etching during the AES measurement, which results in the knock-on damage effect. A high sputtering voltage had to be used for etching because Pt cannot be easily etched with a low sputtering voltage. The AES results, anyway, corroborate the depth profile results in XPS of the same sample: oxygen did not diffuse from the Sb_2O_5 films to the Pt films and the Sb : O ratio in the oxide films was close to 2 : 5.

The AES depth profiles of the SSP structure are shown in Fig. 4.1.4 (b). Here, the applied sputter etching voltage was relatively lower than that used for the PSP structure because the top electrode Sb could be easily etched even with a low sputtering voltage (3 kV), even though the etching time did take a little longer, as indicated by the x-axis scale of the graph. However, low voltage of sputtering did not influence the analysis results. The Sb TE films had a relatively high oxygen concentration of ~20% near the Sb/ Sb_2O_5 interface, and the oxygen concentration slightly increased to ~30 % near the surface of the Sb TE because of the natural oxidation of the Sb TE during its

exposure to air. These results also coincide with the XPS results shown in Fig 4.1.2 (b). Despite the considerable oxygen concentration in the Sb films, the electrical resistivity of these oxygen-containing Sb films (100 nm) on the SiO₂ (100 nm)/Si substrate, measured by the four-point probe technique, was 278 $\mu\Omega\text{-cm}$, which was low enough for the Sb films to work as the TE in the SSP structure. In the Sb₂O₅ region (approximately from 30 min to 40 min sputtering time), the Sb concentration gradually decreased while the O concentration slightly increased with increasing sputtering time. In addition, the approximate atomic concentration ratio of Sb : O was 3 : 5 in the layer, suggesting that the deposition of Sb TE reduced the oxygen concentration of Sb₂O₅ films. The XPS data indicated that the structure of the oxide films was a mixture of Sb₂O₅ and Sb-cluster rather than a uniform Sb₂O₅ films. These induced Sb metallic clusters significantly affected the RS characteristics of Sb₂O₅ films as shown below.

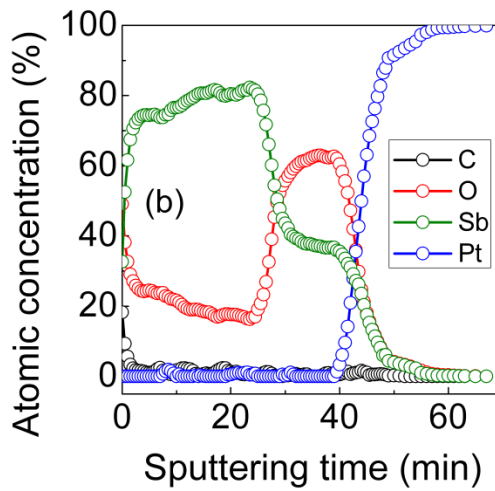
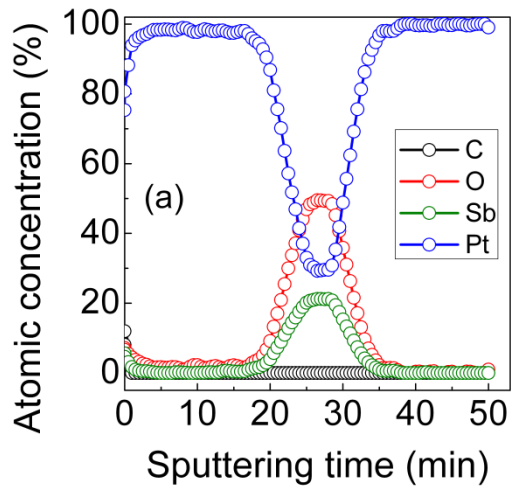


Figure 4.1.4 AES depth profiles results of (a) Pt/Sb₂O₅/Pt and (b) Sb/Sb₂O₅/Pt structures

4.1.3-2 Electrical characteristics of Sb₂O₅ films in PSP and SSP samples

The *I-V* curves showing the RS characteristics of PSP samples are shown in Fig. 4.1.5 (a). The current compliance (I_{cc}) for the forming and set processes was 0.1 mA. At the pristine stage, the films showed a very low current, and an abrupt jump of the current to I_{cc} was occurred by voltage sweep, which is called electroforming process. After the electroforming process, the films remained in LRS. The forming voltage (V_{form}) was ~ 6.5 V. When the films were in LRS, the current increased linearly with increasing voltage, and then suddenly dropped to a low level at ~ 1.2 V (reset voltage, V_{res}), where the films showed the HRS again. While sweeping again with I_{cc} , the current jumped abruptly at the set voltage (V_{set}) of ~ 2 V and the films switched back to LRS. The magnitude of the reset current (I_{res}) of Sb₂O₅ films was as low as 0.2 – 0.3 mA, which is generally much lower than those of other URS materials with a comparable electrode size (Table 4.1.2).

It has been reported that the strength of formed CF after the electroforming step or the subsequent set step has a strong influence on the I_{res} , which is commonly controlled by the I_{cc} value in voltage sweep modes. [23] When a voltage is applied to a pristine state RS films, current generally does not flow uniformly over the entire electrode area due to the involvement of defects, interface traps, and topographical inhomogeneity. In addition, a very high current density ($10^6 - 10^7$ A/cm²) is required to form CF. [8] Therefore, the

localized current flow in any BMO RS cell would actually promote CF formation, otherwise the current density would be too low to induce a CF (cf. $10 \text{ mA}/10^4 \mu\text{m}^2 = 10^2 \text{ A}/\text{cm}^2$). Thus, if the pristine films are highly leaky at the low voltage region, it would be difficult to induce electroforming since the current may be just used off by the leakage. The PSP sample showed a highly insulating property at the pristine state (see inset figure of Fig. 4.1.6 (a)), which is perhaps due to the amorphous nature of the Sb_2O_5 films and the high Schottky barrier height between Sb_2O_5 films and the Pt electrodes. Therefore, the current loss via the area which will eventually be the non-CF portion would be minimized.

In addition, as mentioned in the introduction, the binding energy between the Sb and O is quite low, so CF formation is facilitated even with a small I_{cc} . Although the I_{cc} was quite small, the resistance of Sb_2O_5 films on LRS was sufficiently low (10^3 - $10^4 \Omega$) compared with HRS ($>10^6 \Omega$) because of the highly concentrated current flow after the electroforming. Thanks to the highly localized current flow and the low T_m of Sb (904 K), [12] which was confirmed as the element of CF in Figures 4.1.11, the thermal rupture of the CF could be accomplished with small power dissipation, so that a low I_{res} was achieved. Kim et al. recently reported that the reset operation of TiO_2 might be achieved by melting Magnéli CFs with sufficient electric current and subsequent rapid cooling down. [10] Therefore, the magnitude of I_{res} is

proportional to Joule heating, which is required to increase temperature over T_m . Alternatively, the reset can proceed via the reoxidation of the CF material where the oxygen can be supplied from the nearby Sb_2O_5 material. T_m values of Sb is lower than those of the other CF phases, such as Magnéli (1700 K) of TiO_2 [10] and Ni (1728 K) of NiO. [22] The low T_m values of Sb and Sb_2O_5 suggest a higher drift-diffusion coefficient of oxygen ions. Thus, the low I_{res} in Sb_2O_5 films can be obtained. Although the URS generally features higher LRS/HRS current ratios than BRS, the large power dissipation during the reset process is one of the most significant obstacles for memory application. [24] Therefore, the low I_{res} of Sb_2O_5 is a promising feature of the material as an URS material for memory application.

A switching cycling test in the voltage sweep mode was carried out to evaluate the endurance characteristics of the PSP sample. Although there was a slight fluctuation of resistance in LRS (10^3 to $10^4 \Omega$) and HRS (10^6 to $10^7 \Omega$), reversible switching was observed for the first 25 cycles, as shown in Fig. 4.1.5 (b). The resistance ratios of HRS to LRS are in the range of 2 orders of magnitude. The set stuck phenomenon, however, was always observed only after ~25 cycles and the sample could no longer be reset. These early failures of PSP might have resulted from the severe oxygen consumption which takes place in Sb_2O_5 films during repeated URS.

At room temperature, the ΔG_f of Sb_2O_5 was only -331.6 kJ, which was lower than the values of other BMOs (Fig. 4.1.1). Even when the temperature

increased, the ΔG_f of Sb_2O_5 was still lower than those of other BMOs. Thus, the severe loss of oxygen from Sb_2O_5 can occur easily compared with other BMO materials. The phase diagram of the Sb-O system shows that there were only two intermediate phases (Sb_2O_3 and Sb_2O_4) and that the solid solubility of O into Sb and the non-stoichiometry of Sb_2O_5 were very limited. Even if Sb_2O_3 is crystallized, it cannot be the CF element in the Sb_2O_5 matrix because Sb_2O_3 has a large band gap ($E_g = 3$ eV) and high electrical resistivity ($\rho = 3 \times 10^{14} \mu\Omega\cdot\text{cm}$). [25] The values of E_g and electrical resistivity of Sb_2O_4 were also similar to the values of Sb_2O_3 films. [26] Therefore, when electrical stress is applied to the Sb_2O_5 matrix during the electroforming and set processes, it is believed that oxygen atoms are rejected from the oxide material and CF, which is composed of metallic Sb clusters, is formed. This was actually confirmed by the TEM experiment as shown below. As the number of switching cycles increased, the material became severely devoid of oxygen even only after several tens of cycles. Therefore, the PSP had unsuitable endurance properties for URS application, even though it showed superior switching power performance compared with other TMO materials.

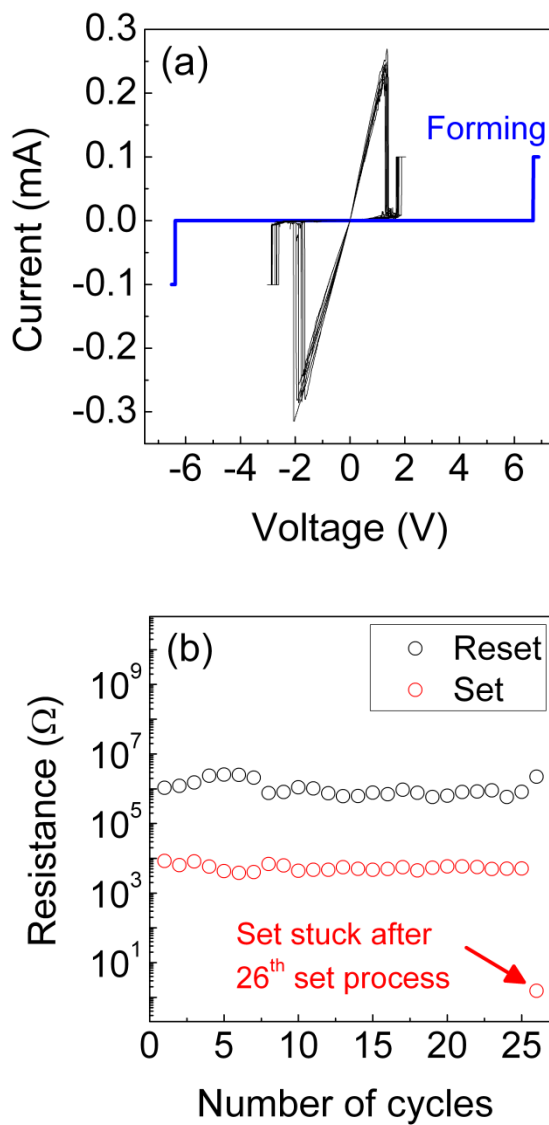


Figure 4.1.5 (a) The *I-V* results and (b) electrical endurance properties of Pt/Sb₂O₅/Pt structure.

Table 4.1.2 Reset current values of unipolar resistive switching material

Resistive switching material	Reset current	Reference
TiO ₂	~50 mA	[3], [10]
Nb ₂ O ₅	~10 mA	[20]
ZrO ₂	~20 mA	[21]
NiO	~20 mA	[9], [22]
CoO	~10 mA	[50]

In order to improve the endurance characteristics of Sb_2O_5 films, Sb metal was adopted as the TE instead of Pt (SSP device). Since Sb can actively extract oxygen from the Sb_2O_5 , generating oxygen vacancies or Sb clusters in Sb_2O_5 , the CF is expected to form without severe oxygen consumption during the electroforming. The I–V characteristics of 70 URS cycles of the SSP by positive voltage sweep with the electroforming step are shown in Fig. 4.1.6 (a). The I_{cc} during the electroforming and set operations was also 0.1 mA. V_{form} (~ 6.5 V), V_{set} ($\sim 1.6 - 2$ V), and I_{res} ($\sim 0.15 - 0.3$ mA) are similar to those of PSP. However, the leakage current value of the pristine SSP sample is higher than that of PSP (inset of Fig. 4.1.6 (a)), which could be due to the pre-existing Sb clusters in the Sb_2O_5 films. Figure 4.1.6 (b) shows the endurance characteristics of SSP. The minimum ratios of HRS to LRS (about 2 orders of magnitude) are maintained over 200 times of switching. Namely, the SSP structure had a far higher endurance property for the URS test than the PSP structure.

It is interesting to note that the power needed to induce the electroforming in both samples was quite similar although the SSP sample already had Sb-clusters in its pristine state. This implies that the energy that is necessary to induce the Sb clusters (or oxygen vacancies) in the Sb_2O_5 layer in PSP sample is minor compared with the energy that is necessary to percolate the Sb clusters to form the CF, meaning that CF formation appears to be mainly controlled by the percolation process. These effects led to the similar power

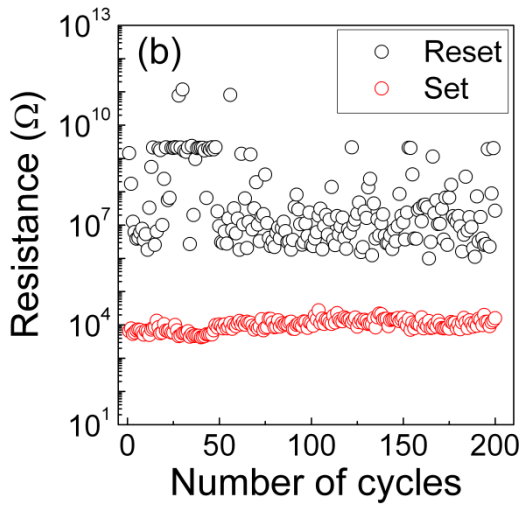
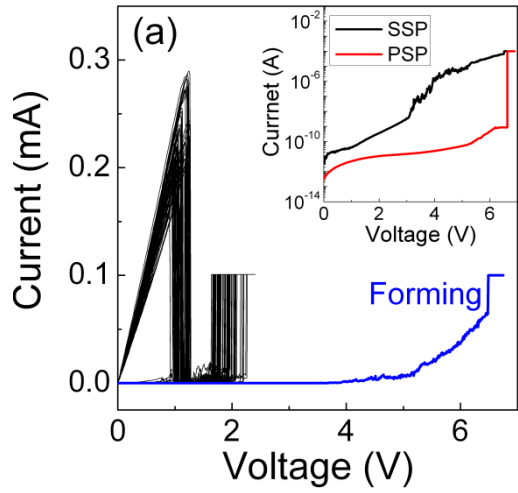


Figure 4.1.6 (a) The URS I - V characteristics of the Sb/Sb₂O₅/Pt structure. Inset figure shows the leakage current of SSP and PSP structure during electroforming process. (b) The electrical endurance characteristics of SSP structure.

consumption during electroforming process in both samples. The better endurance property of the SSP sample than that of PSP sample under this positive bias condition can be attributed to the less oxygen loss during the switching cycles, since

- 1) a severe reduction process in Sb_2O_5 matrix for CF formation can be reduced due to pre-existing Sb clusters and
- 2) Sb TE can act as an oxygen blocking layer while Pt TE cannot.

In fact, the Pt TE showed a severe local “explosion” of the electrode during the switching cycles due to the abrupt oxygen gas evolution, but Sb TE showed a much less gas evolution under the same condition.

While the PSP sample showed quite symmetrical URS characteristics with respect to the bias polarity, which is expected from the symmetrical electrode configuration, the SSP sample actually showed highly asymmetrical switching properties, even though the URS still proceeded at both bias polarities. Figure 4.1.7 (a) shows the I - V characteristics of a pristine SSP in the electroforming process with different values of I_{cc} under the negative bias polarity. For comparison, the electroforming curve for the positive bias polarity was also appended (red line marked with (+) bias), which shows the electroforming at ~ 6.6 V with 1 mA of I_{cc} . However, the electroforming under the negative bias required a much higher voltage and I_{cc} . When the I_{cc} was set

to -1 mA, the electroforming was not observed even when the negative voltage sweep reached -9.5 V. Therefore, subsequent negative voltage sweeps were tested while I_{cc} was increased from -1 to -8 mA from the same electrode. As the number of sweeps increased, the current level gradually increased but the electroforming was observed only when the I_{cc} was increased to -8 mA. This is in a clear contradiction with the PSP case, where the negative bias induced a similar electroforming to that of the positive bias. Figure 4.1.7 (b) shows the reversible I - V results of SSP using the negative voltage sweep mode. After the electroforming occurred at I_{cc} of -8 mA, reversible and stable URS was obtained even when I_{cc} was set to -1 mA. The oxygen ions are pushed toward the Pt BE under the negative bias condition, which may induce less efficient oxygen evolution due to the presence of the Si substrate. However, the oxygen evolution blocking effect by the Si substrate played a minor role, as evidenced by the efficient negative electroforming in PSP. Therefore, there must be another reason for such an inferior electroforming performance of SSP under this bias polarity; this reason is believed to be the oxygen ions present in the Sb TE. At the pristine stage, the Sb TE layer has a high oxygen concentration (20-30%) and the Sb_2O_5 layer has a Sb clusters (Fig. 4.1.8 (a)). CF formation during electroforming process in the Sb_2O_5 layer can be described by a nucleation and growth process of Sb clusters. When the positive voltage was applied to the TE, Sb clusters are generated by electro-thermal assisted redox reaction. The generated Sb cluster and already

present Sb cluster will be developed into the CF (Fig. 4.1.8 (b)). The induced oxygen ion by oxygen reduction process could be drifted and diffused to the anode interface by the applied bias. Hence, the CF can be easily formed without recombination process with oxygen ion. On the other hand, when the negative voltage was applied to the TE, the O^{2-} in the Sb_2O_5 and in the Sb electrode were influenced by the high electric field (a few hundreds kV/cm) and began to drift toward the bottom electrode. At the same time, the already present and switching voltage-induced Sb clusters in Sb_2O_5 started to establish the CF in Sb_2O_5 matrix. However, the drift of the oxygen ions that originated from the Sb TE can recombine with the Sb clusters near the interface between Sb and Sb_2O_5 , or even across the whole Sb_2O_5 layer so that CF may not be easily formed (Fig. 4.1.8 (c)). Hence, to form the CF in the pristine stage using negative voltage sweep, a larger electrical stress is needed than that of the positive voltage sweep.

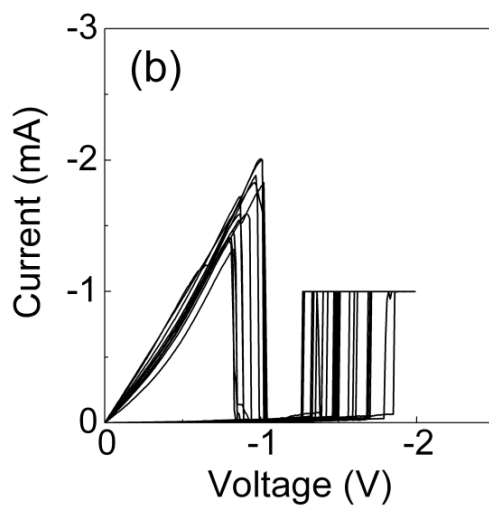
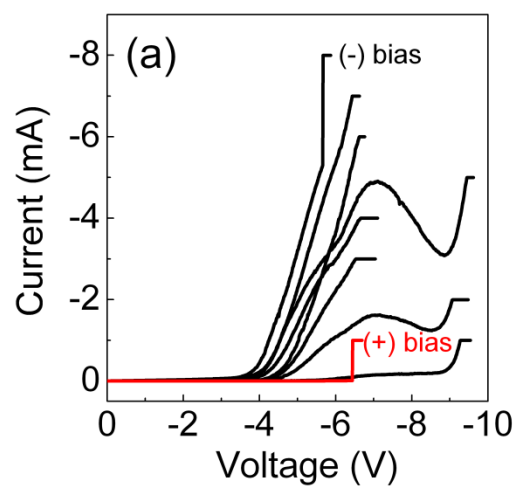


Figure 4.1.7 (a) The electroforming curves and (b) the URS $I-V$ curves after electroforming process with $I_{cc} = -8$ mA, respectively, of Sb/Sb₂O₅/Pt structure using negative voltage sweep mode.

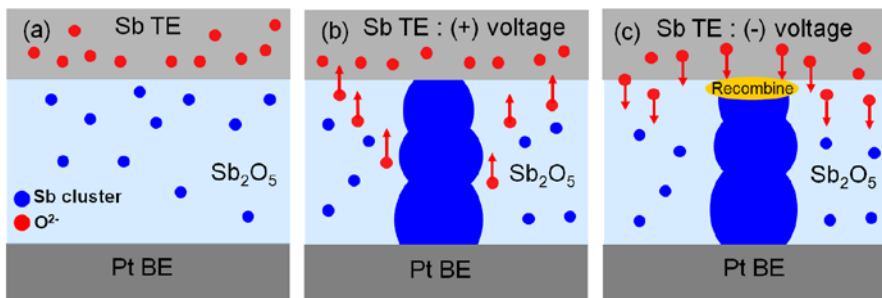


Figure 4.1.8 Schematic diagrams of oxygen ion and Sb cluster movement (a) at pristine state and (b) with high positive bias, and (c) with high negative bias.

4.1.3-3 Resistive switching of Sb_2O_5 films by localized filamentary mechanism

The lateral-area-localized switching behavior and microscopic nature of CF in the Sb_2O_5 films were studied. When the RS in oxide materials is confined to a much smaller area (as in the case of CF) compared with the electrode area, the magnitude of current at LRS should be independent of the device area. [27] Figures 4.1.9 (a) and (b) show the variations of the magnitudes of current and current density of the SSP sample in LRS as a function of sample area, respectively. The current was read at 0.5 V. The magnitudes of current were similar irrespective of the sample area down to $1,600 \mu\text{m}^2$. In addition, current density increased as the device area decreased. These results suggest that the current path of the Sb_2O_5 on LRS was localized. Therefore, it is believed that the RS characteristics of Sb_2O_5 films are controlled by the localized CF.

The general difficulty in observing the CF using TEM arises from its highly localized nature; it is difficult to find the location of the CF from a TEM sample if it is arbitrarily taken from the RS test structure. Therefore, the region of TE where the TE was blown-off (Figure 4.1.10 (a)) from the PSP in LRS was taken and the TEM sample was fabricated using the focused ion beam (FIB) technique (Figure 4.1.10 (b)). The blown off region might be

formed by oxygen explosion effect during electroforming or set process. The LRS sample experienced only 1 cycle (reset to set) after the electroforming process.

The bright field TEM (BF-TEM) images of the PSP structure are shown in Figs. 4.1.11 (a) - (c). In Figs. 4.1.11 (a) and (b), the TE Pt was not observed since it was blown-off. The image clearly shows that dark spots were generated in Sb_2O_5 amorphous films, which were not observed in the pristine state (see Fig. 4.1.2 (b)). A careful examination of the image revealed partially crystallized regions in the dark spots. In general, the differences in the contrast of BF-TEM images were due to the diffraction effect and the mass deviation of the elements composing the sample. The relatively high crystalline phase and heavy elements were shown darkly in BF-TEM image. Therefore, these dark spots were thought to be metallic clusters, which may act as the CF in Sb_2O_5 films.

In order to confirm this, high-resolution (HRTEM) images were taken from the same area, and their inversed fast Fourier transformed (IFFT) micrographs and FFT patterns were examined. Figures 4.1.11 (d) - (f) show the IFFT images that represent the crystalline regions of corresponding BF-TEM images in Figs. 4.1.11 (a) - (c). The crystalline regions from IFFT images coincide well with metallic cluster region in the HRTEM images. The FFT patterns shown in Fig. 4.1.11 (g) - (i) have clearly distinguishing diffraction spots that were not observed in the pristine amorphous Sb_2O_5

sample. In Figs. 4.1.11 (g) and (f), the diffraction spots of the crystalline regions correspond to d-spacings of 0.218 and 0.217 nm, respectively. Although the lattice spacing values of Pt (111) and Sb (110) are quite similar (0.215 [JCPDS card No. 85-0646] and 0.227 nm [JCPDS card No. 35-0732]), the absence of Pt TE near the portion where the FFT patterns were acquired suggests that these diffraction spots correspond to metallic Sb clusters. In addition, from the FFT pattern in Fig. 4.1.11 (i) of the area where the TE Pt was slightly retained (Fig. 4.1.11 (c)), the diffraction spots with d-spacings of 0.351 and 0.175 nm were obtained. These could be unambiguously identified as the (101) and (202) spots of the Sb phase with d-spacings of 0.354 nm (101) and 0.177 nm (202), because other possible d-spacing of Pt (100) of 0.392 nm, and (110) of 0.278 nm can hardly coincide with these spots. Therefore, it is believed that the metallic clusters in Sb_2O_5 films were the metallic Sb phase. The presence of a metallic Sb phase in the Sb_2O_5 films could be responsible for the observed RS behavior. Energy dispersive spectroscopy was also attempted to discern the chemical composition of the clusters, but the overlap of the phase with the matrix did not allow a precise assessment. From these TEM images, it can be understood that the CF structure of Sb_2O_5 is quite distinctive from those of other TMOs, such as TiO_2 or NiO . It is known that pristine TiO_2 films deposited by atomic layer deposition or sputtering process are in crystalline anatase or rutile phase over entire films. [28] In addition, the phase diagram of a Ti-O system is very complicated compared to those of

other TMOs, [12] containing the conducting sub-oxide phase such as Ti_4O_7 or Ti_5O_9 . Therefore, when electrical stress is applied to metal/ TiO_2 /metal structure, the CF in TiO_2 matrix is formed by phase transition from anatase or rutile phase to these conducting sub-oxide phases with conical CF shape. [29] Meanwhile, NiO does not have conducting the sub-oxide phase of NiO. Accordingly, a metallic Ni channel forms at the grain boundary of NiO films with dendritic configurations. [9, 22] Because the as-deposited Sb_2O_5 films are amorphous and no conducting sub-oxide phase exists, it is believed that the CF shape and formation mechanism in the Sb_2O_5 matrix is different from those of other TMOs having crystalline structures. Jung et al. reported that metallic nano-spots are created in the amorphous NbO_x films by electric field and CF is generated by growth and connection of metallic nano-dots. [20]

It is expected that the CF formation mechanism and structure in Sb_2O_5 films are also similar to those of amorphous NbO_x films. In the pristine stage of a PSP or SSP structure, the oxygen reduction process occurred easily with increasing external electrical stress due to low ΔG_f of Sb_2O_5 , and the metallic Sb clusters were created (Fig. 4.1.12 (a)), which will eventually evolved into the percolated path (Fig. 4.1.12 (b) and (c)), which is the CF. In Figs. 4.1.11 (a) - (c), various metallic Sb clusters are formed in the Sb_2O_5 matrix by electrical stress, and some metallic Sb clusters are crystallized as Sb. Therefore, it can be concluded that the URS phenomenon of Sb_2O_5 films is controlled by the formation and rupture of localized CF which is composed of metallic Sb.

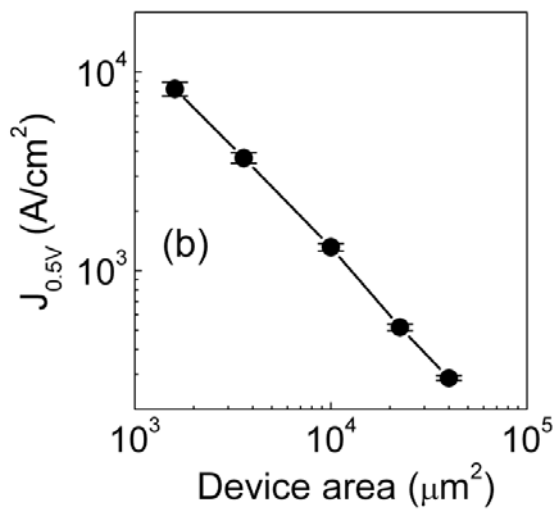
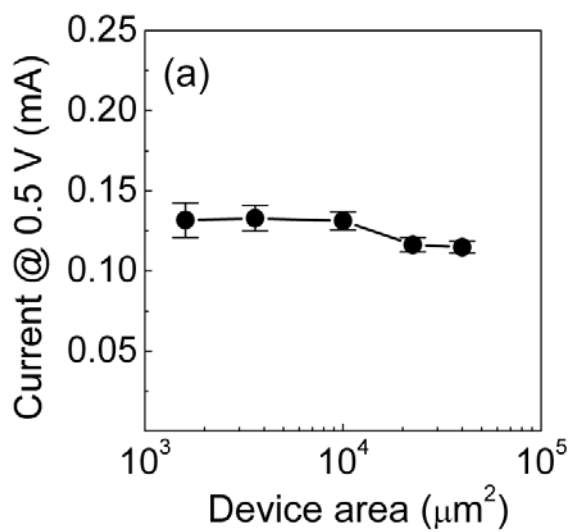


Figure 4.1.9 (a) The magnitude of current and (b) the current density of Sb/Sb₂O₅/Pt structure with various device area. The current values were read at V= 0.5 V

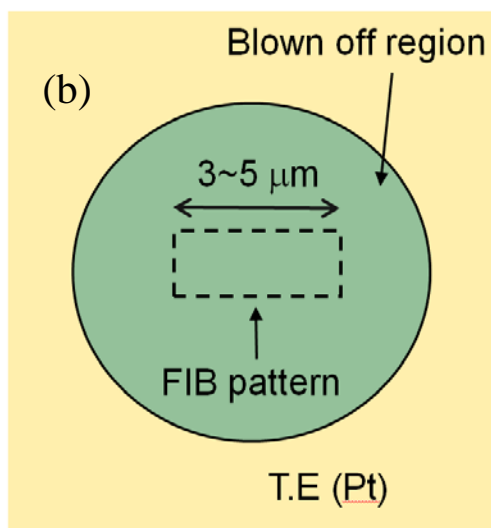
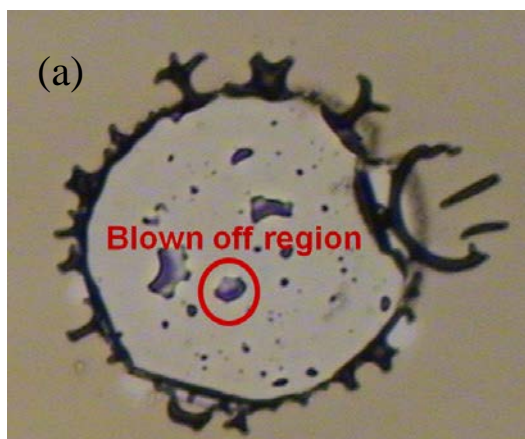


Fig 4.1.10 (a) The images of blown off region after electroforming process, (b) the schematic diagram of FIB patterns.

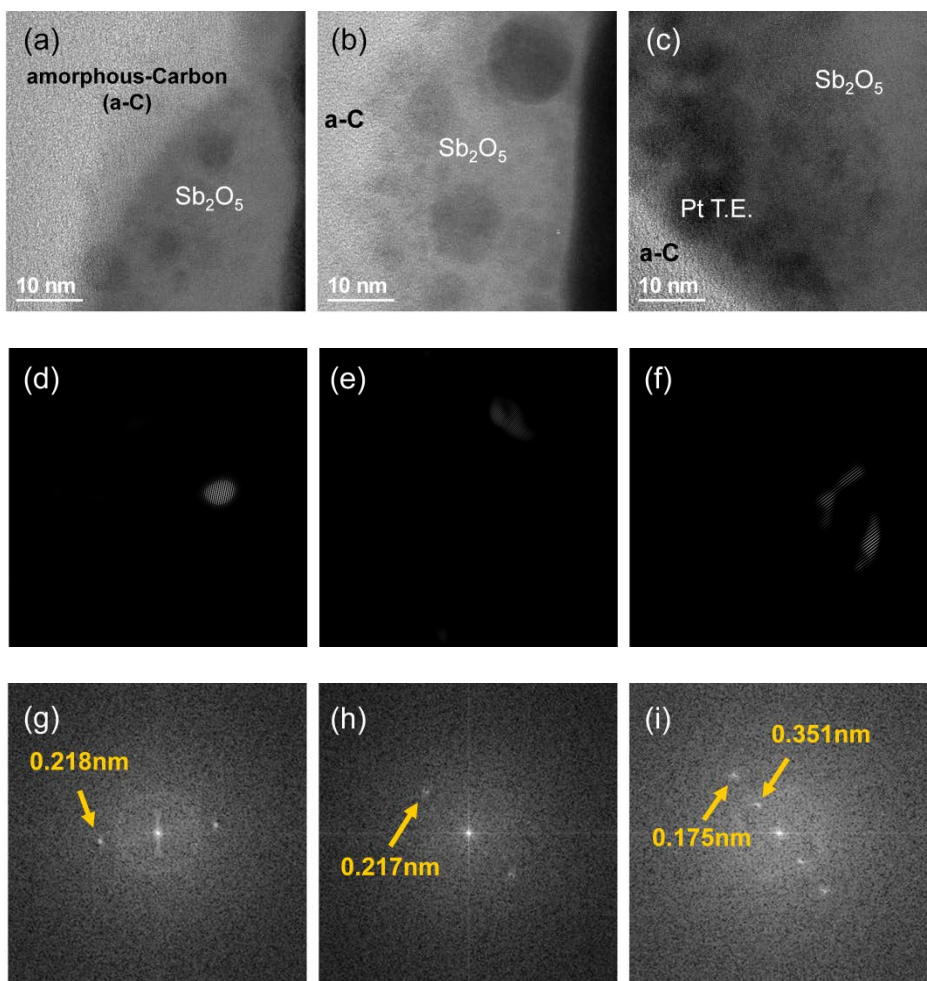


Figure 4.1.11 (a)~(c) The bright field TEM images of the Pt/Sb₂O₅/Pt structure after set process, (d)~(f) shows the inversed FFT images of fig. (a)~(c), respectively. (g)~(i) The FFT micrographs of the high resolution image of Sb₂O₅.

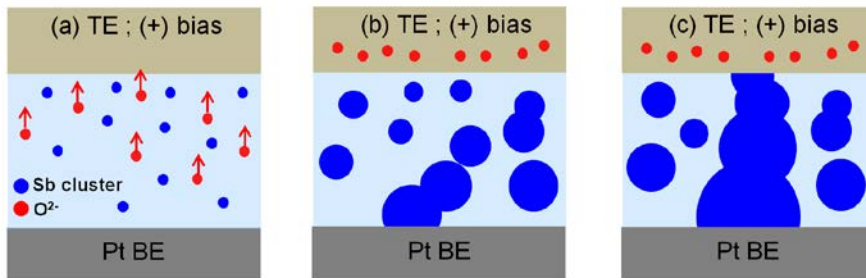


Figure 4.1.12 The schematic diagram of conducting filament formation process in Sb_2O_5 films.

4.1.4 Summary

Two types of TE/amorphous-Sb₂O₅/Pt structure were prepared using Pt and Sb as the top electrode. From the XPS depth profiling and AES analyses, it was revealed that the metallic Sb clusters were created by diffusion of oxygen from Sb₂O₅ to the top Sb electrode (SSP sample) but were not created in the case of the top Pt electrode (PSP sample).

Both PSP and SSP samples showed URS behavior with switching current lower than those of several other TMO materials by almost two orders of magnitude, but the switching endurance of the PSP sample was insufficient to satisfy the requirement for memory application. The weak binding between the pnictogen element Sb and O and the low melting point of Sb₂O₅ resulted switching of low energy consumption, but they also made the RS relatively less reliable. When Sb was used as the top electrode, endurance characteristics improved greatly because of the suppression of oxygen loss from the Sb₂O₅ films by the oxygen blocking effect of Sb TE. In addition, severe oxygen gas evolution from the Sb₂O₅ films during electroforming can be alleviated by pre-existing Sb clusters.

Asymmetric *I-V* switching results with respect to the bias polarity were achieved from the SSP sample, because of the presence of the oxygen-rich layer in the top electrode region. The oxygen was driven into the Sb-cluster-

containing Sb_2O_5 films when the Sb TE was negatively biased, which precluded the fluent formation of a metallic Sb path that connects the TE and BE. TEM analysis confirmed that the electrical stressing induced the formation of metallic Sb clusters, which would percolate to form conducting filaments during the set switching. This pnictogen oxide material with inert electrode represents a class of RS material which can show fluent URS behavior but limited reliability. This is mainly attributed to the weak binding energy of the metal ions with oxygen.

4.2 Bipolar resistive switching characteristics in Sb_2O_5 films

4.2.1 Introduction

The resistive switching (RS) phenomenon for various metal oxides has been extensively studied because of its great potential for resistive random access memory application. [36, 37] The RS phenomenon of metal oxides can be divided into unipolar resistive switching (URS) and bipolar resistive switching (BRS). In the URS phenomenon, set (switching from high resistance state (HRS) to low resistance state (LRS)) and reset (switching from LRS to HRS) occur under the same voltage polarity through a local current path called the conducting filament (CF). [36-38] In URS, the set switching proceeds via a field-assisted thermochemical reaction, while the reset is mostly driven by thermal energy. On the other hand, the BRS phenomenon where set and reset switching depends on bias polarity is generally explained by the interfacial effect such as the modulation of Schottky barrier height (SBH) between the electrode and oxide layer. [39, 40] The URS and BRS are mostly thermal energy and electric field driven phenomena, respectively, and, thus, have been considered to have disparate origins. However, there are actually many cases where the URS and BRS mechanisms present concurrently in the same RS sample, suggesting that they

are closely correlated. [41, 42] Recently, some of the authors suggested the electronically- (charge trapping and de-trapping) or ionically-driven (oxygen vacancy model combined with the localized CF model) BRS mechanism in the CF-ruptured region of URS TiO_2 . [43, 44] However, it is not clearly understood whether the same mechanism can explain the concurrent presence of URS and BRS in other metal oxide systems.

Recently, the authors reported a low energy-consuming URS behavior for a pnictogen oxide (Sb_2O_5), which is mainly due to its low oxygen binding energy. [45] The highly unstable RS property of the Sb_2O_5 film with Pt top and bottom electrodes were largely improved by adopting the Sb top electrode. [10] It was interesting to note that the URS behavior was still observed from such an asymmetric electrode configuration (Sb/ Sb_2O_5 /Pt, called SSP), which would have shown the BRS. Therefore, it is an impending task to check if the sample can show BRS and, if that is the case, what is the potential correlation with URS.

In this chapter, experimental evidences that show the concurrent presence of URS and BRS and the local rupture and recovery of the CF near the anode interface in the SSP sample were presented. A previously suggested method for finding the local rupture and recovery region of CF was adopted. [46] The occurrence of URS or BRS was determined by the degree of rupture regarding CF, and the detailed RS mechanisms for URS and BRS were suggested by studying the electrical conduction mechanisms in the HRS in both RS modes.

4.2.2 Experimental procedure

Sb_2O_5 films, which are n-type semiconductors with a band gap of ~ 3 eV, [32] were deposited using reactive dc magnetron sputtering on Pt/Ti/ SiO_2 /Si substrates. During deposition, the dc power of the Sb target was fixed at 40W, and oxygen concentration in Ar and O_2 gas mixture was 23 %. The chamber pressure and substrate temperature were 6 mTorr and room temperature, respectively. The chemical state of the deposited films was confirmed as stoichiometric Sb_2O_5 by X-ray photoelectron spectroscopy (XPS, SIGMAPROBE).

As mentioned in chapter 4.1, the film thickness of Sb_2O_5 was set to be ~ 30 nm, which was confirmed by cross-sectional transmission electron microscopy (TEM), and the amorphous nature of the deposited Sb_2O_5 films was revealed by X-ray diffraction. After depositing the Sb_2O_5 films, a 100nm-thick Sb top electrode (TE, 300 μm in diameter by shadow mask) was formed by dc magnetron sputtering. The RS characteristics of the SSP structure were measured using an HP4145A semiconductor parameter analyzer at room temperature. During electroforming and set switching, current compliance (I_{cc}) was set to 1 mA, to prevent the complete breakdown of the devices. TE was biased positively or negatively while the Pt bottom electrode (BE) was grounded. The typical electroforming voltage (V_f) from LRS to HRS in URS

was approximately 6.2 - 6.5 V. The Schottky barrier height (SBH) at the Sb/Sb₂O₅ interface was calculated by measuring the current-voltage (*I-V*) with the negative bias being applied to the Sb TE at temperatures ranging from 25 to 105 °C.

4.2.3 Results and Discussions.

4.2.3-1 Anode interfaced switching of Sb_2O_5 films

In the previous chapter, it was found that the CF in the SSP sample is composed of metallic Sb clusters, which percolates between the TE and BE from the detailed TEM study. [45] However, it was not confirmed whether the rupture and recovery of the CF during the repeated switching are localized at a certain location along the length direction of the CF. Kim et al. reported that the RS experiment with the serially connected RS cells is a feasible method to check where the actual RS occurs along the direction of film thickness (along the length direction of CF). [46] Since the rupture and subsequent recovery of the CF will most probably occur locally in most RS oxide materials, the same configuration of the RS experiment was set up in this work as shown in the inset of Fig. 4.2.1. Figure 4.2.2 shows the I - V curves of electroforming (curve F) and the subsequent reset process (curve R) of serially connected A-B or C-D pads. Here, pads A and B (or C and D) were selected and a positive bias was applied to pad A (or C) during the electroforming and reset processes, while pad B (or D) was grounded. Therefore, CF should be formed in the Sb_2O_5 film of the $\text{Sb}/\text{Sb}_2\text{O}_5/\text{Pt}/\text{Sb}_2\text{O}_5/\text{Sb}$ structure after electroforming. The value of V_f was roughly 11 V, which is about 1.7~1.8-times higher than that

of the single SSP sample. Next, the subsequent I - V sweeps of serially connected A and C electrodes (curve A-C), which were anodes during electroforming and subsequent reset processes, and B and D (curve B-D), which were grounded, are shown in Fig. 4.2.2. The I - V of pads B-D demonstrate LRS behavior meaning that CFs in Sb_2O_5 films under pads B and D remain intact. However, HRS behavior is observed from the I - V of pads A-C. The measured resistance value at 0.1 V between pads B (D) and Pt BE, and A (C) and Pt BE was low ($\sim 450 \Omega$) and high ($\sim 2.5 \text{ M}\Omega$), respectively, which corroborate the I - V curves of B-D and A-C in Fig. 4.2.2. These results suggest that the CFs beneath the anode pads (A and C) were ruptured while those under the cathode pads were retained during the reset process. The same experiment was repeated more than 20 times and almost all the results showed that the localized rupture and recovery of the CF occurred near the anode interface. Thus, it can be concluded that the rupture and recovery of the CF during the RS switching of the SSP structure only occur near the anode, which is identical to that in TiO_2 film. [46]

In the pristine state of the SSP structure, the oxygen reduction process occurred with increasing applied bias. In n-type materials, the CF is generally stronger and more conductive near the cathode interface compared to the anode interface because the oxygen vacancies, which comprise of CF, are moved to the cathode interface by an external electric field. [47] In addition,

the thermal conductivity of Sb thin films is under 20 W/m-k, [48] which is relatively lower than that of Pt (72 W/m-k). These thermal properties can enhance the thermal efficiency in the Sb electrode interface region during the reset process since heat loss through Sb TE will be less than Pt BE. [49] In order to understand these effects more clearly, electro-thermal simulation is performed, which shows thermal distribution of ReRAM devices (Figure 4.2.3 (a)). The physical parameters of materials, such as thermal conductivity (κ) and specific heat (C_p), etc., were taken from bulk values (Table 4.2.1). Electrical resistivity of filament was extracted from the resistance of the low resistance state (LRS) obtained from I–V curve. Figure 4.2.3 (b) shows the simulation results which indicated temperature distribution of SSP structure reach steady state after 50 ns. Injected I_{res} and LRS values were obtained from Fig. 4.2.2. In figure 4.2.3 (b), the maximum temperature in SSP structure is almost 900 °C which occurs near the Sb/Sb₂O₅ interface. This can be interpreted by the fact that lower κ of Sb could suppress larger amount of heat loss through top electrode. In addition, because filament area in cathode interface is generally larger than that of anode interface, larger current density in anode interface arise when electrical bias is applied. Therefore, more heat should be generated near the Sb anode interface by electrical current and rupture will occur in a relatively weaker CF in the anode interface region, while the CF in the cathode interface region remains unaffected during the

reset process. Figure 4.2.4 shows the schematic diagram for the developed CFs in the serially connected sample. Based on these explanations regarding the URS property of the SSP sample, the following BRS behaviors of the same sample are examined.

1. Forming and Reset

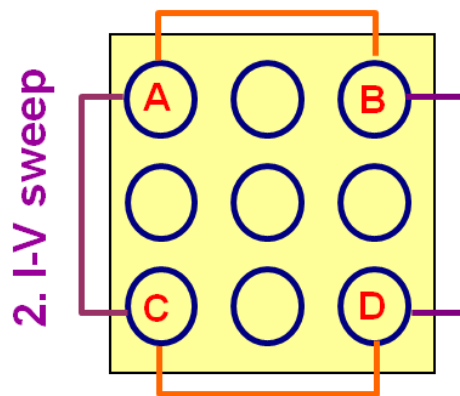


Figure 4.2.1 The schematic diagram of I - V sweep method for anode-cathode interface switching experiment.

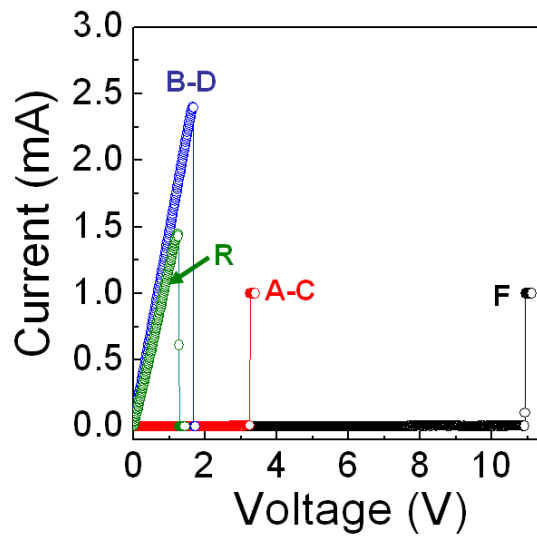


Figure 4.2.2 (a) *I-V* curves of the electroforming process (curve F), and subsequent reset process (curve R). *I-V* curves between pads A and C (curve A-C), and pads B and D (curve B-D) after the reset process is also shown in 4.1.2

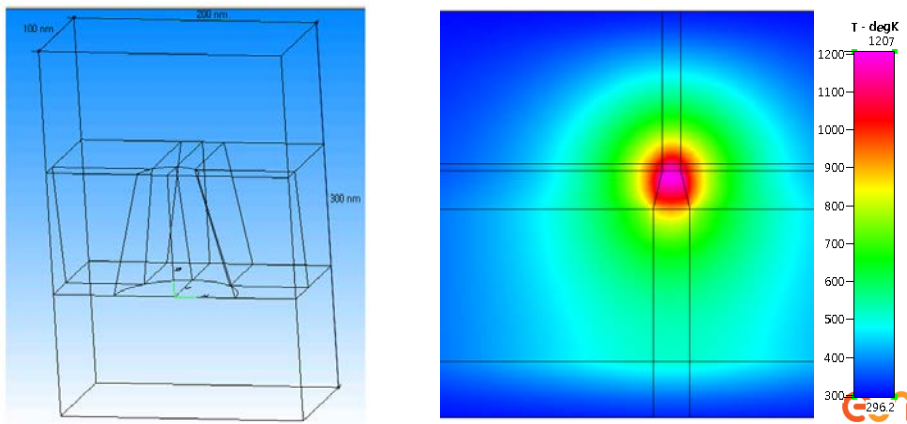


Figure 4.2.3 (a) Simulation structure of SSP device, (b) temperature distribution in SSP device.

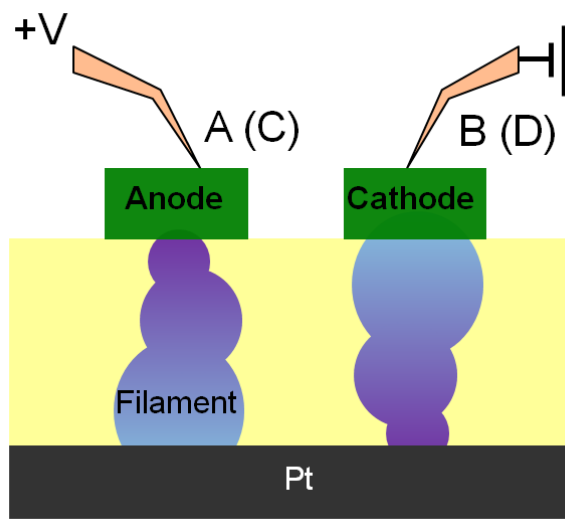


Figure 4.2.4 Schematic diagram of Sb/Sb₂O₅/Pt structure after the developed CFs.

Table 4.2.1 Physical constant used in electro-thermal simulation [48, 51, 52]

Materials	C_p ($J \cdot mol^{-1} K^{-1}$)	κ ($W \cdot m^{-1} K^{-1}$)	Resistivity ($\mu\Omega \cdot cm$)
Pt	25.86	72	0.01
Sb_2O_5	25	10	10^8
Sb	25.23	20	1

4.2.3-2 Bipolar resistive switching properties of Sb_2O_5 films

Figure 4.2.5 shows the I - V characteristics of 70 URS cycles for the single SSP sample with the I_{cc} of 1mA. As mentioned in chapter 4.1.1, it was observed that the Sb TE already contains rather high density of oxygen atoms which were driven into the Sb_2O_5 films from Sb top electrode (TE) when negative bias was applied to TE during electroforming process in pristine single SSP sample. This precluded the formation of a metallic Sb path that connects the TE and bottom electrode. Therefore, all the experimental results of single SSP device were examined only under positive bias polarity because the electrical analysis results of this sample were observed more clearly under the positive bias than those under the negative bias. The repeated URS experiments showed a reset voltage (V_{res}) of 1 - 1.3 V, a reset current (I_{res}) as low as 1.3 - 1.8 mA, and a set voltage (V_{set}) of 1.7 - 2 V. The resistance ratio of HRS to LRS read at 0.1 V is about two orders of magnitude. In TiO_2 , a typical material that shows the concurrent presence of URS and BRS, the switching between the two RS modes was accomplished by taking different I_{cc} during the set operation. [42] However, only the URS phenomenon of the SSP sample was observed irrespective of the I_{cc} even though it varied in a wide range of 0.1 - 5 mA. On the other hand, there are certain abnormal reset processes during repeated URS cycles as shown by the red curve in Fig. 4.2.5, which is enlarged in Fig. 4.2.6. During the 200 URS cycle test, such abnormal

unipolar reset curves were observed only 3-times. When such an abnormal reset I - V sweep was observed, the subsequent RS can be controlled into either URS or BRS as shown below. The occurrence of such an abnormal reset was random, which must be related with the formation of a weaker CF during the previous set step, however, at the moment it is not clearly understood what causes such an abnormal process although this must be related with the statistical problem.

When the electrical bias was maintained until the low current level (blue circle region in Fig. 4.2.6) was reached, the subsequent I - V sweep after this abnormal reset process showed the URS behavior. However, when the applied bias was discontinued in the middle current level (red circle region in Fig. 4.2.6), the subsequent RS characteristics of the single SSP sample became BRS as shown in Fig. 4.2.7. It can be understood that the migration of oxygen ions from and into the partly ruptured CF region near the anode is responsible for the BRS from the negative and positive bias polarities of the BRS set and reset steps shown in Fig. 4.2.8. Here, the voltage sweep range for set and reset processes was from 0 to -0.6 and 0.6 V, respectively. The BRS V_{set} was approximately -0.5 V and the negative differential resistance (NDR) occurred at ~0.3 V with a peak current of ~0.6 mA. Thus, the power consumption for set and reset switching in BRS is less than that of URS. Figure 4.2.8 illustrates the distribution of the resistance values in the HRS and LRS for the device measured at 0.1 V. This device operated between the HRS and LRS for 50

switching cycles without switching failure, and the average resistance ratio read at 0.1 V between HRS and LRS was roughly 6.

Yoon et al. recently reported that the BRS behavior in the Pt/TiO₂/Pt device can be altered to tri-stable states by controlling the extent of rupture regarding the filament when the BRS behavior was initiated from the reset state of URS. [43] The origin of BRS in the SSP sample is expected to be similar to that of the TiO₂ sample. When the electrical bias is applied during the abnormal URS reset process, the rupture of CF should be initiated at the anode interface region with limited extent. Since the applied voltage is discontinued in the middle of filament rupture process, the weak remaining CF near the anode interface, while the other part of the CF remains intact, may induce the BRS. This is confirmed by the detailed analysis on the conduction mechanism of URS and BRS discussed below.

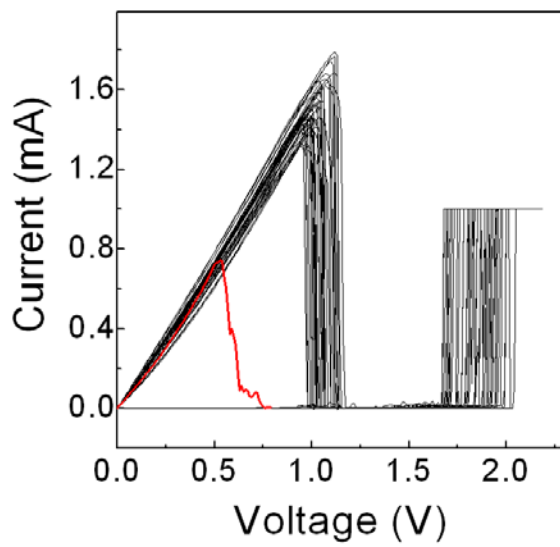


Figure 4.2.5 The URS I - V characteristics of the Sb/Sb₂O₅/Pt structure.

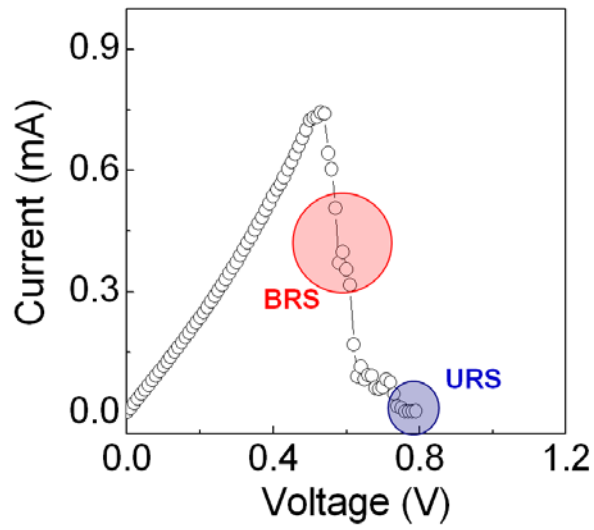


Figure 4.2.6 *I-V* result of abnormal reset process during URS cycling measurement.

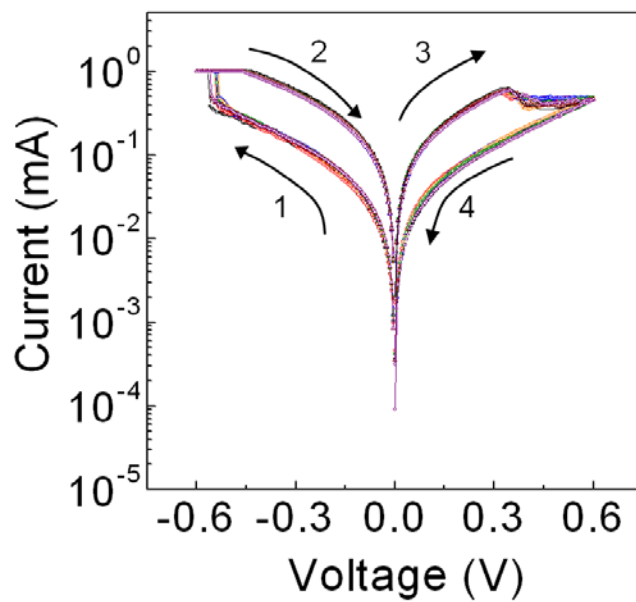


Figure 4.2.7 The BRS I - V characteristics after abnormal URS reset process.

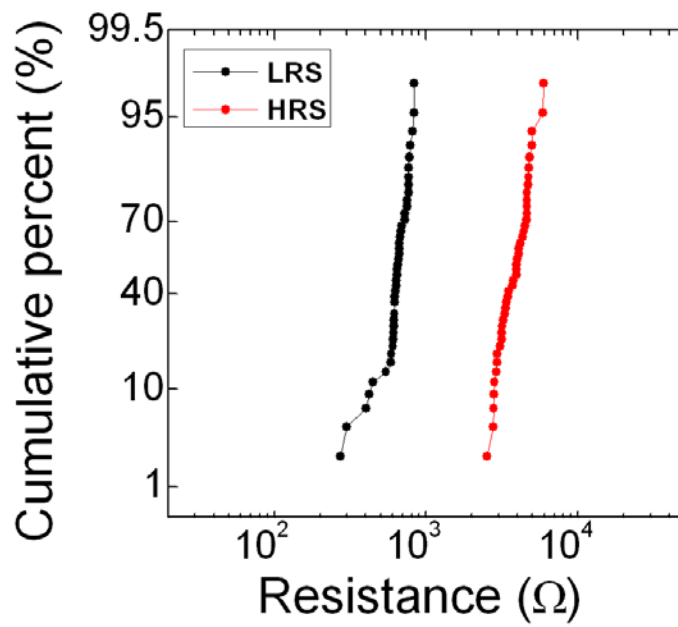


Figure 4.2.8 The distribution of the low and high resistance values.

The nonlinear electronic conduction mechanisms including Schottky emission, space-charge-limited current (SCLC), and Poole-Frenkel (P-F) emission were adopted to fit the measured I - V relation. Figure 4.2.9 shows the I - V curves of HRS in URS measured at temperatures ranging from 25 to 105 °C and the lower left inset shows the fitting results to Schottky emission. From the slope of each linear fit in lower left inset, the SBH as a function of applied voltage was obtained (lower right inset). The zero-voltage SBH at the Sb/Sb₂O₅ interface was estimated to be 0.66 eV from the extrapolation of the best linear fitted graph to $V = 0$. The estimated optical dielectric constant of k was ~ 2 from the fitting, which is consistent with the estimated refractive index ($n \sim k^{1/2}$) of 1.55 probed from the ellipsometry of Sb₂O₅ films. The dominant Schottky emission conduction with relatively high SBH in the HRS of URS indicates that the rupture of the CF near the Sb TE was quite extensive, meaning that the defect density in the CF-ruptured region is quite low. This is due to the easy oxidation of CF during the reset process because of the low melting point (high ion mobility) of metallic Sb (904 K), and Sb₂O₅ (798 K). [12] In contrast, the conduction mechanism in the HRS of BRS was best-fitted to the SCLC mechanism as shown in Fig. 4.2.10. The inset of Fig. 4.2.11 shows ten BRS I - V curves plotted according to the SCLC mechanism, showing the uniformity of the I - V curves. The conduction in the LRS can be well explained by the Ohmic conduction. In the low voltage region of the HRS, the current shows a linear relation with voltage (Ohm's law) and the

slope increases to 1.87 at a higher voltage, which follows the relation of $I-V^2$ (Child's law). Then, the current sharply rises with a slope of 4.12, which is close to 4.0, at the trap-filled-limited voltage (V_{TFL}). The increase of the current beyond V_{TFL} can be understood whereby the shallow trapping sites, *i.e.* oxygen vacancies, between Sb TE and the remaining CF region are fully occupied. Hence, the conduction behavior of BRS in the SSP sample is explained by the trap-controlled SCLC mechanism. [46] The Schottky and P-F emissions were also applied, but they did not fit the curves well. The fact that HRS follows the SCLC mechanism suggests that the electrical conduction is not governed by SBH. Kim et al. explained BRS of TiO_2 as bias-polarity-dependent carrier trapping and de-trapping processes, assuming that interfacial SBH is less than 0.1 eV. [44] They claimed that such a low SBH enables fluent carrier injection into the conduction band of the insulator and the high-density traps within the localized region, where the CF is ruptured, cause the SCLC. In the case of BRS for the SSP structure, high oxygen vacancies may exist in the CF ruptured region and the SBH should be low since the rupture of CF through the oxidation of metallic Sb is not fully completed. Injected electrons will be trapped by oxygen vacancies in the CF ruptured region.

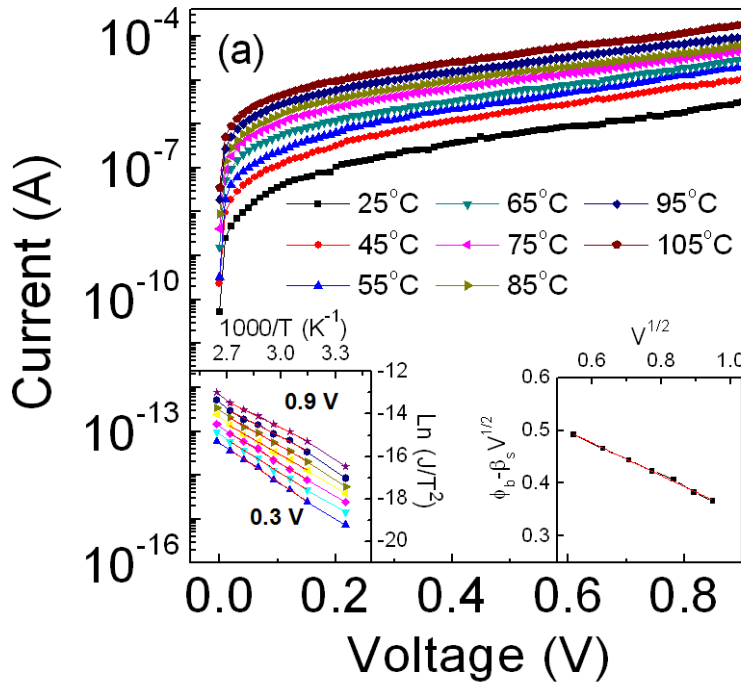


Figure 4.2.9 The I - V curves of the Sb/Sb₂O₃/Pt device measured at temperatures ranging from 25 to 105 °C. The Schottky plot of the J - T curves is shown in lower-left inset figure. The lower-right inset figure shows the variation in SBH as a function of V .

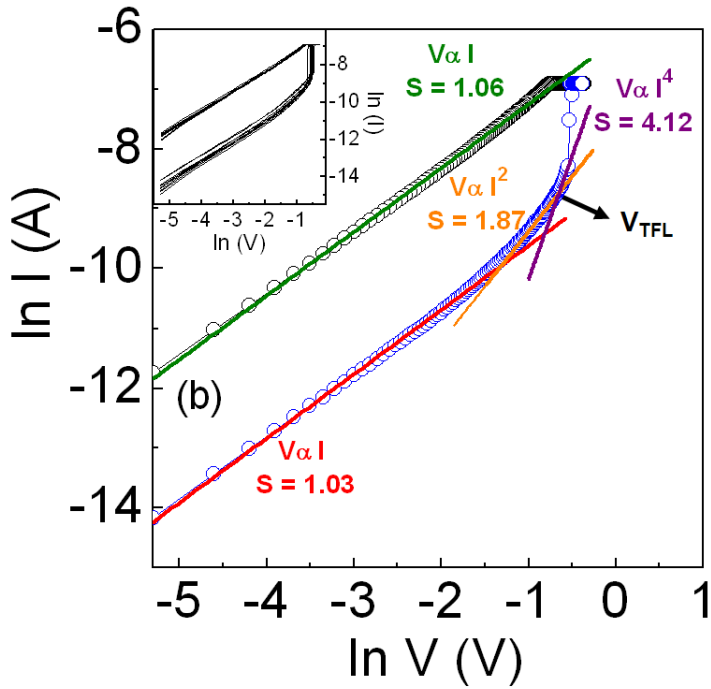


Figure 4.2.10 The I-V curves and fitting results using SCLC mechanism of the LRS and HRS plotted on a log-log scale. The upper-left inset shows 10 cycles of BRS.

As the transition from the URS mode to the BRS mode was occasional, the reverse transition from the BRS mode to the URS mode also occurred occasionally. *I-V* curves of Fig. 4.2.11 show the transition from BRS to URS. During the repeated *I-V* sweeping in the BRS mode, the current suddenly dropped to a low level without showing NDR, which is similar to the reset process of URS as indicated by the red curve. After this abnormal reset, set switching became possible with either the positive or negative bias, and a typical set switching *I-V* curve with negative bias was included, which is indicated by the black arrow. In this case, the current level in the reset state and V_{set} were quite smaller and larger than that of the BRS case, respectively, suggesting that the CF rupture during the previous abnormal reset was extensive as in URS. In addition, the RS sample, which changed from BRS to URS, tends to show only URS behavior, and it can be inferred that the BRS behavior of SSP sample was less reproducible and less controllable than that of URS. This is because when BRS sample experiences switching failure and turns into unipolar reset state, steep current drop during BRS cycles occurred suddenly without tri-metastable state which can be seen in the current levels of abnormal URS reset process (blue and red circle regions in Fig. 4.2.5). This also implies that the BRS behavior is close to the ionic switching mechanism schematically shown in Fig. 4.2.12, rather than the electronic switching one.

In Fig. 4.2.12 (a), the status of the CF ruptured region near the anode, where the mixture of oxygen vacancies and oxygen ions are present with the

remaining part of CF, is schematically shown. When the negative voltage is applied to the TE, the oxygen vacancies are gradually attracted into the CF ruptured region by the external electric field while the oxygen ions are repelled to the bulk of the Sb_2O_5 film or onto the interface with Pt BE (Fig. 4.2.12 (b)). If this vacancy gathering becomes too severe, the ruptured CF is completely recovered and URS is also recovered accordingly. The reset process occurs when positive bias is applied to the TE (Fig. 4.2.12 (c)). The NDR behavior is believed to show up due to gradual oxidation in the locally rejuvenated region of the CF. Again, if this recovery is too high, then the SSP sample begins to show the URS reset state and URS is recovered.

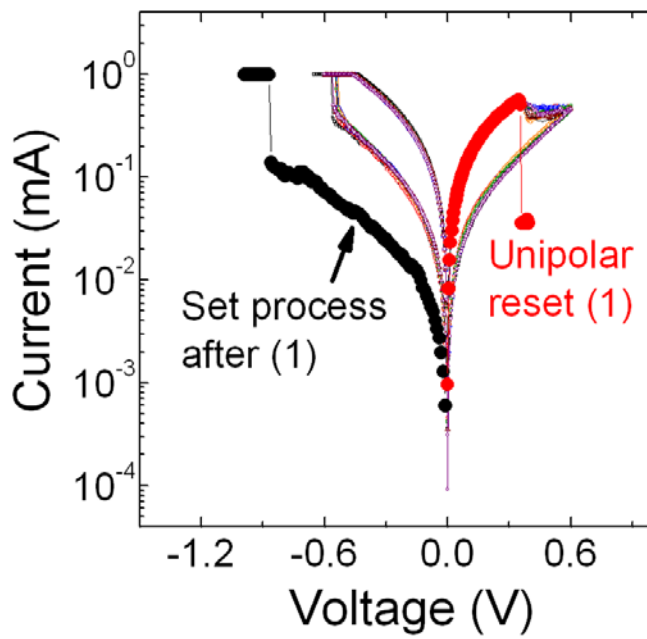


Figure 4.2.11 The abnormal reset process during BRS cycling measurement.

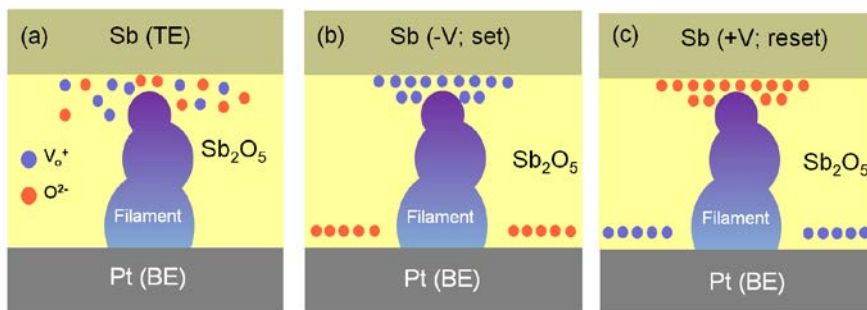


Figure 4.2.12 The schematic diagrams of (a) reset state after abnormal reset process of URS, (b) set process of BRS, and (c) reset process of BRS.

4.2.4 Summary

In this chapter, the concurrent presence of URS and BRS behaviors and the transitions between them regarding the Sb/Sb₂O₅/Pt structure were studied. The RS was induced by the rupture and recovery of the filaments in the localized region near the anode (Sb electrode). The BRS phenomenon was driven by the abnormal reset process during URS and the recovery of URS was induced by another abnormal reset process during BRS. The Schottky emission and space-charge-limited current in HRS were the dominant conduction mechanisms for URS and BRS, respectively, meaning that the URS and BRS phenomena are induced by more complete (URS) and retarded (BRS) reoxidation and reduction of the local CF-ruptured region.

4.3 The effects of bottom electrode material on resistive switching properties of Sb_2O_5 films

4.3.1 Introduction

Recently, one of the subjects facing the semiconductor industry involves the scaling limit of conventional nonvolatile memory (NVM). Among the several candidates for next-generation NVMs to solve this problem, resistive random access memory (ReRAM) based on a simple binary metal oxide has the potential to serve as a replacement for conventional NVM owing to its good retention, high endurance properties, rapid operation, and low power consumption. [53]

Many experimental results have explained the resistive switching mechanism of NiO or TiO_2 in terms of the formation and rupture of the conducting path in thin film bulk. [54] However, if the conducting path ruptures in bulk, the role of the metal electrode would simply involve the carrying of the current. It has been shown that the properties of resistive switching (RS) depend strongly upon the metal electrodes in various metal oxide ReRAMs. For example, the interfacial reaction between the metal electrode and TMO may have adverse influence on the properties of RS. [55, 56] Moreover, cation migration from metal electrodes plays a significant role

in RS through the effect of electrochemical metallization. [57] Therefore, Pt electrode is widely used for resistive switching materials because Pt, which is inert material, electrode is free about diffusion and chemical reaction issues with resistive switching materials. In addition, Pt is prone to form a Schottky contact with n-type semiconductor materials, and these well-defined Schottky contact has been shown to enhance the RS characteristics since leakage level can decrease during electroforming and set process. However, because Pt cannot be easily etched, it is hard to apply as electrodes material in mass production. Furthermore, considering the relatively high cost of the widely used Pt compare with other electrode materials, reducing the manufacturing cost is essential before ReRAM can be commercialized as a type of next-generation NVM. Therefore, the effects of electrodes on the RS properties must be considered as an important factor in pursuit of a proper metal electrode.

This chapter presents systematic investigation of the effects of Ti (reactive metal with Sb_2O_5 films and low work function as 4.4 eV [58]), TiN (non-reactive metal with Sb_2O_5 films and low work function as 4.5 eV [59]), and Pt (non-reactive metal with Sb_2O_5 films and high work function as 5.4 eV [58]) bottom metal electrodes on the resistive switching properties of Sb_2O_5 thin films. Ti metal is well known for its ability to absorb oxygen atoms from buried HfO_2 [60] and modify the resistive switching property of the ZrO_2 [61]. In contrast, TiN Titanium nitride (TiN) is used as diffusion barrier in very

large scale integration (VLSI) metallization schemes. It can prevent an undesired chemical interaction between bottom electrode and resistive switching materials.

4.3.2 Experimental procedure

100 nm-thick Ti or TiN bottom electrodes were deposited by reactive dc magnetron sputtering on SiO₂/Si substrates. A metallic Ti target (99.99 %, LTS Inc.) with 3-inch diameter was sputtered in a nitrogen (N₂) and argon (Ar) gas mixture, whose N₂ content was varied from 0 to 9 %, controlled by regulating the nitrogen flow. The chamber pressure and substrate temperature during Ti film deposition were 6 mTorr and room temperature, respectively. The substrate temperature during deposition of TiN films was varied from 350 °C to 475 °C. Then, Sb₂O₅ films were deposited using reactive dc magnetron sputtering on BE/SiO₂/Si substrates. After Sb₂O₅ film deposition, 100nm-thick Sb was formed by dc magnetron sputtering using metal shadow mask. The Sb/Sb₂O₅/Ti (SST) and Sb/Sb₂O₅/TiN (SSN) structures were used for the measurement of electrical characteristics.

The crystallinity of the grown films was analyzed by glancing angle X-ray diffraction (GAXRD, PANalytical, X'Pert PRO MPD) under Cu K α radiation at 40 kV and 30 mA. The chemical composition of the TiN films was examined using the Auger electron spectroscopy (AES, Perkin-Elmer 660) depth profiles. The RS characteristics of the SST and SSN structure were measured with an HP4145A semiconductor parameter analyzer at room temperature. The resistances of HRS and LRS were measured at 0.1 V. During

RS, the top electrode was biased positively or negatively, while the bottom electrode was grounded.

4.3.3 Result and discussions

4.3.3-1 Material properties of deposited TiN films

Figure 4.3.1 shows the dependence of the deposition rate of TiN on the N_2 partial pressure in the sputtering gas ($Ar + N_2$) at sputtering pressures of 6 mTorr with various substrate temperatures. The deposition time of TiN is fixed as 270 seconds. The deposition rate of TiN is not changed significantly by N_2 partial pressure and temperature changing. Figure 4.3.2 (a) shows the X-ray diffraction patterns of the deposited TiN films as a function of substrate temperature at N_2 partial pressure of 0.74. Although all deposited TiN thin films a dominant (111) texture could be found, the (111) texture of TiN is more enhanced with increasing substrate temperature. Combadiere et Al. reported that at relatively low substrate temperatures will be the dense planes containing only Ti atoms, because of two reasons - first, the character of TiN as ion-covalent solid which forms firstly the most compact piling of the most voluminous species in a FCC crystallographic lattice and second, the relatively low adatom mobility at which only a small amount of the octahedral sites are occupied by nitrogen atoms. [62, 63] So, (111) texture of TiN increased with increasing substrate temperature. Figure 4.3.2 (b) shows the X-ray diffraction patterns of TiN films with various N_2 partial pressures at 450

°C substrate temperature. The (111) texture of TiN was well defined above 0.074 % N₂ content.

Figures 4.3.3 show the AES depth profiles of TiN films grown on the SiO₂ substrate with the substrate temperature of 450 °C. TiN films have the oxygen concentration throughout the film. It would be close to highly oxygen deficient TiO_xN_y layer (x is ~ 0.3 and y ~ 0.7 for the Ti layer) rather than pure TiN films. As mentioned in Chap. 4-1, the oxygen incorporated in the film during sputtering originated from residual oxygen in the sputtering chamber. Despite the considerable oxygen concentration in the Sb films, the electrical resistivity of these oxygen-containing TiN films (100 nm), in the case where the N₂ content and substrate temperature were 7.4 % and 450 °C, respectively, on the SiO₂ (100 nm)/Si substrate was quite low as 965 μΩ-cm, enough for the TiN films to work as the bottom electrode in the SSN structure (Fig. 4.3.4).

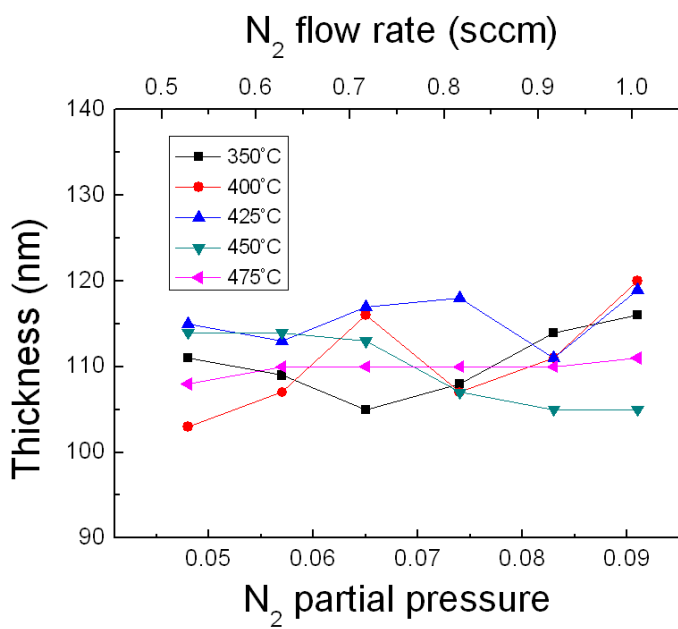


Figure 4.3.1 The dependence of the deposition rate of TiN on the N₂ partial pressure with various temperature.

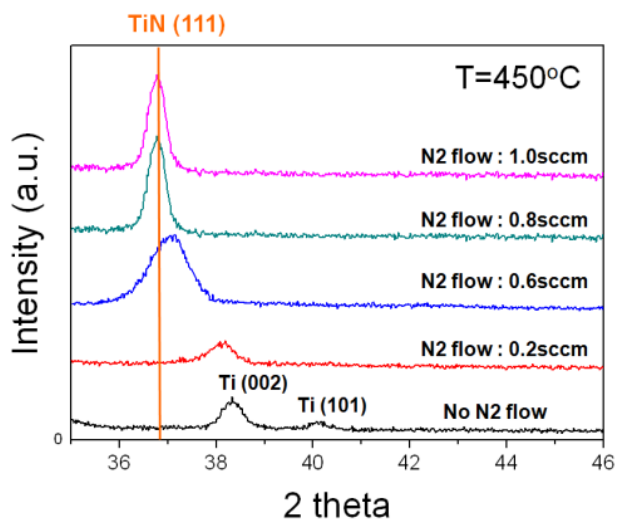
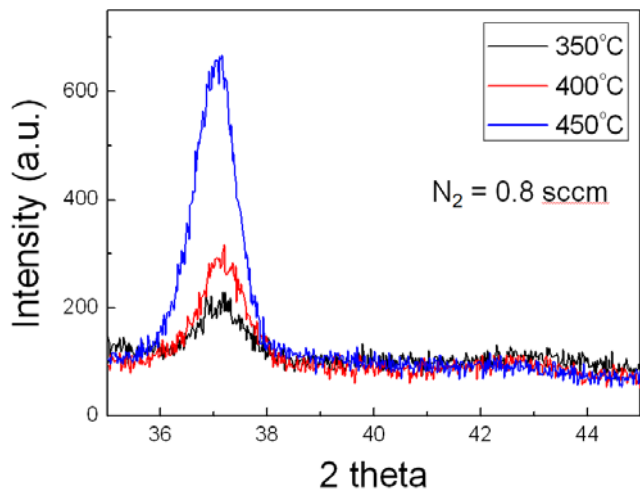


Figure 4.3.2 Glancing angle X-ray diffraction patterns of TiN films on SiO_2/Si substrate with various (a) temperature and (b) N_2 partial pressure.

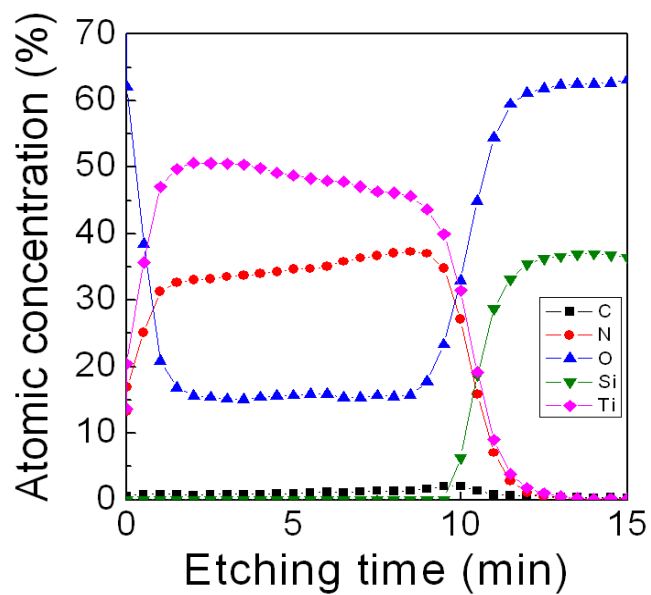


Figure 4.3.3 AES depth profiles results of TiN/SiO₂ structure.

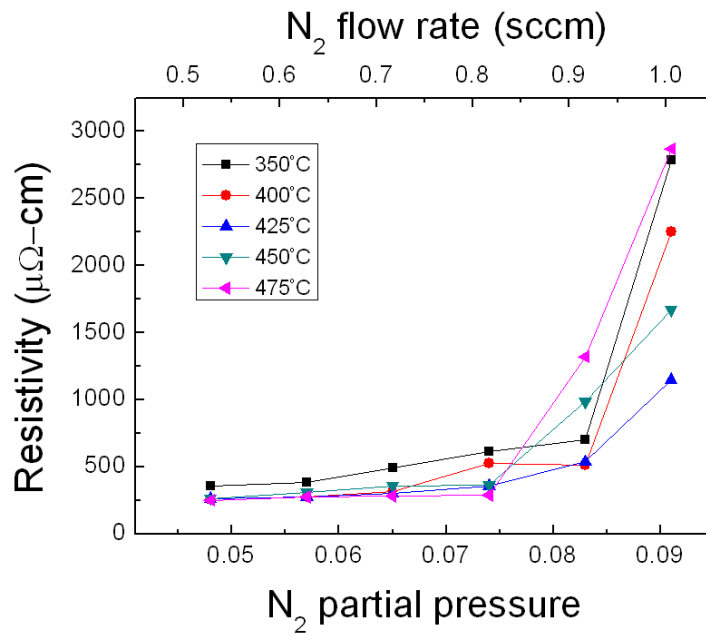


Figure 4.3.4 Changes of resistivity values of TiN films as a function of N_2 partial pressure.

4.3.3-2 Resistive switching properties of Sb/Sb₂O₅/Ti (SST) and Sb/Sb₂O₅/TiN (SSN) structure

Figure 4.3.5 shows the electroforming curves of Sb/Sb₂O₅/metal with Pt, Ti, and TiN bottom electrodes. Positive bias voltage was applied to the Sb top electrode while the bottom electrode was grounded. The current compliance (I_{cc}) for the electroforming was 1 mA. In the case of SSP and SSN structure, as-deposited samples showed electroforming process normally, although the leakage current levels in low voltage region was different. This phenomenon can be explained in terms of the work function of TiN (4.5 eV) is lower than that of Pt (5.4 eV). However, various electroforming curves are obtained when positive bias is applied to SST structure (Fig. 4.3.6). There were initially on-state curves, normal electroforming curves, and reset curve from initially on-state as shown by (1), (2), and (3) in Fig. 4.3.6, respectively. From these various electroforming process phenomena of SST structure, it can be inferred that the chemical reaction between the Ti bottom metal electrode and Sb₂O₅ plays an important role in electroforming. Generally, the oxidation of Ti occurs more easily than that of Sb in a comparison of the standard free energy of the formation of oxides shown in the Ellingham diagram in Fig. 4.1.1. Therefore, in pristine stage, oxygen getter effects of Ti bottom electrode induced a local reduction of Sb₂O₅ into Sb clusters by the diffusion of oxygen; as a result, the conducting path in Sb₂O₅ matrix could be developed. Therefore,

because of these redox reactions between Sb_2O_5 and Ti bottom electrode, various initial states form in Sb_2O_5 matrix. In pristine state, if CF was developed entire on vertical direction in Sb_2O_5 matrix by severe redox reaction, initially on-state curves during electroforming process can be obtained as shown by curve (1) in Fig. 4.3.6. The normal electroforming curves (curve (2) in Fig. 4.3.6) mean that the created Sb clusters by redox reaction exist as disconnected state each other in Sb_2O_5 matrix, and the reset curves (curve (3) in Fig. 4.3.6) can be shown by rupture of CF, which is already existed in pristine state, during electroforming process.

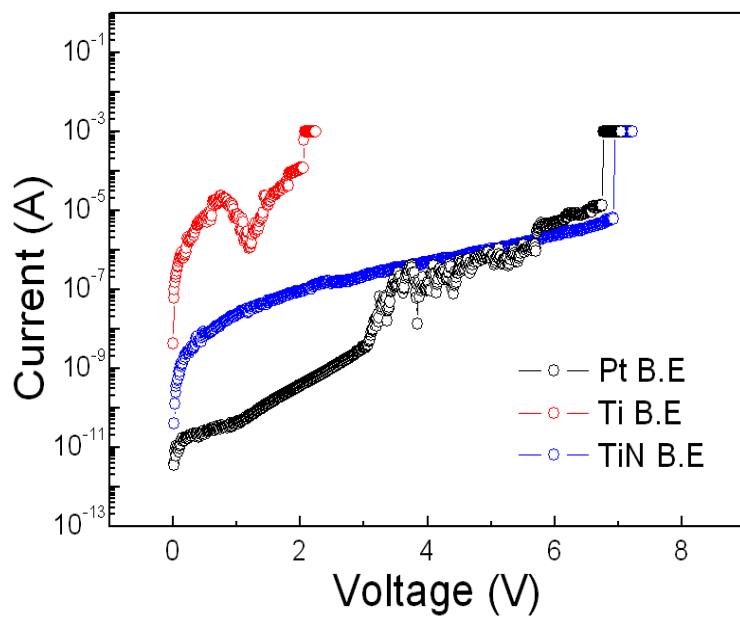


Figure 4.3.5 Electroforming curves of SSP, SST, and SSN devices.

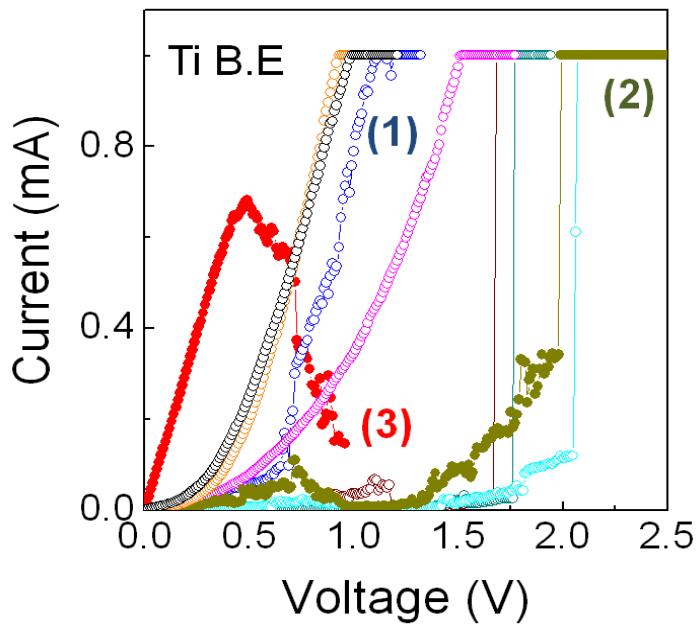


Figure 4.3.6 Various electroforming curves of Sb/Sb₂O₅/Ti device.

The RS characteristics after electroforming process were also shown variable with various electroforming curves. In the case of curves (1) in figure 4.3.6, only Ohmic conduction is shown until I_{cc} of 1 mA without electroforming process. However, in the case of curve (2), the URS phenomenon of SST device was shown after electroforming process (Fig. 4.3.7). URS endurance characteristics of SST structure were very limited. Set stuck phenomenon was always observed after ~ 3 cycles and the device could no longer reset. These early failure of SST device might come from overfull Sb clusters which is induced by oxygen diffusion effect between Sb_2O_5 and Ti bottom electrode. Figure 4.3.8 shows the BRS properties of SST structure. The BRS phenomenon was driven from reset process during electroforming process ((3) curve in Fig. 4.3.6). After this reset process, the LRS changes to the HRS by a voltage sweep with the opposite polarity as forming (set process). The HRS that appeared can be changed again to an LRS by applying a voltage with the opposite polarity as set process (reset process). The V_{set} is approximately -0.5 V and the negative differential resistance (NDR) occurred at ~ 1.0 V with a peak current of ~ 0.8 mA. Generally, in ReRAM device, electroforming process is required to activate the pristine devices to show bi-stable resistive switching. This process is regarded as a kind of soft breakdown, which generates conducting paths in the oxide film. Therefore, these BRS characteristics of SST structure without electroforming process are interesting phenomenon. As mentioned above, amount of Sb cluster, which is

the element of CF, naturally exist in Sb_2O_5 thin films due to oxygen diffusion effect. Therefore, because of already existed CF in Sb_2O_5 matrix, the pristine state of SST structure can be LRS. At these pristine stages, the reset process occurred when positive bias was applied to the TE by rupture of local Sb CFs. After this reset process, the resistance state of SST device is changed from LRS to HRS. The electronic conduction mechanism in HRS of SST structure, which showed the BRS behavior, was well defined as SCLC (Fig. 4.3.9). This result indicates that a very high concentration of oxygen vacancies may be present in erased CF region, and these oxygen vacancies can act as a shallow donor in Sb_2O_5 films, as a result, the SCLC in HRS were dominant electrical conduction mechanisms. In figure 4.3.10 (a), the reset state after applying positive bias to pristine SST sample is represented to correspond to a state where the remaining CF and the top electrode are detached with a highly oxygen vacancies and oxygen ions concentrations. Here, when the negative voltage was applied to the TE, the oxygen vacancies were influenced by the external electric field and began to move toward TE and recovery of CF can occur gradually. At specific voltage, which called V_{set} , the recovery of CF is completed and abrupt current jump to I_{cc} is happened (Fig. 4.3.10 (b)). The reset process occurred when positive bias was applied to the TE. The NDR behavior during bipolar reset switching may have occurred due to the gradual oxidation of the recovery region of local filaments when the oxygen ions migrated toward the top interface causing shrinkage of the recover region

during set process (Fig 4.3.10 (c)). Therefore, it can be concluded that the BRS phenomenon of SST devices is contributed to the electric field driven movement of oxygen vacancies and oxygen ions similar with BRS phenomenon of SSP structure (Chap. 4.2).

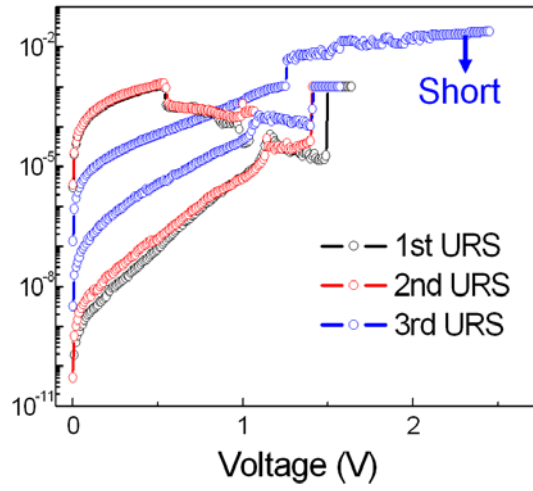


Figure 4.3.7 The URS characteristics of SST structure.

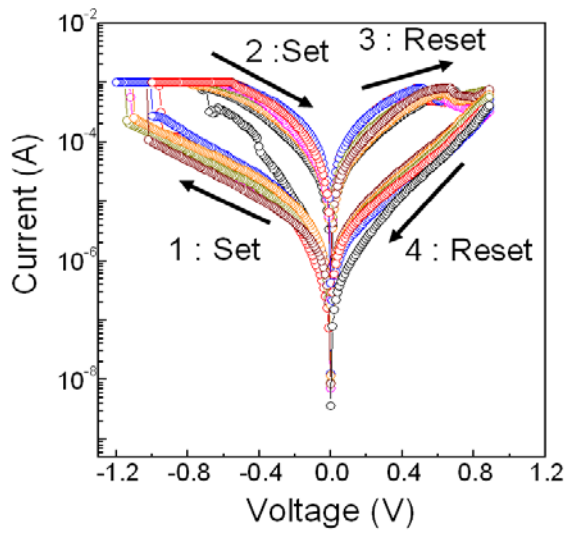


Figure 4.3.8 The BRS characteristics of SST structure.

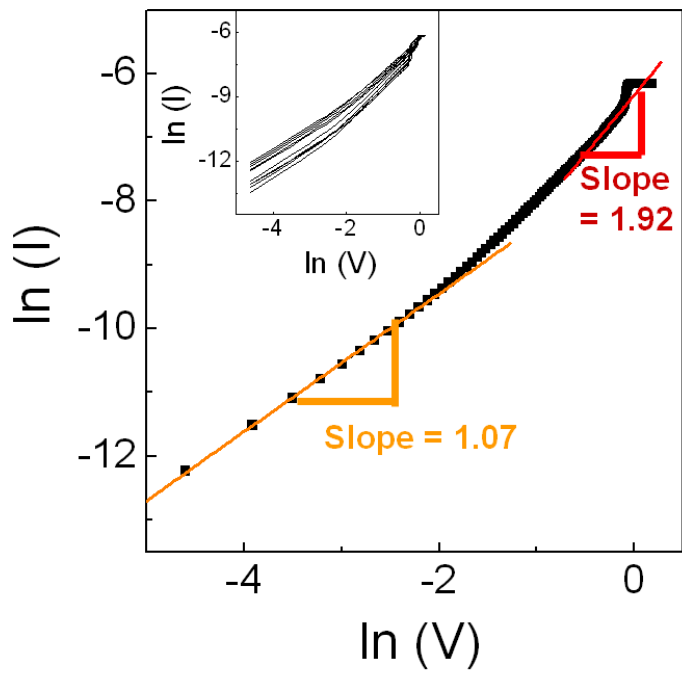


Figure 4.3.9 I - V curves and fitting results using SCLC mechanism of the HRS plotted on a log-log scale.

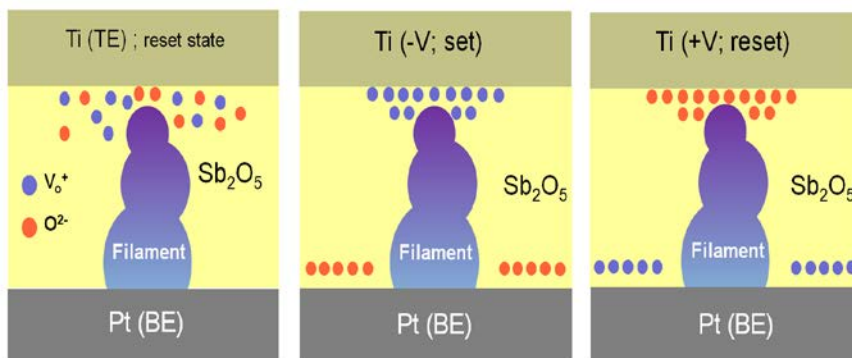


Figure 4.3.10 The schematic diagrams of (a) reset state from electroforming process, (b) set process of BRS, and (c) reset process of BRS.

The electroforming process and resistive switching behaviors of SSN structure is similar with that of SSP structure of which device characteristics were explained detail in chapter 4.1 and 4.2. I-V characteristics of URS in the SSN device by positive voltage sweep are shown in Fig. 4.3.11. The I_{cc} during forming and set operation was also 0.1 mA like SSP case in Fig 4.1.3. The V_{set} (1.6~2 V), and I_{res} (0.15~0.3 mA) are similar with the results of SSP, respectively. Figure 4.3.12 shows the endurance characteristics of SSN. The minimum ratios of HRS to LRS are maintained over 500 times of switching. This result suggests that SSN has a promising endurance property for URS application without using Pt electrode. In addition, SSN structure is also shown the BRS properties by abnormal reset process during URS cycles similar with SSP structure as mentioned in chapter 4.2.

Figure 4.3.13 shows the abnormal reset process of SSN structure during repeated URS cycles. When electrical bias was applied continually to low current level (blue spot region), the set process after this abnormal reset process went back to normal set process. However, when applied bias was stopped on the middle current level (red spot region), the RS characteristics of SSN device were changed from URS to BRS. The detailed BRS behaviors of SSN structure is shown in Fig. 4.3.14. Here, the voltage sweep range for set and reset process is from 0 V to -1.1 V and 1.1 V, respectively. The negative differential resistance (NDR) occurred at ~0.8 V with a peak current of ~0.06 mA. Thus, the power consumption for set and reset switching in BRS of SSP

device is quite less than that of URS. It is believed that these results were descended from the anode interfacial effects in SSN device. As already mentioned about BRS mechanisms of SSP structure in Chapter 4.2, it can be inferred that the origin of BRS in SSN device comes from abnormal reset process during URS cycles. Because the applied voltage was stopped during URS reset process and rupture of CF occurred firstly at anode interface region, the ruptured CF region in Sb_2O_5 films was very limited at anode interface. These interface effects lead to change the conduction mechanism between URS and BRS. Because the remained CF in the Sb_2O_5 films is very stable with a vacancy-ordered structure compared to oxygen vacancies in limited anode interface region, a recovery and rupture of CF can be happen only partially or modulate only limited anode interface region, which corresponds to a transition into the BRS. [43] The average resistance ratio between HRS and LRS was about 7~8 (inset of Fig. 4.3.14). Figure 4.3.15 shows the LRS and HRS curve. The conduction behaviors in the LRS can be well explained by the Ohmic conduction. In the low voltage region in the HRS, the current has a linear relation with voltage, I - V (Ohm's law); and at higher voltages, the slope of I - V curve was 1.95, which follows the relation $I \propto V^2$ (Child's law). The jump of the current above V_{TFL} can be understood that the shallow trapping sites, such as oxygen vacancies, between Sb TE and remained CF region are fully occupied. Therefore, the conduction behavior of BRS in the SSN device is explained by the trap-controlled SCLC mechanism similar with

SSP and SST structure. In the case of BRS of SSN structure, very high oxygen vacancies may be exist in anode interface region in HRS state and the SBH may be very low because the rupture of CF through the oxidation of metallic Sb is not perfectly completed during reset process of URS. The injected electron can be trapped by oxygen vacancies in anode interface region; as a result, the conduction mechanism is defined as SCLC.

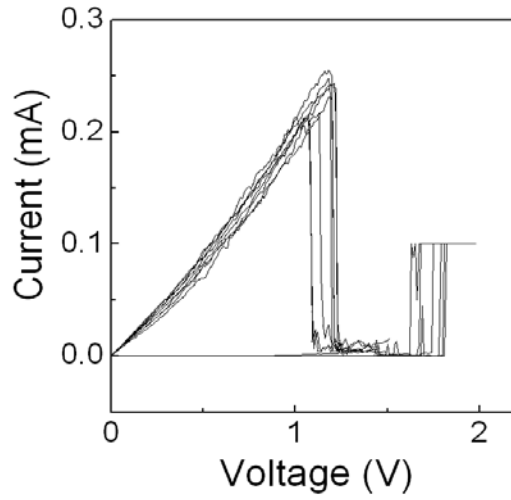


Figure 4.3.11 The URS behaviors of Sb/Sb₂O₅/TiN structure.

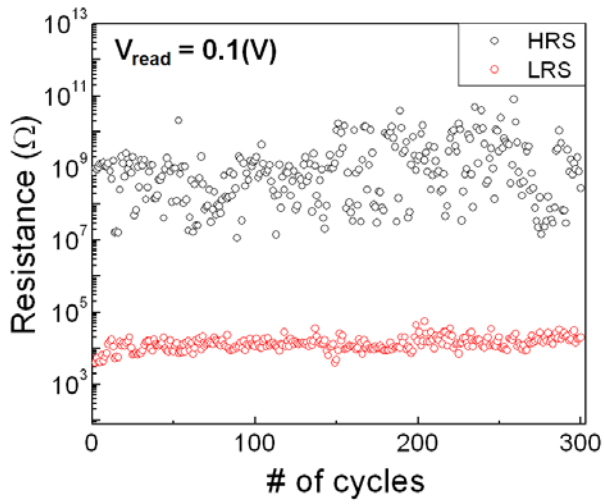


Figure 4.3.12 URS endurance characteristics of Sb/Sb₂O₅/TiN structure.

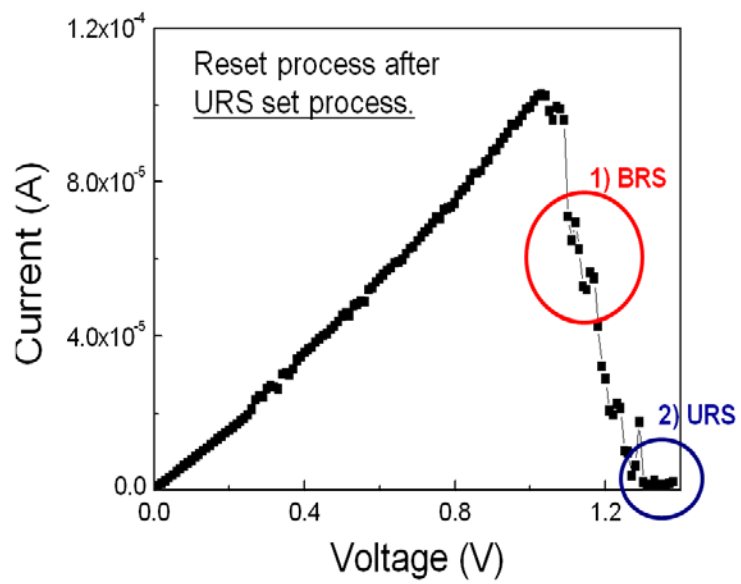


Figure 4.3.13 *I-V* result of abnormal reset process of SSN structure during URS cycling measurement.

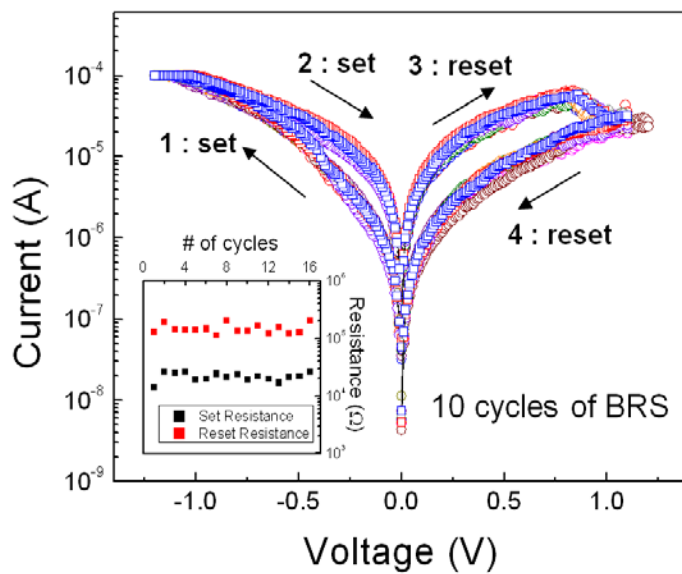


Figure 4.3.14 The BRS *I-V* characteristics after abnormal URS reset process. Inset figure shows distribution of the low and high resistance values.

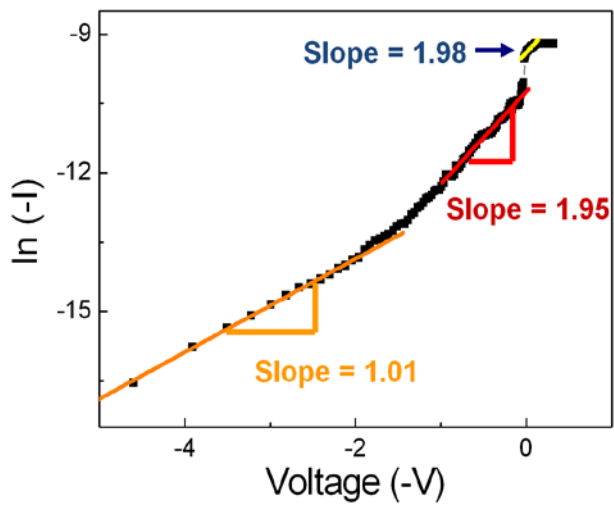


Figure 4.3.15 Fitting results of SSN device using SCLC mechanism of the HRS plotted on a log-log scale.

4.3.4 Summary

In summary, two types of Sb/Sb₂O₅/B.E structure were prepared using Ti and TiN as a bottom electrode. Because of the oxygen diffusion effect from Sb₂O₅ to Ti bottom electrode, the various electroforming and resistive switching behavior were obtained in SST structure. URS and BRS endurance properties of SST structure from *I-V* measurement were not good enough to fulfill the requirement for ReRAM application.

When TiN was used as bottom electrode instead of Ti, improvement in endurance characteristics were obtained. Both URS and BRS behavior of SSN device were similar with that of SSP device. The Space-charge-limited current in HRS was the dominant conduction mechanisms for BRS meaning that the BRS phenomena are induced by retarded reoxidation and reduction of the local conducting filament ruptured region. Because TiN film is widely used material in electronic memory industry, SSN device can be one of promising candidate for use in ReRAM.

4.4 Bibliography

- [1] J.J. Yang, I.H. Inoue, T. Mikolajick, and C.S. Hwang, *MRS Bulletin* 37 (02), 131 (2012); D.S. Jeong, R. Thomas, R.S. Katiyar, J.F. Scott, H. Kohlstedt, A. Petraru, and C.S. Hwang, *Reports on Progress in Physics* 75 (7), 076502 (2012).
- [2] W.W. Zhuang, W. Pan, B.D. Ulrich, J.J. Lee, L. Stecker, A. Burmaster, D.R. Evans, S.T. Hsu, M. Tajiri, and A. Shimaoka, *IEEE Electron Device Meeting*, 193 (2002).
- [3] R. Waser, R. Dittmann, G. Staikov, and K. Szot, *Advanced Materials* 21 (25-26), 2632 (2009).
- [4] D.S. Jeong, H. Schroeder, and R. Waser, *Electrochemical and solid-state letters* 10, G51 (2007).
- [5] K.M. Kim, G.H. Kim, S.J. Song, J.Y. Seok, M.H. Lee, J.H. Yoon, and C.S. Hwang, *Nanotechnology* 21, 305203 (2010)
- [6] K.J. Yoon, M.H. Lee, G.H. Kim, S.J. Song, J.Y. Seok, S. Han, J.H. Yoon, K.M. Kim, and C.S. Hwang, *Nanotechnology* 23 (18), 185202 (2012).
- [7] M.J. Lee, C.B. Lee, D. Lee, S.R. Lee, M. Chang, J.H. Hur, Y.B. Kim, C.J. Kim, D.H. Seo, and S. Seo, *Nature Materials* 10 (8), 625 (2011).
- [8] D.H. Kwon, K.M. Kim, J.H. Jang, J.M. Jeon, M.H. Lee, G.H. Kim, X.S. Li, G.S. Park, B. Lee, and S. Han, *Nature Nanotechnology* 5 (2), 148

(2010).

- [9] M.J. Lee, S. Han, S.H. Jeon, B.H. Park, B.S. Kang, S.E. Ahn, K.H. Kim, C.B. Lee, C.J. Kim, and I.K. Yoo, *Nano letters* 9 (4), 1476 (2009).
- [10] K.M. Kim, D.S. Jeong, and C.S. Hwang, *Nanotechnology* 22, 254002 (2011).
- [11] J.P. Strachan, M.D. Pickett, J.J. Yang, S. Aloni, AL David Kilcoyne, G. Medeiros-Ribeiro, and R. Stanley Williams, *Advanced Materials* 22 (32), 3573 (2010).
- [12] E.M. Levin, C.R. Robbins, and H.F. McMurdie, *Phase Diagram for Ceramists*, Am. Ceram. Soc., Columbus, Ohio (1969).
- [13] H. Okamoto, *Journal of Phase Equilibria and Diffusion* 29 (1), 124 (2008).
- [14] S.P. Garg, N. Krishnamurthy, A. Awasthi, and M. Venkatraman, *Journal of phase equilibria* 17 (1), 63 (1996).
- [15] K.M. Kim, B.J. Choi, B.W. Koo, S. Choi, D.S. Jeong, and C.S. Hwang, *Electrochemical and solid-state letters* 9, G343 (2006).
- [16] J. Yao, L. Zhong, D. Natelson, and J.M. Tour, *Scientific Reports* 2 (2012).
- [17] H.Y. Lee, Y.S. Chen, P.S. Chen, P.Y. Gu, Y.Y. Hsu, S.M. Wang, W.H. Liu, C.H. Tsai, S.S. Sheu, and P.C. Chiang, *IEEE Electron Device Meeting*, 19.7.1 (2010); Y.S. Chen, H.Y. Lee, P.S. Chen, PY Gu, CW Chen, WP Lin, WH Liu, YY Hsu, SS Sheu, and PC Chiang, *IEEE Electron Device*

- Meeting, 1 (2009); P. Gonon, M. Mougenot, C. Vallée, C. Jorel, V. Jousseau, H. Grampeix, and F. El Kamel, *Journal of Applied Physics* 107 (7), 074507 (2010).
- [18] C.D. Wagner, A.V. Naumkin, A. Kraut-Vass, J.W. Allison, C.J. Powell, J.R. Rumble Jr, A.Y. Lee, and D.M. Blakeslee, NIST X-ray Photoelectron Spectroscopy Database, NIST Standard Reference Database 20, Version 3.4 (Web Version) U. S. Department of Commerce (2003).
- [19] S.C. Chae, J.S. Lee, S. Kim, S.B. Lee, S.H. Chang, C. Liu, B. Kahng, H. Shin, D.W. Kim, and C.U. Jung, *Advanced Materials* 20 (6), 1154 (2008).
- [20] K. Jung, Y. Kim, W. Jung, H. Im, B. Park, J. Hong, J. Lee, J. Park, and J.K. Lee, *Applied Physics Letters* 97 (23), 233509 (2010).
- [21] X. Wu, P. Zhou, J. Li, L.Y. Chen, HB Lv, Y.Y. Lin, and T.A. Tang, *Applied Physics Letters* 90 (18), 183507 (2007).
- [22] D.C. Kim, S. Seo, S.E. Ahn, D.S. Suh, M.J. Lee, B.H. Park, I.K. Yoo, I.G. Baek, H.J. Kim, and EK Yim, *Applied Physics Letters* 88 (20), 202102 (2006).
- [23] C. Rohde, B.J. Choi, D.S. Jeong, S. Choi, J.S. Zhao, and C.S. Hwang, *Applied Physics Letters* 86, 262907 (2005).
- [24] Y.H. Do, J.S. Kwak, J.P. Hong, K. Jung, and H. Im, *Journal of Applied Physics* 104 (11), 114512 (2008).
- [25] N. Tigau, V. Ciupina, G. Prodan, GI Rusu, C. Gheorghies, and E. Vasile, *Journal of Optoelectronics and Advanced Materials* 5 (4), 907 (2003).

- [26] M. Miyayama, S. Ogi, and H. Yanagida, *Journal of the American Ceramic Society* 66 (5), 351 (1983); B. Ouni, J. Ouerfelli, A. Amlouk, K. Boubaker, and M. Amlouk, *Journal of non-crystalline solids* 356 (25), 1294 (2010).
- [27] J. H. Lee, G. H. Kim, Y. B. Ahn, J. W. Park, S. W. Ryu, C. S. Hwang, and H. J. Kim, *Applied Physics Letters* 100 (12), 123505 (2012).
- [28] J.H. Yoon, K.M. Kim, M.H. Lee, S.K. Kim, G.H. Kim, S.J. Song, J.Y. Seok, and C.S. Hwang, *Applied Physics Letters* 97 (23), 232904 (2010).
- [29] G.H. Kim, J.H. Lee, J.Y. Seok, S.J. Song, J.H. Yoon, K.J. Yoon, M.H. Lee, K.M. Kim, H.D. Lee, and S.W. Ryu, *Applied Physics Letters* 98, 262901 (2011).
- [30] J. Robertson, *The European Physical Journal Applied Physics* 28 (3), 265 (2004).
- [31] P. Puspharajah, S. Radhakrishna, and A.K. Arof, *Journal of materials science* 32 (11), 3001 (1997).
- [32] W.A. Badawy, *Thin Solid Films* 186 (1), 59 (1990).
- [33] S.H. Kim, T. Yoko, and S. Sakka, *Journal of the American Ceramic Society* 76 (10), 2486 (1993).
- [34] E.F. Lambson, G.A. Saunders, B. Bridge, and R.A. El-Mallawany, *Journal of non-crystalline solids* 69 (1), 117 (1984).
- [35] B. Ihsan, *Thermochemical data of pure substances*, Weinheim, Germany (1989).

- [36] R. Waser, R. Dittmann, G. Staikov, and K. Szot, *Advanced Materials* 21 (25-26), 2632 (2009).
- [37] D.S. Jeong, R. Thomas, RS Katiyar, JF Scott, H. Kohlstedt, A. Petraru, and C.S. Hwang, *Reports on Progress in Physics* 75 (7), 076502 (2012).
- [38] D.H. Kwon, K.M. Kim, J.H. Jang, J.M. Jeon, M.H. Lee, G.H. Kim, X.S. Li, G.S. Park, B. Lee, and S. Han, *Nature Nanotechnology* 5 (2), 148 (2010).
- [39] A. Sawa, *Materials Today* 11 (6), 28 (2008).
- [40] T. Fujii, M. Kawasaki, A. Sawa, H. Akoh, Y. Kawazoe, and Y. Tokura, *Applied Physics Letters* 86 (1), 012107 (2005); A. Baikalov, YQ Wang, B. Shen, B. Lorenz, S. Tsui, YY Sun, YY Xue, and C.W. Chu, *Applied Physics Letters* 83, 957 (2003).
- [41] C. Schindler, S. Therman, R. Waser, and Michael N. Kozicki, *IEEE Transaction on Electron Devices* 54(10), 2762 (2007)
- [42] D.S. Jeong, H. Schroeder, and R. Waser, *Electrochemical and solid-state letters* 10, G51 (2007).
- [43] K.J. Yoon, M.H. Lee, G.H. Kim, S.J. Song, J.Y. Seok, S. Han, J.H. Yoon, K.M. Kim, and C.S. Hwang, *Nanotechnology* 23 (18), 185202 (2012).
- [44] K.M. Kim, B.J. Choi, M.H. Lee, G.H. Kim, S.J. Song, J.Y. Seok, J.H. Yoon, S. Han, and C.S. Hwang, *Nanotechnology* 22, 254010 (2011).
- [45] Y. Ahn, S.W. Ryu, J.H. Lee, J.W. Park, G.H. Kim, Y.S. Kim, J. Heo, C.S.

- Hwang, and H.J. Kim. [*Accepted*, Journal of Applied Physics, Ms# JR12-7383]
- [46] K.M. Kim, B.J. Choi, and C.S. Hwang, Applied Physics Letters 90 (24), 242906 (2007).
- [47] K.M. Kim, D.S. Jeong, and C.S. Hwang, Nanotechnology 22, 254002 (2011).
- [48] F. Volklein and T. Starz, IEEE 16th International Conference on Thermoelectrics, 711 (1997)
- [49] S.W. Ryu, Y.B. Ahn, H.J. Kim, and Y. Nishi, Applied Physics Letters 100 (13), 133502 (2012).
- [50] H. Shima, F. Takano, H. Akinaga, Y. Tamai, I. H. Inoue, and H. Takagi, vol. 91, pp. 012901-1-012901-3, (2007).
- [51] W. M. Haynes, *CRC Handbook of Chemistry and Physics*, 92nd ed. CRC, Boca Raton, (2011)
- [52] N.N. Greenwood, & A. Earnshaw, *Chemistry of the Elements*, 2nd ed, Oxford: Butterworth-Heinemann (1997)
- [53] I. G. Baek, M. S. Lee, S. Seo, M. J. Lee, D. H. Seo, D. S. Suh, J. C. Park, S. O. Park, H. S. Kim, I. K. Yoo, U-In Chung, and J. T. Moon, Tech. Dig. Int. Electron Devices Meeting, 587 (2004)
- [54] W.-G. Kim, and S.-W. Rhee, Microelectron. Eng. 87, 98 (2010)
- [55] C.-Y. Lin, C.-Y. Wu, C.-Y. Wu, T.-C. Lee, F.-L. Yang, C. Hu, and T.-Y. Tseng, IEEE Electron. Device Lett. 28, 366 (2007).

- [56] C. B. Lee, B. S. Kang, A. Benayad, M. J. Lee, S.-E. Ahn, K. H. Kim, G. Stefanovich, Y. Park, and I. K. Yoo, *Appl. Phys. Lett.* 93, 042115 (2008)
- [57] R. Waser and M. Aono, *Nature Mater.* 6, 833 (2007)
- [58] H.B. Michaelson, *Journal of Applied Physics*, 48 (11), 4729 (1977)
- [59] R.C. Glass, L.M. Spellman, and R.F. Davis, *Applied physics letters*, 59 (22), 2968 (1991)
- [60] H. Kim, P. McIntyre, C. O. Chui, K. Saraswat and S. Stemmer, *J. Appl. Phys.* Vol. 96, p.3467 (2004)
- [61] C.-Y. Lin, C.-Y. Wu, C.-Y. Wu, T.-C. Lee, F.-L. Yang, C. Hu and T.-Y. Tseng, *IEEE Electron Dev. Lett.* Vol. 28, p.366 (2007)
- [62] L. Combadiere, J. Machet, *Surface Coatings Technol.* 88, 17 (1996)
- [63] S. Groudeva-Zotova, R. Kaltofen, and T. Sebald, *Surface and Coatings Technology* 127, 144 (2000)

5. Conclusion

The resistive switching characteristics of antimony oxide (Sb_2O_5) thin film, which has low binding energy, low energy band gap, and low melting point, was studied for resistive random access memory application.

Firstly, the unipolar switching properties (URS) of Sb_2O_5 thin film were investigated. $\text{Sb}/\text{Sb}_2\text{O}_5/\text{Pt}$ (SSP) and $\text{Pt}/\text{Sb}_2\text{O}_5/\text{Pt}$ (SSP) structure were prepared in this study. From the XPS depth profiling and AES analyses, it was revealed that the metallic Sb clusters were created by diffusion of oxygen from Sb_2O_5 to the top Sb electrode but were not created in the case of the top Pt electrode. When Sb was used as the top electrode, endurance characteristics improved greatly because of the suppression of oxygen loss from the Sb_2O_5 films by the oxygen blocking effect of Sb TE. In addition, severe oxygen gas evolution from the Sb_2O_5 films during electroforming can be alleviated by pre-existing Sb clusters. TEM analysis confirmed that the electrical stressing induced the formation of metallic Sb clusters, which would percolate to form conducting filaments during the set switching.

Secondly, the bipolar switching properties (BRS) of Sb_2O_5 thin film were studied using $\text{Sb}/\text{amorphous-}\text{Sb}_2\text{O}_5/\text{Pt}$ sample. The resistive switching was induced by the rupture and recovery of the filaments in the localized region near the anode. BRS phenomenon was driven by abnormal reset process

during URS. The BRS set voltage was approximately -0.5 V and the negative differential resistance (NDR) occurred at ~ 0.3 V with a peak current of ~ 0.6 mA. Thus, the power consumption for set and reset switching in BRS is less than that of URS. The Schottky emission and space-charge-limited current in HRS were dominant conduction mechanisms for URS and BRS, respectively. In the case of BRS, high oxygen vacancies may exist in the CF ruptured region and the Schottky barrier height should be low since the rupture of CF through the oxidation of metallic Sb is not fully completed. Therefore, injected electrons will be trapped by oxygen vacancies in the CF ruptured region. The URS phenomenon was explained by rupture and recovery of localized CF, however, the BRS phenomenon was controlled by the motion of oxygen vacancies and oxygen ions within filament rupture region between Sb top electrode and remained CF.

Finally, the effect of bottom electrode on resistive switching property of Sb_2O_5 thin film was studied using Ti and TiN as the bottom electrode. In the case of $\text{Sb}/\text{Sb}_2\text{O}_5/\text{Ti}$ sample, the various electroforming and resistive switching properties were obtained due to the effect of oxygen diffusion from Sb_2O_5 to Ti bottom electrode. URS and BRS endurance properties of SST were insufficient to satisfy the requirement for ReRAM application. In contrast, reproducible and stable switching endurance were obtained in $\text{Sb}/\text{Sb}_2\text{O}_5/\text{TiN}$ (SSN) structure. URS and BRS characteristics of SSN structure were similar with that of SSP structure. Because TiN film is widely

used material in electronic memory industry, SSN device can be one of promising candidate for use in ReRAM.

List of Publications

1. Journal (SCI)

1. Jaeyeong Heo, Seok-Jun Won, Dail Eom, Sang Young Lee, Young Bae Ahn, Cheol Seong Hwang, and Hyeong Joon Kim, "The Role of the Methyl and Hydroxyl Groups of Low-k Dielectric Films on the Nucleation of Ruthenium by ALD", ESL 11 (8) H210-213 (2008)

2. Seung Wook Ryu, Jong Ho Lee, Young Bae Ahn, Choon Hwan Kim, Bong Seob Yang, Gun Hwan Kim, Soo Gil Kim, Se-Ho Lee, Cheol Seong Hwang, and Hyeong Joon Kim, "The reason for the increased threshold switching voltage of SiO₂ doped Ge₂Sb₂Te₅ thin films for phase change random access memory", Appl. Phys. Lett. 95, 112110 (2009)

3. Seung Wook Ryu, Young Bae Ahn, Jong Ho Lee, and Hyeong Joon Kim "Thermal Stability of SiO₂ Doped Ge₂Sb₂Te₅ for Application in Phase Change Random Access Memory", Journal of Semiconductor Technology and Science, Vol.11, No.3, (2011)

4. Seung Wook Ryu, Ho-Ki Lyeo, Jong Ho Lee, Young Bae Ahn, Gun Hwan Kim, Choon Hwan Kim, Soo Gil Kim, Se-Ho Lee, Ka Young Kim, Jong Hyeop Kim, Won Kim, Cheol Seong Hwang and Hyeong Joon Kim, "SiO₂ doped Ge₂Sb₂Te₅ thin films with high thermal efficiency for applications in phase change random access memory",

Nanotechnology, 22, 254005 (2011)

5. Seung Wook Ryu, Young Bae Ahn, Hyeong Joon Kim, and Yoshio Nishi, "Ti-electrode effects of NiO based resistive switching memory with Ni insertion layer", Appl. Phys. Lett, 100, 133502 (2012)

6. Jong Ho Lee, Gun Hwan Kim, Young Bae Ahn, Ji Woon Park, Seung Wook Ryu, Cheol Seong Hwang, and Hyeong Joon Kim, "Threshold switching in Si-As-Te thin film for the selector device of crossbar resistive memory", Appl. Phys. Lett, 100, 123505 (2012)

7. Youngbae Ahn, Seung Wook Ryu, Jong Ho Lee, Ji Woon Park, Gun Hwan Kim, Young Seok Kim, Jaeyeong Heo, Cheol Seong Hwang, and Hyeong Joon Kim, "Unipolar resistive switching characteristics of pnictogen oxide films: Case study of Sb_2O_5 ", J. Appl. Phys. 112, 104105 (2012)

8. Youngbae Ahn, Jong Ho Lee, Gun Hwan Kim, Ji Woon Park, Jaeyeong Heo, Seung Wook Ryu, Young Seok Kim, Cheol Seong Hwang, and Hyeong Joon Kim, "Concurrent presence of unipolar and bipolar resistive switching phenomena in pnictogen oxide Sb_2O_5 films", J. Appl. Phys. 112, 114105 (2012)

2. Conferences

2.1 Domestic

1. Yeong Bae Ahn, Jeong Hyun Moon, Jae Bin Lee and Hyeong Joon Kim, “Preferred orientation texture of AlN thin films deposited by RF magnetron sputtering method”
2006 한국결정학회 춘계연구발표회, 서울대학교 반도체 공동연구소, 2006. 5. 26.
2. 안영배, 문정현, 이재빈, 김형준, “Deep RIE 공정을 이용한 차세대 이동 통신용 멤브레인 구조의 FBAR 제작”, 한국재료학회 춘계학술발표대회 및 제10회 신소재 심포지엄, 경상대학교 공과대학, 2006
3. Youngbae Ahn, Jong Ho Lee and Hyeong Joon Kim, “Fabrication and performance analysis of air gap type thin film bulk acoustic wave resonator”, 한국결정학회 추계학술발표회, 한국산업대학교, 2007. 11. 16,
4. 안영배, 문정현, 이종호, 정학준, 이재빈, 김형준, “이동통신용 FBAR 소자에 적용되는 high quality Mo/AlN 박막 증착 연구”, 제3회 강유전체 연합심포지엄, 무주리조트 티롤호텔, 2007. 2. 12.
5. Jong Ho Lee, Seung Wook Ryu, Yeong Bae Ahn, Se-Ho Lee, Cheol Seong Hwang, Hyeong Joon Kim, “Deposition and Chracterization of Bi doped $\text{Ge}_2\text{Sb}_2\text{Te}_5$ Thin Films for Phase Change Random Access Memory Appliaction”, 한국재료학회

추계학술발표대회, 2008. 11. 7, 차세대융합기술연구원, 2008

6. Seung Wook Ryu, Jong Ho Lee, Young Bae Ahn, Choon Hwan Kim, Cheol Seong Hwang and Hyeong Joon Kim, "Dependency of threshold switching on density of localized states of $\text{Ge}_2\text{Sb}_2\text{Te}_5$ thinfilms for phase change random access memory", 한국재료학회 추계학술발표대회, 2008. 11. 7, 차세대융합기술연구원, 2008

7. 이종호, 안영배, 박지운, and 김형준, "Phase change characteristics of Bi_2Te_3 -doped $\text{Ge}_2\text{Te}_2\text{Te}_5$ thin films for the application of phase change random access memory", 한국반도체디스플레이기술학회 2012년 춘계학술대회 및 제2회 반도체 디스플레이 제주포럼, 제주대학교 국제교류회관, 2012

8. 박지운, 안영배, 이종호, and 김형준, "Threshold switching phenomenon of SbTeO film", 한국반도체디스플레이기술학회 2012년 춘계학술대회 및 제2회 반도체 디스플레이 제주포럼, 제주대학교 국제교류회관, 2012

9. 안영배, 이종호, 박지운, and 김형준, "The characteristics of resistive memory using antimony oxide thin film", 한국반도체디스플레이기술학회 2012년 춘계학술대회 및 제2회 반도체 디스플레이 제주포럼, 제주대학교 국제교류회관, 2012

10. 박지운, 안영배, 이종호, 김형준, "안티모니텔레륨 산화막의 threshold switching 현상에 대한 연구", 한국반도체디스플레이기술학회 2012년 추계학술대회, 킨텍스

(KINTEX), 일산, October, 2012

11. 안영배, 이종호, 박지운, 김영석, 김형준, "저항 변화 메모리 적용을 위한 안티모니 산화막의 unipolar 및 bipolar 저항 변화 특성", 반도체디스플레이학회 추계학술대회, 킨텍스 (KINTEX), 일산, October, 2012

2.2 International

1. Young Bae Ahn, Jong Ho Lee, Jeong Hyun Moon, Hak Joon Jeong, Jae Bin Lee, and Hyeong Joon Kim, "Fabrication and Characterization of Air Gap Type Thin Film Bulk Acoustic Wave Resonator Using Deep Silicon Etching Process", 212th Meeting of The Electrochemical Society (ECS, Washington DC, MA USA), October 7-12, 2007

2. Young Bae Ahn, Jong Ho Lee, and Hyeong Joon Kim, "Fabrication and Performance Evaluation of Air-gap Type Film Bulk Acoustic Wave Resonator and Filters", ICMAP 2008, Jeju, Korea, August 18 – 20, 2008

3. S.W. Ryu, J.H. Lee, Y.B. Ahn, C.S. Hwang, H.J. Kim, "Phase Transformation Behaviors of SiO₂ Doped Ge₂Sb₂Te₅ Films for Application in Phase Change Random Access Memory", ICMAP 2008, Jeju, Korea, August 18 – 20, 2008

4. Y.B. Ahn, S.W. Ryu, J.H. Lee, , C.H. Kim, H.J. Kim, "Thermal and electrical

effects of TiAlN as heater to reduce reset current for application in Phase Change Memory”, 10th Annual non-volatile memory technology symposium, October 25-28, 2009

5. S.W. Ryu, J.H. Lee, Y.B. Ahn, C.H. Kim, C.S. Hwang, H.J. Kim, “The reason for the increased threshold switching voltage of SiO₂ doped Ge₂Sb₂Te₅ thin films for phase change random access memory”, 10th Annual non-volatile memory technology symposium, October 25-28, 2009

6. J.H. Lee, S.W. Ryu, Y.B. Ahn, C.H. Kim, H.J. Kim, “Deposition and characterization of Bi doped Ge₂Sb₂Te₅ thin films for phase change random memory (PcRAM) application”, 10th Annual non-volatile memory technology symposium, October 25-28, 2009

7. J. H. Lee, S. W. Ryu, Y. B. Ahn, and H. J. Kim, “Deposition and Characterization of Bi doped Ge₂Sb₂Te₅ Thin Films for Phase Change Random Access Memory Application”, The 7th AMF-AMEC, June 28- July 1, 2010

8. S. W. Ryu, H. K. Lyeo, J. H. Lee, Y. B. Ahn, G. H. Kim, C. H. Kim, S. G. Kim, S. H. Lee, K. Y. Kim, J. H. Kim, W. Kim, C. S. Hwang and H. J. Kim, “The improvement of thermal efficiency by SiO₂ doping into Ge₂Sb₂Te₅ for application in Phase Change Random Access Memory”, The 7th AMF-AMEC, June 28- July 1, 2010

9. Seung Wook Ryu, Young Bae Ahn, Jong Ho Lee, Choon Hwan Kim, Ka Young

Kim, Ju hee Lee, Won Kim, and Hyeong Joon Kim, "Thermal stability of SiO₂ doped Ge₂Sb₂Te₅ for application in phase change random access memory", ITC-CSCC, Gyeongju, Korea, 2011

10. Jong Ho Lee, Seoung Wook Ryu, Young Bae Ahn, Gun Hwan Kim, Choon Hwan Kim, Youshio Nishi and Hyeong Joon Kim, "Bi-doped Ge₂Sb₂Te₅ thin films by cosputtering Ge₂Sb₂Te₅ with Ge₂Bi₂Te₅ for phase change memory application", TC-CSCC, Gyeongju, Korea, 2011

11. Seung Wook Ryu, Jong Ho Lee, Young Bae Ahn, and Hyeong Joon Kim, "Formation mechanism of layered structure in SiO₂-doped Ge₂Sb₂Te₅ for phase-change random access memory application", ICEIC 2012, Jeongseon, Korea, 2012

12. Seung Wook Ryu, Liang Zhao, Jong Ho Lee, Young Bae Ahn, and Hyeong Joon Kim, "Bias polarity dependency on NiO-based unipolar resistive switching by insertion of nickel layer", ICEIC 2012, February 1-3 Jeongseon, Korea

13. Youngbae Ahn, Jong Ho Lee, Ji Woon Park, and Hyeong Joon Kim, "Resistive switching and endurance characteristics of Sb₂O₅ thin films in Pt/Sb₂O₅/Pt and Sb/Sb₂O₅/Pt structures" 12th Non-Volatile Memory Technology Symposium 2012 (NVMTS 2012), 31 Oct - 2 Nov, 2012

14. Ji Woon Park, Youngbae Ahn, Jong Ho Lee, and Hyeong Joon Kim, "Threshold switching phenomenon in SbTeO thin film" 12th Non-Volatile Memory Technology

Symposium 2012 (NVMTS 2012), 31 Oct - 2 Nov, 2012, Resorts World Sentosa,
Singapore

국문 초록

향후 전하를 이용한 기존의 메모리들이 집적화에 있어 한계를 맞이할 것으로 예상되면서, 이를 대체할 새로운 concept의 차세대메모리가 각광받고 있다. 저항변화메모리는 이러한 차세대 메모리 중 하나로서, 다양한 금속 산화물을 상부와 하부 전극 사이에 배치하는 간단한 캐패시터 구조를 가지고 있어 집적화에 유리하다는 장점을 가지고 있기 때문에 현재 활발한 연구가 진행되고 있다. 하지만 저항변화메모리의 상용화를 위해서는 보다 심도 깊은 연구가 필요하며, 구체적으로 set/reset 과정에서 발생하는 물리, 화학적 변화 메커니즘에 대한 이해와 신뢰성 확보가 이루어져야 한다. 저항변화메모리에 적용 가능한 다양한 금속 산화물 후보군 중에서, 현재까지의 연구는 TiO_2 , NiO 등의 저항변화 특성을 쉽게 관찰, 이해할 수 있는 물질이나 높은 결합에너지를 가지며 신뢰성이 높은 HfO_2 , Ta_2O_5 등의 물질에 대해 집중적으로 이루어졌다. 하지만 낮은 결합에너지를 갖는 금속 산화물 물질의 저항변화 특성 연구 또한 구동전력 감소 및 저항 변화 거동의 물리/화학적 메커니즘에 대한 이해라는 관점에서 중요한 연구 주제가 될 수 있다.

본 논문에서는 낮은 결합에너지를 갖는 금속 산화물 물질인 Sb_2O_5 박막을 reactive magnetron sputtering 방법을 이용하여 제조한 후, 그 저항 변화 특성을 평가하였다. Sb_2O_5 박막의 저항변화 거동은 저항변화 현상의 분류에 따라 unipolar 저항 변화 거동과 bipolar 저항 변화 거동에 대해 모두 평가되었으며, 금속 물질로는 백금과 안티모니를 이용하였다.

먼저 백금 상부 전극을 이용하여 Sb_2O_5 의 unipolar 저항변화 특성을 연구하였으며, 낮은 결합에너지로 인해 약 $200 \mu\text{A}$ 정도의 매우 작은 전류만으로 reset 이 되는 것을 확인하였다. 하지만 낮은 결합에너지로 인하여 반복되는 저항변화 과정 동안 쉽게 산소를 잃기 때문에 20회 미만의 cycle에서 set-stuck 현상이 발생하였다. 이를 개선시키기 위해 상부 전극 물질을 안티모니로 대체하여 연구를 진행하였으며, 그 결과 Sb_2O_5 박막의 저항변화 거동에 대한 신뢰성이 10배 이상 크게 향상되는 결과를 얻었다. 이는 상부 안티모니 전극이 oxygen blocking layer로서 작용함과 동시에 Sb_2O_5 박막 내부에 metal cluster들을 형성시켜 저항변화 스위칭시 소모되는 산소의 양을 현격히 줄여주기 때문으로 이해된다. TEM 분석 결과 set 상태의 Sb_2O_5 박막의 경우 metallic Sb가 박막 내부에 형성되어 있는 것을 관찰 할 수 있었으며, 따라서 결론적으로 Sb_2O_5 박막의 unipolar 저항변화 거동은 Sb_2O_5 박막 내부에서 국부적인 Sb filament의 형성과 파괴로 유발되는 것이라 할 수 있다.

다음으로 Sb_2O_5 박막의 bipolar 저항변화 거동에 대하여 filament 메커니즘과 연관 지어 그 특성을 고찰하였다. Sb_2O_5 박막의 bipolar 거동은 unipolar 저항변화 스위칭 과정 중에서 발생하는 비정상적인 reset 과정을 통해 관찰되었다. Unipolar와 bipolar 저항변화 거동 메커니즘 분석을 위하여 고저항 상태에서의 전도 메커니즘 분석결과 unipolar 저항변화 거동은 Schottky emission, bipolar 저항변화 거동은 space-charge-limited current로 각각 정의되었다. 이와 같은 결과를 통해 bipolar 저항변화 거동은 비정상적 unipolar reset 과정을 통해 필라멘트가 부분적으로 파괴되었을 때, 파괴된 부분에서의 산소 이온과 산소 공공의 이동에 따라 유발되는 것으로

이해된다.

마지막으로, 상부 전극 물질은 안티모니를 이용하고, 하부 전극 물질로 티타늄, 질화티타늄 등을 적용하여 Sb_2O_5 박막의 저항변화 특성을 비교하였다. 티타늄 박막을 하부전극으로 적용할 경우 산소 확산 효과로 인하여 Sb_2O_5 박막의 저항변화 특성이 열화됨을 확인할 수 있었다. 질화티타늄 박막을 쓴 소자의 경우 300회 이상의 안정된 저항변화 특성을 보였으며, 지우기 전류 값은 약 $200 \mu\text{A}$ 였다.

주요어 : Sb_2O_5 , 저항변화, 5족 산화물, 산화 안티몬, Unipolar 저항변화, Bipolar 저항변화, 필라멘트, 저항변화메모리

학 번 : 2008-30180

안 영 배